February 2008

Structural Analysis of a Simulated Supercooled Liquid

John A. Schneeloch
Worcester Polytechnic Institute

Project Number: GDP - 0701

Structural Analysis of a Simulated Supercooled Liquid

A Major Qualifying Project Report

submitted to the Faculty

of the

WORCESTER POLYTECHNIC INSTITUTE

in partial fulfillment of the requirements for the

Degree of Bachelor of Science

by

John Schneeloch

Date: March 3, 2008

Approved:

Professor George D. J. Phillies, Major Advisor

Professor Germano S. Iannacchione, Co-Advisor

1. molecular dynamics
2. liquids
3. glass transition

Abstract

We study the structure of a binary supercooled Lennard-Jones system with molecular dynamics simulations. To determine the structural characteristics of supercooled liquids, we compute spherical harmonic invariants of atomic configurations as introduced by Steinhardt, et al. [15] and extended by Phillies and Whitford [26]. We introduce a technique of plotting "two-harmonic distributions", which are distributions of configurations sorted according to two different invariants, and discuss their interpretation. We find that these distributions reveal "tails" that are indicative of icosahedral order.

Contents

1 Introduction

Some liquids remain liquid even when cooled significantly below their freezing points; these liquids are said to be supercooled. A supercooled liquid is in a metastable state, where all sufficiently small displacements of the point in phase space corresponding to the liquid result in a higher free energy, even though large displacements may result in a lower free energy [1]. When a supercooled liquid is cooled far enough, an amorphous solid may form, rather than a crystal; this is the glass transition. It is not entirely clear how or why glass formation happens. One theory was put forth by Frank [2] in 1952, who notes that for clusters of thirteen argon-like atoms, the magnitude of the binding energy is 8.4% greater when the twelve outer atoms were located at vertices of an icosahedron than of face centered cubic (FCC) or hexagonal close-packed (HCP) structures. Icosahedral order should thus prevail for small clusters. Since icosahedra cannot tessellate in flat three-dimensional space, frustration must occur to fill space with icosahedral ordering; this frustration reduces the advantage of icosahedral ordering over other structures. It has been found in molecular dynamics (MD) simulations that at least 5000 atoms are needed before the crystal structures' binding energies are greater than those for the icosahedral structures [3].

One of the most commonly used atomic potentials in molecular dynamics is the Lennard-Jones potential. For a binary system such as the one used in this project, this potential is given by

$$U_{ij} = \begin{cases} 4\epsilon \left[\left(\frac{\sigma_{ij}}{r}\right)^{12} - \left(\frac{\sigma_{ij}}{r}\right)^{6} \right] & , \quad r \leq 2.5 \\ 0 & , \quad r > 2.5 \end{cases} \tag{1}$$

Here, σ and ϵ are adjustable parameters. The indices i and j on σ_{ij} represent the species of each particle in the pair, either A or B for each particle. For a monatomic system, σ would not need any indices. ϵ represents the well-depth of the potential, and it has no indices because both species in this project have the same ϵ. In this project, we have

$$\begin{aligned} \sigma_{AA} &= 1 \\ \sigma_{AB} &= 11/12 \\ \sigma_{BB} &= 5/6 \end{aligned} \tag{2}$$

These parameters were taken from Phillies and Whitford [26]. r is the distance between the centers of the two particles. If we were to neglect the attractive portion of the potential, we would have a potential that approximates a hard-sphere potential due to the steepness of the r^{-12} curve [29]. The Lennard-Jones minimum is at $2^{1/6}\sigma_{ij}$, and this radius can be thought of as the radius of such a hard-sphere particle.

When one has two species of differently sized Lennard-Jones particles, the degree of icosahedral order depends on the size ratio of the species. Molecular dynamics simulations with two species may be used as a way to inhibit crystallization [4]. Alternate methods exist as well, such as quenching a system

quickly [15] or using a potential that inhibits crystallization. One example of a crystallization-inhibiting potential is the Dzugutov potential [5]:

$$
\begin{aligned}
V &= V_1 + V_2, \\
V_1 &= A(r^{-m} - B)\exp\frac{c}{r-a}, r < a, \\
V_1 &= 0, r \geq a, \\
V_2 &= B\exp\frac{d}{r-b}, r < b, \\
V_2 &= 0, r \geq b
\end{aligned}
\tag{3}
$$

Here, V is the total potential, equal to the sum of two different potentials V_1 and V_2; r is the distance between two particles' centers; m, A, B, a, b, c, and d are adjustable parameters. At short distances this approximates the Lennard-Jones potential, but, unlike for the LJ potential, for the Dzugutov potential we have a maximum outwards from the minimum. The location of this maximum can be adjusted to inhibit the formation of certain crystal structures.

Cozzini and Ronchetti investigated various size ratios and combinations in MD simulations of binary LJ systems [8]. The size ratio between a smaller species S and a larger species L was given by α according to

$$\sigma_{LL} = \alpha\sigma_{SS}$$

In addition, $\sigma_{LS} = (\sigma_{LL} + \sigma_{SS})/2$. Both species had particles of equal mass and equal well-depth ϵ (see (1)), so that the only parameter distinguishing between particle species was the size ratio α. (This is also the case with this project, where we have $\alpha = 1.2$.) Cozzini and Ronchetti investigated 13-atom clusters with α values of 1.6, 1.4, 1.33, and 1.25. A second parameter η represents the number of S atoms in the cluster. Cozzini and Ronchetti started their simulations with liquid clusters of all L atoms. They then replaced η of these L atoms with S atoms, then quenched the system to find a minimum potential energy state. In a separate simulation, multiple clusters were formed for a certain η by starting with a liquid cluster with η S atoms and $13 - \eta$ L atoms, taking "snapshots" every 10,000 time steps, and quenching each snapshot to its lowest energy state. The temperature of the liquid clusters was high enough so that the snapshots were statistically independent from each other. These two processes yielded equivalent lowest energy states.

The aim of Ronchetti and Cozzini was to examine the energies of the clusters for each local energy minimum and to examine the structure of these states. For the structural analysis, three tools were used: Voronoi polyhedra, common neighbors analysis, and Steinhardt's invariants [15]. Common neighbors analysis and the spherical invariants will be discussed below. The process of the Voronoi polyhedron is as follows: First, define the central atom as the atom in the cluster with the highest number of first neighbors. Next, determine the corresponding polyhedron where each face of the polyhedron is centered on each

atom neighboring the central atom. This polyhedron can be classified in the form (a, b, c, d, e) according to how many faces have 3, 4, 5, 6, and 7 faces respectively. For an icosahedral configuration, the corresponding polyhedron is the polyhedron whose faces are centered on the vertices of an icosahedron. A dodecahedron satisfies this condition, so the corresponding indices are (0,0,12,0,0) since a dodecahedron consists of twelve pentagons.

For $\alpha = 1.25$, Cozzini and Ronchetti [8] report that most polyhedra are 12-faced for all η. At $\alpha = 1.33$ and $\alpha = 1.4$, most polyhedra are 12-faced only for high η, with 10- and 11-faced polyhedra becoming more common for lower η. For $\alpha = 1.6$, 12-faced polyhedra are dominant only for very high η. Most icosahedral structures found by Cozzini and Ronchetti were either large particles surrounding a small particle, or a structure with a large particle at the center. These structures were referred to as S-ICO and L-ICO respectively.

Iwamatsu [6] [7] compiled a list of minimum energy states for clusters of thirteen particles of two species. He found that when the size ratio is less than about .6 - .7, most of the lowest energy states are not icosahedral. (Note that size ratios can be expressed as either α or $1/\alpha$. A size ratio less than .6 - .7 is equivalent to a size ratio α being greater than 1.43 - 1.67.)

There have been many theories attempting to link frustrated icosahedral structure to tessellation in curved space [9] [10]. In these theories, a frustrated system of particles is transformed into an unfrustrated system if space is curved. One may thus analyze something in the curved space and then transform to Euclidean space by adding disclination lines. This transform is difficult in practice, however [11].

Experiments by Fischer et al. involving abnormal light scattering may be explained by a frustration theory. [12] Fischer, et al. noticed anomalies in the scattering of light from supercooled orthoterphenyl; these anomalies include that light scattering grew for hours after the initial supercooling and that enhanced scattering found for low temperatures persisted for days after the sample was heated well above melting. Kivelson [13] developed a theory of frustration that claimed to explain these experimental findings. For the free energy Kivelson used the expression:

$$F = \sigma L^2 - \phi L^3 + s_o L^5 \tag{4}$$

Here F is the free energy, L represents the size of the cluster in one dimension, and σ, ϕ, and s_o are coefficients. The first term represents the surface energy of the cluster, the second term represents the free energy of the bulk volume, and the last term represents the strain energy required to transfer the structure from a curved space, in which the structure is unfrustrated, to Euclidean space, in which the structure become frustrated. This expression is similar to the free energy expression used in nucleation theory except for the last term.

To investigate frustration theories in MD simulations, one must have a way of determining the nature of the structure of the atoms in the system. Quantities such as the structure factor and the radial distribution function are commonly used in this regard [14] [27]. The common neighbors analysis (described below) and the Voronoi polyhedra method are two more methods to determine

structure, these taking into account the angular distribution of atoms. Another method presented by Steinhardt, et al. involves finding rotationally invariant combinations of the spherical harmonic components of the positions of atoms about a core atom [15]. The spherical harmonic components for a cluster of atoms are

$$Q_{lm} = N^{-1} \sum_{i=1}^{N} Y_{lm}(\hat{\mathbf{r}}_i) \tag{5}$$

Here, i is the index defining each atom within the cluster; l and m are integers labeling the spherical harmonics, where $m \geq 0$ and $-l \leq m \leq l$; $Y_{lm}(\hat{\mathbf{r}}_i)$ are the spherical harmonics for each atom position $\hat{\mathbf{r}}_i$; and N represents the number of points in the cluster. The first combination of spherical harmonic components Steinhardt, et al. used is

$$Q_l^2 = \frac{4\pi}{2l+1} \sum_{m=-l}^{l} |Q_{lm}|^2 \tag{6}$$

This expression is normalized so that $Q_0^2 = 1$ and that $0 \leq Q_l^2 \leq 1$. Q_l is simply $\sqrt{Q_l^2}$, but we shall refer solely to the Q_l^2, which we will often call the "harmonics".

The above describes the Q_l^2 as they are calculated in this project, but it is worth mentioning how Steinhardt, et al. [15], Tomida and Egami [11], and Phillies and Whitford [26] have used these invariants. Steinhardt, et al. defined a bond to be a line segment connecting two neighboring atoms. Neighbors were atoms within $1.2r_o$ units of each other, where r_o was the location of the Lennard-Jones minimum. (For a more general system, such as one with multiple species with different potential minima locations, Steinhardt, et al. suggested a nearest-neighbor definition with r_o being the location of the first peak of the radial distribution function.) The angles used to calculate spherical harmonic components were the angles of the bonds relative to the system's coordinate axes. This bond angle definition is arbitrary in that the direction of the bond (i.e., from which atom to which atom the bond points) is not specified, but this was unimportant to Steinhardt, et al. since they only calculated the Q_l^2 for even l, which are invariant with respect to bond direction. Steinhardt, et al. took the average Q_l^2 over all bonds within a sphere centered in the cube defining the boundary conditions, with a radius of seven times the first peak of the radial distribution function.

Tomida and Egami [11] did not calculate the Q_l^2, but they did find the Q_{ml} and used them in a "cluster orientational correlation function". These Q_{lm} differed from Steinhardt, et al.'s Q_{lm} in that these functions were averaged over each configuration rather than over all bonds within a certain distance from the system's center, where we use "configuration" to mean all atoms within a certain distance of a certain atom. Phillies and Whitford [26] follow this approach of averaging harmonic quantities over each configuration, and we follow Phillies's and Whitford's approach.

We define the "shell atoms" to be the atoms neighboring a chosen atom called the "core" atom. A spherical harmonic decomposition implies that we can liken shell atom positions to points on a sphere, so as an approximation, we divide the space around the core atom into shells. We say that all atoms within a certain distance of the core atom are in the "first coordination shell", that all atoms outside the first shell but within a second shell radius are in the "second coordination shell", and so on.

Besides the Q_l^2, there are other rotationally invariant combinations of spherical harmonics used in the literature. Steinhardt, et al. [15] introduced the third-order invariants:

$$W_l = \sum_{\substack{m_1,m_2,m_3 \\ m_1+m_2+m_3=0}} \begin{pmatrix} l & l & l \\ m_1 & m_2 & m_3 \end{pmatrix} \times Q_{lm_1} Q_{lm_2} Q_{lm_3} \tag{7}$$

The array in the W_l equation is a Wigner $3j$ symbol. The sum is taken over all m_1, m_2, and m_3 such that $m_1 + m_2 + m_3 = 0$. Terrones and Mackay [16] presented the fourth-order invariants:

$$Z_l = \sum_{\substack{m_1,m_2,m_5 \\ m_1+m_2+m_5=0}} \sum_{\substack{m_3,m_4,m_5 \\ m_3+m_4+m_5=0}} (-1)^{l-m} \begin{pmatrix} l & l & l \\ m_1 & m_2 & m_5 \end{pmatrix} \begin{pmatrix} l & l & l \\ m_3 & m_4 & m_5 \end{pmatrix}$$

$$\times [Q_{lm_1} Q_{lm_2} Q_{lm_3} Q_{lm_4}] / [Q_l^4] \tag{8}$$

The ensemble averages of these quantities, as well as their ratios, can be a sensitive measure of structure. These rotationally-invariant quantities are all indexed by l, but it is possible to create invariant quantities that are combinations of a number of different l. For example, Mitus et al. [33] used the following quantity to measure the degree of icosahedral structure:

$$Q_{l_1 l_2 l_3} = \sum_{m_1 m_2 m_3} \begin{pmatrix} l_1 & l_2 & l_3 \\ m_1 & m_2 & m_3 \end{pmatrix} \times Q_{l_1 m_1} Q_{l_2 m_2} Q_{l_3 m_3} \tag{9}$$

where $(l_1, l_2, l_3) = (4, 4, 6)$.

The importance of icosahedra (especially "perfect" icosahedra) in the structure of supercooled liquids has been questioned by many. Stillinger and LaViolette [17] [18] defined, for each structure of coordination number 12, a criterion that distinguished icosahedra from fcc and hcp structures. Specifically, when one calculates a radial distribution function for a structure, one finds that the function's first peak, which represents the closest distance particles are likely to be to each other, is about the same for fcc, hcp, and icosahedral structures (1.05, 1.05, and 1.10 respectively), but that the second peak is at a different location for fcc and hcp versus the icosahedron, due to fcc and hcp structures having square faces and corresponding diagonal lengths (1.4849 for fcc and hcp vs. 1.7864 for icosahedra). Using this criterion, Stillinger and LaViolette found that, out of 1465 particles in their MD simulations with coordination number 12, only one had as few as one "distance violation". They accepted that this one

case was a distorted icosahedron, but noted that if one were to view structures with more than one violation as distorted icosahedra, one should remember that, to an extent, the fcc and hcp structures are also distorted icosahedra. They came to the conclusion that deviations of the coordination number from 12 were much more important to the amorphous structure of glasses than the presence of icosahedra, and demonstrated that $g(r)$ between particles of different coordination numbers varied considerably.

Mossa and Tarjus [19] have conducted simulations in which Lennard-Jones clusters are subjected to a mean-field approximation for the frustration effects existing in bulk condensed phases. This method involves using a radial distribution function to represent the effects of the numerous particles outside of the configuration by multiplying the radial distribution function by the two-body potential to find the external field. They found that the locally preferred structure is an icosahedron.

Experimentally, Di Cicco and Trapananti [20] used X-ray absorption spectroscopy to find the bond-angle distribution in undercooled liquid copper. Reverse Monte Carlo analysis was used to obtain configurations, from which the $\hat{W}_6$ distribution was calculated. The $\hat{W}_l$ are coefficients introduced by Steinhardt, et al. [15], and are equal to the ratio $\sqrt{W_l^2/\left(Q_l^2\right)^3}$. Di Cicco and Trapananti found that $\hat{W}_6$ had a broad range and extended toward the icosahedral value of $\hat{W}_6 = -0.1698$ as $\hat{W}_6$ became more negative. They noted that the $\hat{W}_6$ distribution changed little for higher temperatures except to shift slightly toward higher $\hat{W}_6$. Icosahedral order increases as $\hat{W}_6$ decreases to -0.1698, as Di Cicco and Trapananti proved when they plotted the bond-angle distributions corresponding to selected $\hat{W}_6$ values and noted that the bond-angle distribution had peaks in places expected for icosahedra. The icosahedral characteristics of the bond-angle distributions corresponding to each $\hat{W}_6$ seemed to be present for $\hat{W}_6 < -0.09$, so Di Cicco and Trapananti took the integral of the $\hat{W}_6$ distribution for $\hat{W}_6 < -0.09$ to count the number of "nearly-icosahedral" configurations. They found that about 10% of the configurations could be defined as nearly-icosahedral.

Ganesh and Widom [21] have conducted MD simulations of copper via the "first principles" approach, in which quantum mechanics is used to determine forces and energies, though the particles themselves move classically. They have found "small but significant" disagreement with Di Cicco and Trapananti's experimental data [20]. They attribute this difference to a different method of determining positions. Di Cicco, et al. used a reverse Monte Carlo method, while Ganesh and Widom used a first-principles molecular dynamics method.

Celino, et al. [22] showed that "defective" icosahedra, as well as "perfect" icosahedra, lower the local cohesive energy. They used "common-neighbor analysis" [3] by attributing to each pair of nearest-neighbor atoms three numbers: the number of nearest neighbors common to both atoms, the number of bonds between these common neighbors, and the "number of bonds in the longest continuous chain formed" by the bonds connecting common neighbors. These three numbers can be represented as indices jkl. 421 and 422 indicate hcp and fcc;

555 implies icosahedral order; 544 and 433 results from a broken bond between common neighbors in a perfect icosahedron. Let N_{555} represent the number of atoms surrounding an atom having indices 555. If an atom is in the center of a perfect icosahedron, then $N_{555} = 12$. The fraction of particles having $N_{555} = 12$ (i.e., the number of perfect icosahedra) is 0.26% for undercooled systems, dropping to 0.11% for warmer liquid systems. For defective icosahedra, where $N_{555} \leq 6$, the fraction is 9.15%. Celino, et al. note that this calculation agrees with the 10% figure of Di Cicco and Trapananti [20].

There are a number of indirect experimental methods to determine the structure of glass. In addition to the X-ray absorption method used by Di Cicco and Trapananti [14] [20], Jansen, et al. [24] have done extensive investigation on experimental techniques of determining structure of amorphous compounds, using $Si_3B_3N_7$, a substance having properties ideal for such investigations, as an example. They divide their methods into three ranges: small (1-2 angstroms), medium (2-8 angstroms), and large (>8 angstroms). In addition, they use three categories of tools: "local probes" such as infrared spectroscopy, "interference methods" which determine pair correlation functions via scattering experiments, and "direct-imaging techniques" such as TEM, SEM, and AFM.

Mode-coupling theory (MCT) is one of the most successful theories of the glass transition [25]. In MCT, the glass transition is postulated to be the "singular behavior of the solution of the equations of motion of the dynamic structure factor." [4]. According to MCT, time correlations of quantities (such as the density) would for high temperatures decay as a single-exponential function, but for low temperatures the decay is more complicated [25]. In the short term, the nature of the decay will be the same for all temperatures; in intermediate times (the beta-relaxation regime) particles "appear trapped in cages formed by other particles"; for long times (the alpha-relaxation regime), the correlation decays according to a stretched exponential law. This theory is said to explain the behavior of some glass-forming materials, but not others. In addition, there is agreement that the singularity of the MCT equations is not the same as the real world glass transition.

There are several dynamical quantities which when calculated describe not only the structure of a system, but how this structure relates to the movement of the atoms. Sastry, et al. [23], for example, investigated the van Hove self-correlation function, which represents the distribution of distances particles travel in a certain unit of time. They found this function to be nearly Gaussian for high temperatures ($T = 1.06$), but gaining a second peak as temperatures decreased below $T = .61$, suggesting that to a certain extent, particles are trapped in atomic cages.

Donati, et al. [32] investigated the relationship between spatial correlation and mobility, where mobility is defined as the maximum distance a particle travels from its initial position over a certain convenient time period. This time period is the time when the distribution of particle displacements is broadest, and is many orders of magnitude greater than the microscopic "collision time". Donati, et al. determined that "mobile" particles were spatially correlated with other "mobile" particles, and "immobile" particles were spatially correlated with

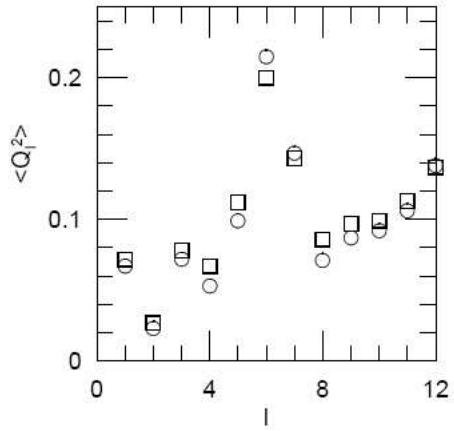

Figure 1: This is a plot of the $\langle Q_l^2 \rangle$ for particles within the first half shell as calculated by Phillies and Whitford [26]. The circles represent $T = 0.55$ and the squares represent $T = 0.88$.

other "immobile" particles. They found that most particles appear to be localized in cages, and a smaller number of mobile particles form "cooperatively rearranging 'strings.' " As the system evolves, mobile particles become immobile and immobile particles become mobile; on the α-relaxation time scale, all particles have the chance to be mobile.

The foundation of this project is the work of Phillies and Whitford [26]. They investigated a binary supercooled system of 15625 Lennard-Jones particles in a cubic system with density 1.30 and periodic boundary conditions. Phillies and Whitford calculated spherical harmonic invariants [26]; values for $T = 0.55$ and $T = 0.88$ are displayed in fig. 1. Historically, calculations of the odd-l invariants were avoided since expected structures (such as the icosahedral and crystal structures) would have odd-l harmonics equal to zero due to the inversion symmetry of these structures. Having decided to look at the odd-l harmonics, Phillies and Whitford found that the ensemble average of the $l = 7$ harmonic was greater than any other harmonic except for $l = 6$, surprising considering that septahedral order is rare in nature. In addition, they found that $\langle Q_{11}^2 \rangle$ had a magnitude on the order of $\langle Q_{10}^2 \rangle$ and $\langle Q_{12}^2 \rangle$, and that these all decrease by almost 10% as T decreases from 1.2 to 0.56. These facts suggest that the same

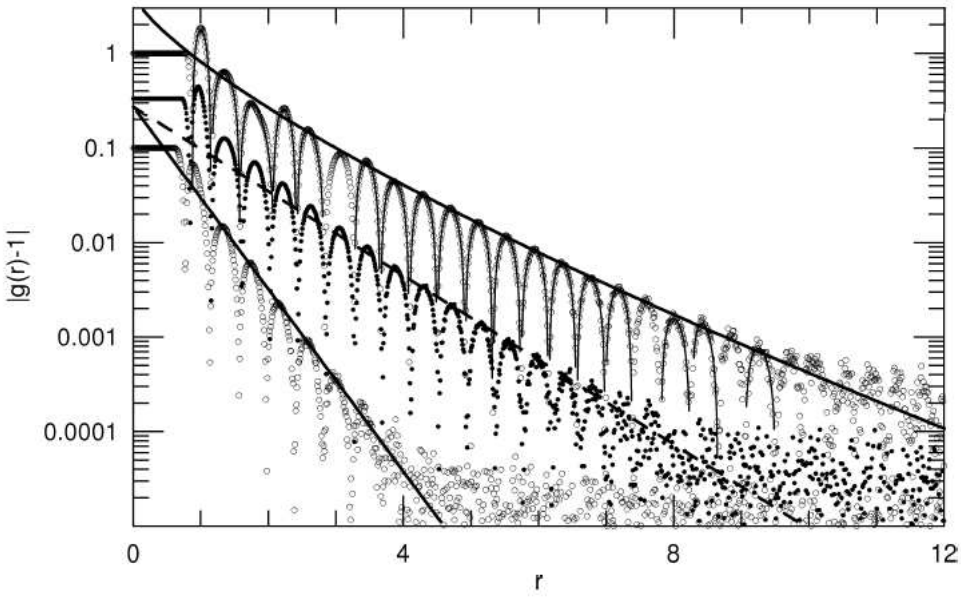

Figure 2: This is the all-atoms radial distribution function $g(r)$, plotted as $|g(r) - 1|$ against r, as calculated by Phillies and Whitford [27]. From top to bottom, these curves represent $T = 20$, $T = 2.01$, and $T = 0.56$. The latter two curves have been displaced downward for clarity, but $|g(0) - 1| = 1$ for all curves. Each peak on this plot represents either a peak or a trough on a $g(r)$ plot.

process is responsible for the magnitudes of all three harmonics. Phillies and Whitford noted that if icosahedral order were increasing, the 10th harmonic should increase, not decrease. As the system cools from 0.88 to 0.55, the 6th, 7th, and 12th harmonics increase, while all others decrease.

Phillies and Whitford have examined the distribution of the $\langle Q_l^2 \rangle$ over different times, limiting themselves to averages including all core atoms and all shell atoms regardless of type, as opposed to, for example, averaging over all type A core atoms and type B shell atoms, or any other species-specific averaging. The distributions of the averages $\langle Q_l^2 \rangle$ should not be confused with the distribution of the Q_l^2 over the atoms in the simulation. Conditional averages were also taken, where averages are restricted to a certain combination (jkl), where j represents the identity of the core atom (type A, type B, or all), k represents the number of type A shell atoms, and l represents the number of type B shell atoms.

Phillies and Whitford have performed wavelet decompositions on the system to obtain information about the position correlations of the harmonics. Most notably, when the temperature decreased, the correlation length of the $l = 7$ harmonic increased, but the correlation length of the $l = 5$ harmonic did not change much.

They have analyzed the time dependence of the spherical harmonic components via the correlation function

$$C_l^{(2)}(t) = \frac{4\pi}{2l+1} \sum_{m=-l}^{l} \langle Q_{lm}(0)\ Q_{lm}^*(t) \rangle \tag{10}$$

To save time, they only looked at $l = 5, 6, 7, 10, 11$, and 12. At $T = 1.20$, all of these correlation functions had a single shoulder. The $l = 6$ and $l = 7$ correlation functions were longest-lived, followed by the $l = 5$ function, then by the $l = 10$, $l = 11$, and $l = 12$ correlation functions. The similarity in the $l = 10$, $l = 11$, and $l = 12$ functions suggests a common origin, as noted above. At $T = 0.56$, slow modes were apparent, especially for $l = 10$, $l = 11$, and $l = 12$. Phillies and Whitford have quantified this description by fitting each curve to a stretched exponential form and finding mode lifetimes. Lifetimes depend substantially on l at $T = 1.2$, but at $T = 0.56$ lifetimes are independent of l.

2 Procedure

2.1 Parameters and Computer Specifications

This project consists of molecular dynamics simulations of two species of particles obeying a Lennard-Jones potential. This system was enclosed in an $L \times L \times L$ cube with $L = 45.93109$ and had periodic boundary conditions. The density was $N/V = 1.29$. The melting temperature of our system is believed to be $T = 1.1$ [27]. The Calvo and Sanz-Cerna fourth order method was used to simulate the particles' movements [31]. A time step consisted of one movement of the particles. The value of a time step depended on temperature. Time step values were

taken from Phillies and Whitford [28]. These values ranged from $\Delta t = 0.01$ for $.49 < T < 1.0$, to $\Delta t = 4.4 \cdot 10^{-5}$ for $T \approx 50000$. Here and throughout this project, T shall represent the temperature.

The simulation parameters and the program used to perform the simulations were taken from Phillies and Whitford [26] [28]. The simulations all had 125,000 particles, with 62,500 atoms of species A and 62,500 atoms of species B. As mentioned above for the simulations of Phillies and Whitford, the indices i and j refer to the species of each particle in the pair and may each be either "A" or "B". The Lennard-Jones potential is given in equation (1), but here the potential is species specific, acting on neighbors within 2.5 σ_{ij} of each other rather than within 2.5 distance units independent of species. The σ_{ij} and ϵ are the same as for Phillies and Whitford, the σ_{ij} being given by equation (2).

The units used in this project are the natural units used in many Lennard-Jones simulations, including simulations by Phillies and Whitford, and Steinhardt, et al. [15]. We have

$$T^* = k_B T/\epsilon$$
$$\rho^* = \rho\sigma^3/m$$
$$t^* = t(\sigma^2/m\epsilon)^{1/2}$$

For argon, these natural units can be converted to SI units such that one temperature unit is 120 K, one distance unit is 3.4 $\mathring{A}$, and one mass unit is 40 amu.

2.2 Calculations

The program we used performs a molecular dynamics simulation on a system of particles. This program was provided by Phillies and Whitford [28] and is available in the files that come with this project. The program used in this project was written in Fortran 77 and compiled using g77 in a Unix environment. Several of Worcester Polytechnic Institute's high-speed computers were used for the simulations, including vex.wpi.edu, big16.wpi.edu, and rave.wpi.edu. Vex.wpi.edu is a dual 2.6 GHz Opteron with 4 GB RAM, big16.wpi.edu is a 16-core Opteron with 32 GB RAM, and rave.wpi.edu is a Quad AMD Opteron with 2.8 MHz CPUs, and 4 GB RAM. In general, the time to compute one time step was about a few seconds, with some variation probably due to numerous programs running at the same time competing for the same resources. The difference in calculation times between the three computers was relatively small, usually masked by the variations in calculation time for each computer. To Phillies and Whitford's program several changes have been made, including cosmetic changes, correction of minor errors, and code introduced to calculate certain quantities listed below. In addition, MATLAB was often used to process data generated by Phillies and Whitford's program.

We define a "run" to be one execution of the program. Each run was either an "equilibration run", an "integration run", or a "cooling run", depending on its aim, though runs frequently had more than one aim (i.e., a combined equilibration and integration run.) Equilibration runs are runs in which the system

is moved forwards in time by solving Newton's laws of motion over numerous time steps without performing more time-consuming calculations. Integration runs are runs where, in addition to equilibration, other calculations may be performed, such as calculating the radial distribution function. Cooling runs are runs in which the system is cooled to a desired temperature through successive reductions by a certain percent until the actual temperature is within a certain percent of the desired temperature. See "list of runs.txt", a file that comes with this project, for a table of non-preliminary runs performed. One should be careful not to confuse an "integration run", where significant measurements and calculations are made, with an "integration", which refers to one integration of the equations of the Calvo and Sanz-Cerna method.

In this project temperature is defined as

$$T = \frac{\sum_i p_i^2}{3(n_1 + n_2 - 1)} \tag{11}$$

Here, i is the particle index, p_i^2 is the square of the magnitude of the momentum of the ith particle, n_1 is the number of particles of species A, and n_2 is the number of particles of species B. Because the mass of every particle is equal to 1, p_i is equal to the velocity v_i. We see that T is defined to be proportionate to the kinetic energy $\frac{\sum_i p_i^2}{2}$.

Temperatures mentioned in this paper with fewer than three significant figures should be considered approximate. There are a few reasons for the approximation. First, temperatures rapidly fluctuate within a range of about half a percent. The temperature the program outputs is the temperature at the last time step the temperature was calculated. Second, the cooling process is not exact, and the final temperature distribution will often be within the range of the goal temperature, but the average temperature at that time will be within about half a percent larger than the goal temperature. Third, for a series of runs stretching across a few hundred thousand time steps, the temperature drifts significantly due to the approximate nature of all integration methods and due to the tendency for the kinetic energy to drift while a system is equilibrating. Fourth, for obvious reasons it is more convenient to refer to a "$T = .54$" run than a "$T = .5435$" run, where the temperature with fewer significant digits would be the goal temperature and the other figure would be either the temperature at a certain time step or even the average temperature.

Phillies and Whitford have provided numerous equilibrated samples at temperatures ranging from $T = .59$ to $T = 50,000$ [28]. In addition, the author has created samples from $T = .51$ to $T = .56$ by equilibrating and cooling a $T \approx .557$ run provided by Phillies and Whitford. These runs can be split into six "series" of runs separated from each other by 0.01 temperature units. The total number of time steps for series 1-6 are, to the nearest 10,000 time steps: 300,000 for series 1 at $T \approx .56$, 320,000 for series 2 at $T \approx .55$, 390,000 for series 3 at $T \approx .54$, 280,000 for series 4 at $T \approx .53$, 248,000 for series 5 at $T \approx .52$, 149,000 for series 6 at $T \approx .51$.

One way to determine the degree of equilibration of a sample is to look at

the drift of its temperature, which is proportional to the average kinetic energy. When a system is in thermal equilibrium, the average kinetic and potential energies should fluctuate about constant values. (The total energy would always be constant, however.) If the system is not in equilibrium, then the kinetic energy should drift until the system reaches equilibrium. Thus, we take temperature data every time step so that we can look at the amount of drifting and make judgments on how equilibrated our samples are. These data are plotted in the "Validity tests of simulation" subsection in the next section.

In addition, we find the radial distribution function $g(r)$ and the correlation function $\langle Y_1 p_z \rangle$ and use these functions as tests of the validity of our simulation. Specifically, we can compare our $g(r)$ with the Phillies and Whitford $g(r)$ plotted in fig. 2. $\langle Y_1(0)p_z(t)\rangle$, abbreviated $\langle Y_1 p_z\rangle$, is given by

$$\langle Y_1(0)p_z(t)\rangle = \sum_i Y_1(0)p_z(t) \tag{12}$$

Here, Y_1 represents the spherical harmonic component of a configuration with $l = 1$ whos function is positive for $z > 0$ and negative for $z < 0$. p_z is the z-component of the momentum of a particle. The sum is taken over a certain number of randomly selected particles, over different moments in time spread far enough apart to be statistically independent. Y_1 signifies the distribution of the density of the configuration in the z-direction. If $Y_1 > 0$ for a configuration, then particles are congregated in the positive z-direction, and vice versa for $Y_1 < 0$. We would expect density fluctuations to even out over time, so if, for example, particles in a configuration tend to congregate in the positive z-direction, then the core particle should soon be heading in the negative z-direction, towards the lower density. Soon after $t = 0$, we would expect $Y_1(0)$ and $p_z(t)$ to be of opposite sign, so $\langle Y_1(0)p_z(t)\rangle$ should drop from 0 soon after $t = 0$. As time increases, the core particle's velocity and the original configuration become statistically independent, so we would expect $\langle Y_1(0)p_z(t)\rangle$ to rise back to zero.

To determine the structure of our simulated supercooled liquid, we, following Phillies and Whitford [26], calculate the $\langle Q_l^2\rangle$, defined in (6), for various temperatures. We call the l in Q_l^2 the "harmonic index". The Q_l^2 values will be referred to as the "harmonics", a term that should not be confused with the values Q_{lm} of the spherical harmonics. The Q_{lm}, unlike the Q_l^2, are not rotationally invariant. To calculate the Q_l^2, we must first decide on a definition for the coordination shells. Phillies and Whitford defined the shells to be the particles existing in the crests and troughs in between subsequent roots of $g(r) - 1$, where $g(r)$ is the radial distribution function that does not distinguish between species [28]. The shell radii defined in this way are the "half shell radii". Alternatively, we could define each shell to be the space between subsequent minima of $g(r)$. The radii under this definition will be referred to as the "full shell radii". Roughly speaking, the full shell radii represent full coordination shells and the half shell radii represent half shells. Most of the investigation in this project concerns only the first full shell.

To gain information beyond the $\langle Q_l^2\rangle$, we calculate the Q_l^2 distributions. Calculation of these single-harmonic distributions is straightforward. For each

l, the Q_l^2 lie within a certain range which we divide into equally-spaced bins, each bin containing the number of configurations within that segment of Q_l^2. However, while these distributions served as a stepping stone to developing the two-harmonic distributions mentioned below, there seems to be nothing about these distributions that the two-harmonic plots do not show more clearly, so we will not be introducing them in this paper except once to show the advantage of two-harmonic distributions.

To illuminate some of the odder aspects of the single-harmonic distributions, it is helpful to categorize configurations by two harmonics in what we call "two-harmonic distributions". These distributions are labeled by two harmonic indices (l, j). The calculation of these distributions is similar to the single-harmonic distribution calculation. For each of two harmonic indices l_1 and l_2, the configurations' harmonics lie within certain ranges which are divided into equally-spaced bins. If each axis has n bins, then the two-harmonic distribution has $n \times n$ bins because each configuration is categorized by $Q_{l_1}^2$ and $Q_{l_2}^2$. Each bin contains a certain number of particles, and in this project this particle number is represented in a pseudocolor plot on a scale from blue for few configurations to red for many configurations. The two-harmonic distributions (as well as for the harmonic averages and single-harmonic distributions) depend on shell radius definition, temperature, core atom species, coordination number, and the specific combination of species in the first shell. Representative examples for each dependence will be demonstrated in the next section.

One of the simplest ways to quantify the shape of the two-harmonic distributions is through cross-harmonic correlation functions:

$$c(j,l) = \frac{\langle Q_l^2 Q_j^2 \rangle - \langle Q_l^2 \rangle \langle Q_j^2 \rangle}{\langle Q_l^2 \rangle \langle Q_j^2 \rangle} \tag{13}$$

Here, j and l are two harmonic indices, with Q_l^2 and Q_j^2 being the corresponding harmonics. This function is normalized to account for the magnitude of the $\langle Q_l^2 \rangle$ and $\langle Q_j^2 \rangle$. Note that $c(j,l) = c(l,j)$. In general, the more elongated along a line of negative slope the two-harmonic distributions are, the more negative the cross-harmonic correlation. Eq. (13) is equivalent to

Unless otherwise stated, these calculations were performed every 200 time steps, usually over 4000 time steps total for a total of 20 different moments in time.

3 Results

3.1 Validity tests of simulation

For the six series we equilibrated, we present in figures 3 through 4 the temperature plots of six equilibration series, with the temperature data being subject to a 100-term moving average. The gaps in these plots represent missing temperature data during that period of equilibration. The missing patches of data are due to a number of reasons, including the hard drive crashing mid-simulation,

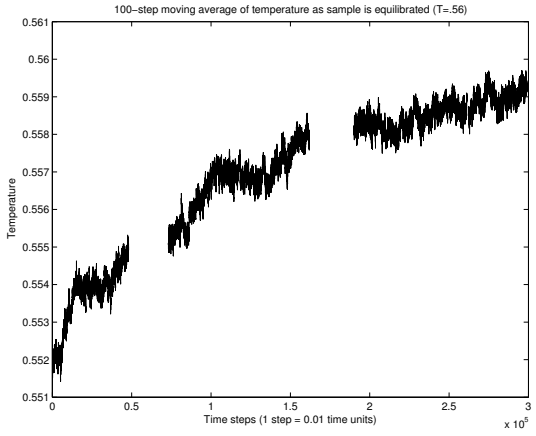

Figure 3: The temperature data for series 1. We note that as equilibration time increases, the temperature seems to drift upwards, and the rate of increase tends to decrease.

accidentally writing to a full hard drive, or being unable to retrieve data from compact disks due to errors.

All six series show an upward temperature drift at most times, suggesting that these series are only partially equilibrated. Series 1-3 have a rate of temperature increase that decreases, suggesting that these series are becoming more equilibrated with time. The temperature rate increase for series 4-6 cannot be judged as accurately, with rate increases that either appear to remain constant or that fluctuate too much to discern a pattern. We note that equilibration time is expected to be longer for lower temperatures, and that the numbers of time steps for series 1-3 are greater than for series 4-6.

To test the validity of our molecular dynamics simulations, we have generated the radial distribution function $g(r)$ and the correlation function $\langle Y_1 p_z(t) \rangle$ that was introduced in equation (12). We see that our $g(r)$ matches the radial distribution function of Phillies and Whitford [27] (see fig. 2). Both functions have amplitudes which decrease nearly exponentially with increasing distance; both functions share an oddly-shaped third crest, where the peak is skewed to lesser r; and both functions become nearly indecipherable for $r > 10$. These similarities are to be expected since both simulations are performed with the same system (i.e., same particle species and same parameters) and at similar temperatures ($T = .52$ for our plot vs. $T = .56$ for Phillies and Whitford.)

The $\langle Y_1 p_z(t) \rangle$ function also behaves as expected. As mentioned earlier, this function was expected to decrease suddenly, then increase to zero and remain there, which it does. The one surprise is a hiccup that appears as $\langle Y_1 p_z(t) \rangle$ increases in time.

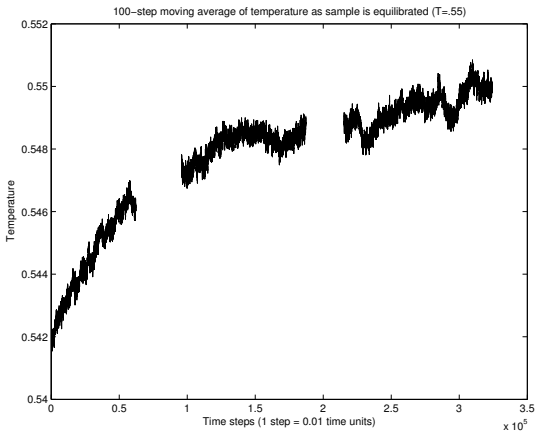

Figure 4: The temperature data for series 2. We note that as equilibration time increases, the temperature seems to drift upwards, and the rate of increase tends to decrease.

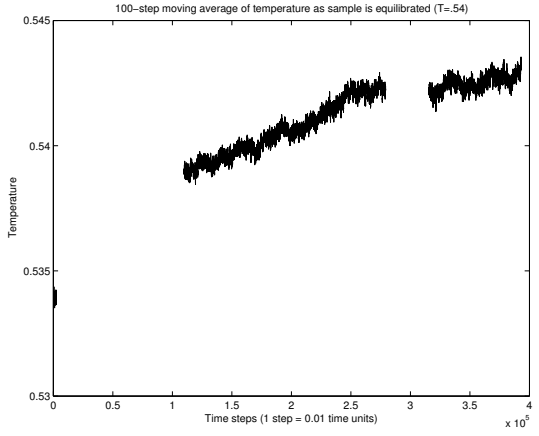

Figure 5: The temperature data for series 3. Due to a large section of missing data near the beginning, it is difficult to clearly see the change in the rate of temperature drift, but the existing data indicates an increasing temperature with a decreasing rate of temperature increase as equilibration time increases.

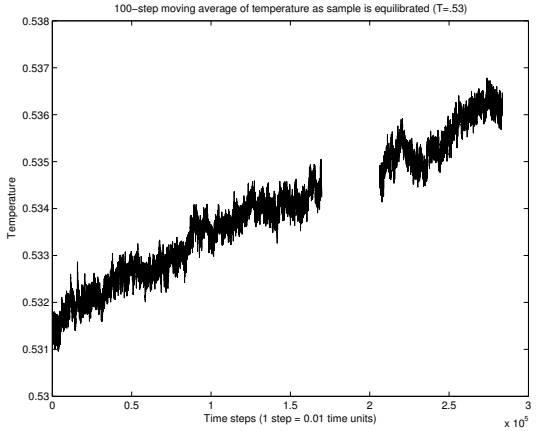

Figure 6: The temperature data for series 4. As equilibration time increases, temperature increases, and the rate of temperature increase seems to remain constant.

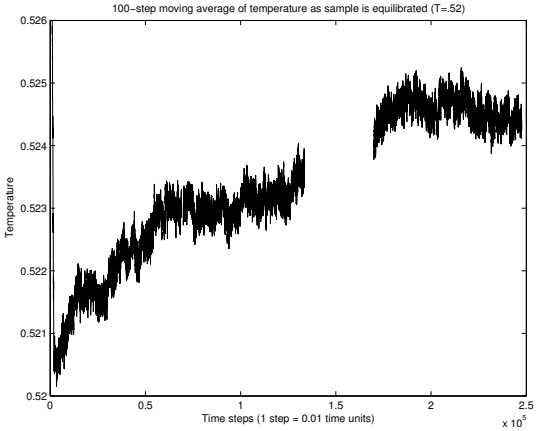

Figure 7: The temperature data for series 5. We note that as equilibration time increases, the temperature drifts upwards, and the rate of increase tends to vary between a steep increase and no increase.

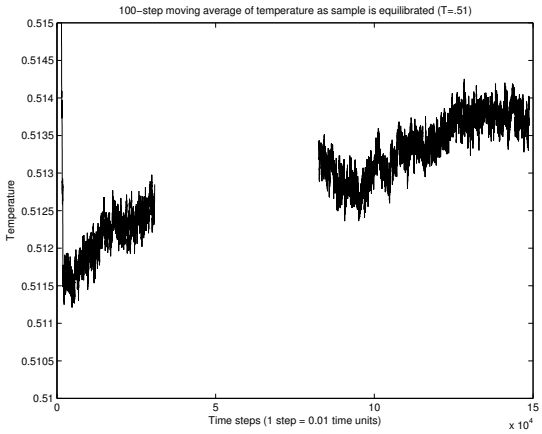

Figure 8: The temperature data for series 6. We note that as equilibration time increases, the temperature drifts upward.

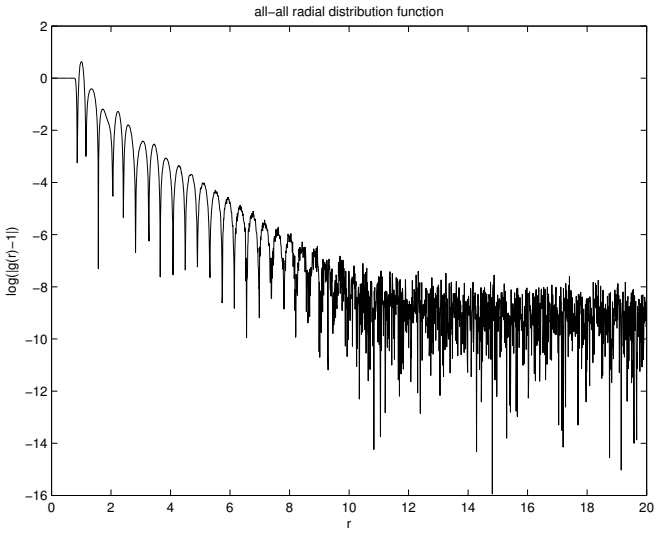

Figure 9: This is the radial distribution function between all particles regardless of species. $T = .52$. The species-dependent $g(r)$ have a similar shape, shifted towards greater r for A-A pairs, towards lesser r for B-B pairs, and with little shifting for A-B pairs. Compare with fig. 2.

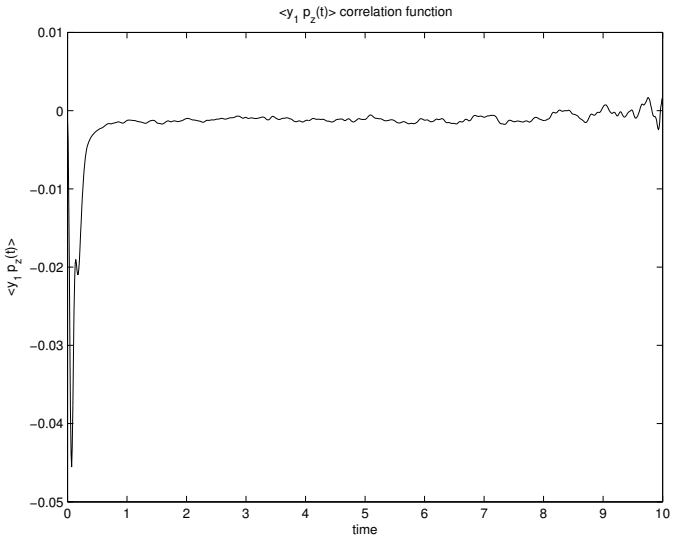

Figure 10: The correlation function $\langle Y_1(0)p_z(t)\rangle$ for $T = .52$. This function dips sharply soon after $t = 0$ due to the core particle responding to the density gradient within the first-shell configuration. After the function's initial dip, the velocity of the core particle is independent of the original configuration and $\langle Y_1 p_z\rangle$ goes to zero, although there is an unexplained hiccup along the way. As time increases, the fluctuations increase.

3.2 Harmonic averages

The harmonic averages $\langle Q_l^2 \rangle$ for the first half shell and the first full shell are calculated for a number of different temperatures. See fig. 11 and fig. 12 for a plot of the temperature dependence of the $\langle Q_l^2 \rangle$ for the first half shell and the first full shell respectively. The lowest temperature where $\langle Q_l^2 \rangle$ is plotted is $T = .52$; $\langle Q_6^2 \rangle$ is highest at this temperature. The harmonics for $T = .52$ in fig. 11 should agree with the $T = .55$ $\langle Q_l^2 \rangle$ plot in fig. 2, but while the even harmonics seem to match, the odd harmonics in fig. 2 are raised relative to the $T = .52$ harmonics in 11. In both fig. 12 and fig. 11 we note that as the temperature increases, the harmonic averages curve becomes flatter, and the location of the maximum of this function shifts to greater l. To get a better idea of the temperature dependence of $\langle Q_l^2 \rangle$, we plot Q_1^2 vs. temperature in fig. 13. We do this because from fig. 12 it seems plausible that temperature would decrease in a way that appears linear on a log-log plot, but fig. 13 shows that the slope of this curve decreases as temperature increases.

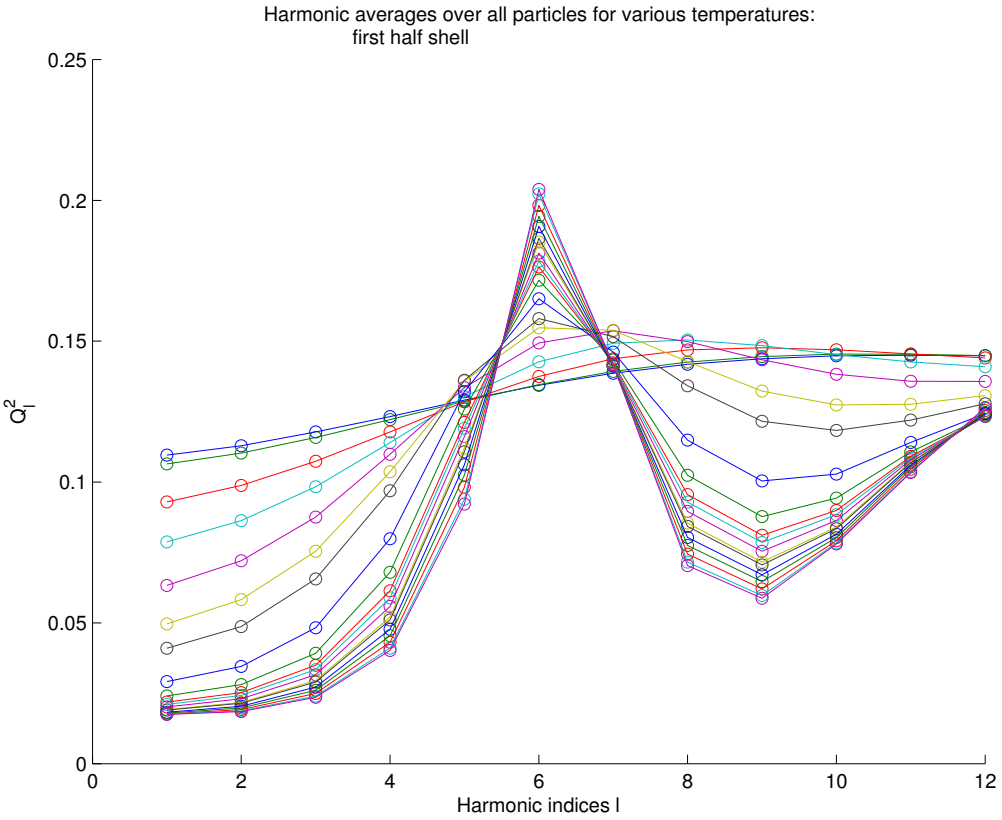

Figure 11: These are the first half shell's harmonics plotted for many different temperatures. As the temperature lowers, the first harmonic decreases. The specific temperatures plotted are: T=50000, 30000, 5000, 1000, 200, 50, 20, 5, 2.25, 1.6, 1.4, 1.2, 1.0, .9, .81, .73, .66, .62, and .59.

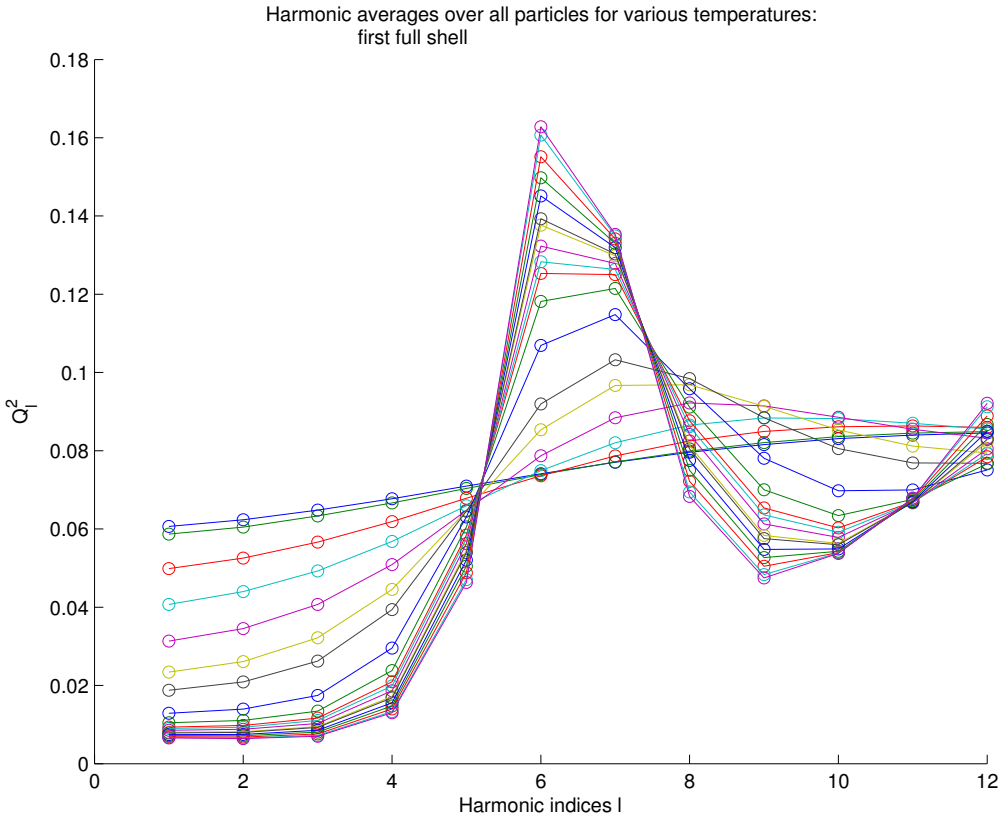

Figure 12: These are the first full shell's harmonics plotted for many different temperatures. As the temperature lowers, the first harmonic decreases. The specific temperatures plotted are: T=50000, 30000, 5000, 1000, 200, 50, 20, 5, 2.25, 1.6, 1.4, 1.2, 1.0, .9, .81, .73, .66, .62, and .59.

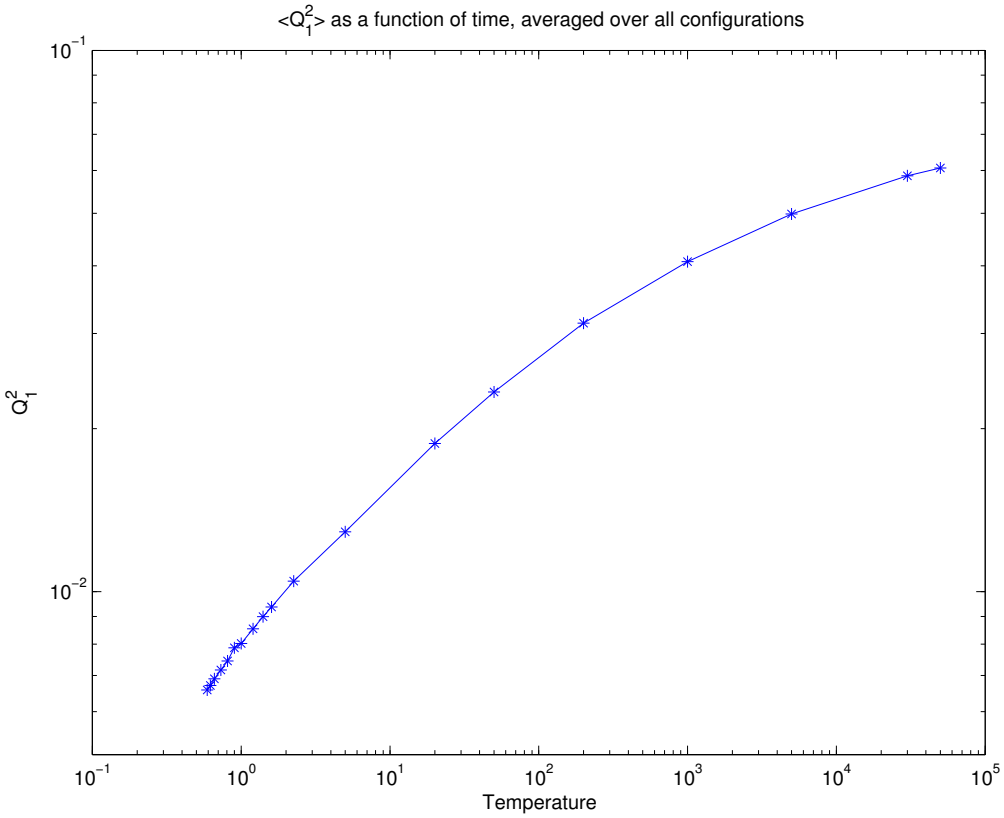

Figure 13: Here we plot $\langle Q_1^2 \rangle$ as a function of temperature, where the average is taken over all configurations. The shell radius used is the full shell radius.

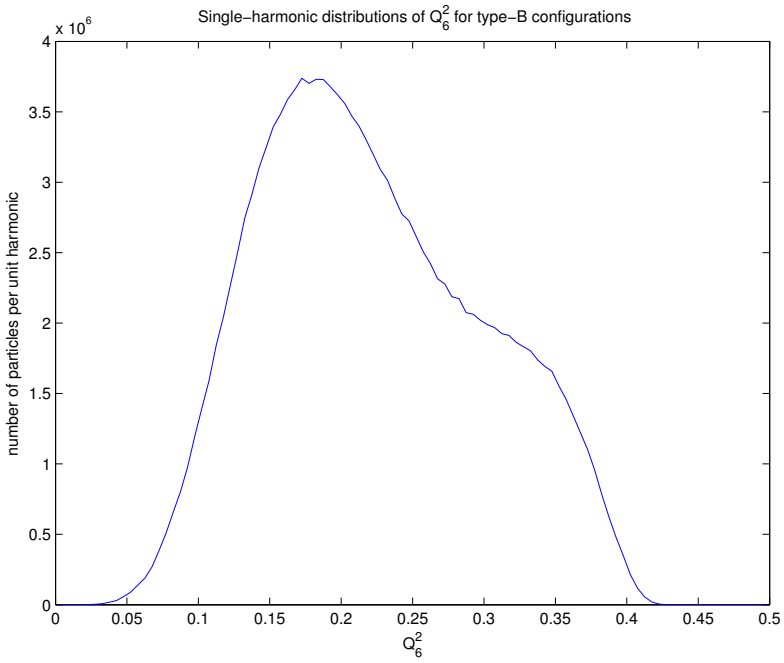

Figure 14: This is the distribution of Q_6^2 for type-B configurations.

3.3 Single-harmonic distributions

We do not devote much time to analysis of single-harmonic distributions because information gained by these distributions seems to be more obvious in the two-harmonic plots. For example, in fig. 14 we plot the distribution of the Q_6^2 for type-B configurations. If we plotted other single-harmonic distributions, especially the high-temperature distributions, we would notice that this curve has a greater-Q_6^2 bump that is not normally present. However, from the $(6, l)$ two-harmonic distributions for various l plotted below, we see tails for high-Q_6^2. Seeing tails in the two-harmonic plots is much more informative than seeing a bump in this single-harmonic distribution.

3.4 Two-harmonic distributions: Introduction

The two-harmonic distributions for various conditions are plotted in this section as pseudocolor plots. In each plot, configurations are categorized according to two different harmonics, represented by the horizontal and vertical axes. The density of the number of configurations at a certain pair of harmonic coordinates is mapped to color which ranges from dark blue for low density to dark red for high density. These distributions were generated by calculating the harmonics of the configurations for every particle over twenty different times (separated

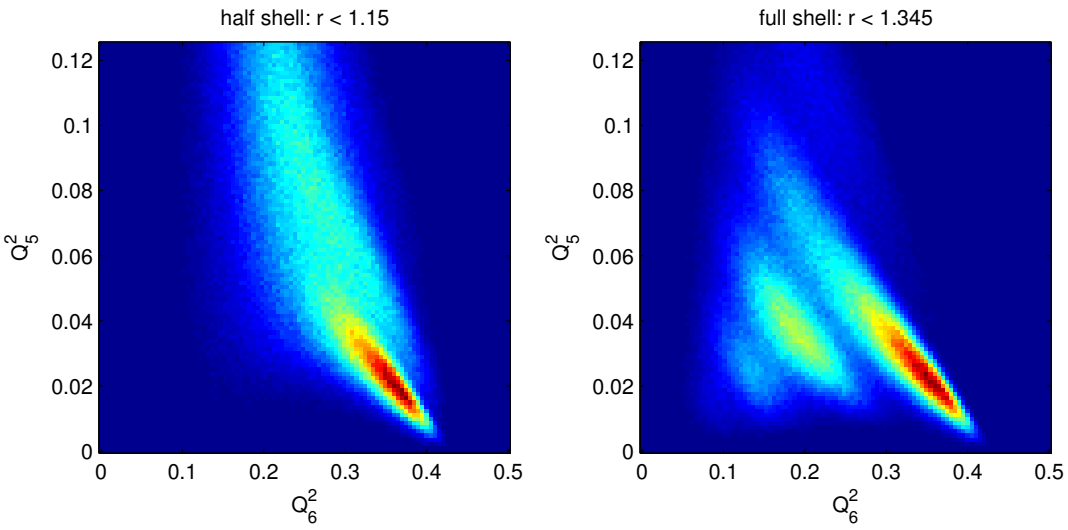

Figure 15: Two-harmonic distributions for $(6, 7)$ for type-B configurations. See text for plotting information. We see that the $r < 1.15$ shell definition results in a distribution that lacks the band structure of the distribution with $r < 1.345$.

by 200 time steps) for a total of 2,500,000 configurations' harmonics when all configurations were considered.

Fig. 15 compares the $(5, 6)$ distribution for type-B core atom configurations for the first half shell and first full shell. From these plots, it appears that the full-shell definition yields "sharper" distributions than the half-shell definition. Both plots clearly show a tail as $Q_5^2 \to 0$ and Q_6^2 increases, but the half-shell plot lacks the band structure of the full-shell plot. Also, there are few configurations below the main "tail" band. Below we note that the lower-Q_5^2 bands correspond to coordination numbers greater than 12. It seems consistent that a smaller shell size would result in fewer high-coordination-number configurations. Using the half shell radius would not necessarily be better or worse than using the full shell radius, but based on the seeming difference in "sharpness" of these graphs we decided to employ the full shell radius almost exclusively in this project.

Before we investigate the low-temperature distributions in more detail, we present a few two-harmonic distributions for $T \approx 50000$, plotted in figures 16 and 17. We notice that the $(8, 9)$, $(8, 10)$, $(9, 10)$, and $(9, 11)$ distributions all resemble each other. They appear to be roughly symmetrical about the diagonal line $Q_j^2 = Q_l^2$. They are simple in that they have one peak and do not have any protrusions. Finally, these distributions are round, that is, they have no tails or flat sides. When the word "ordinary" is used later to describe two-harmonic distributions, it will mean that the described distributions are similar to the $T \approx 50000$ distributions in that they have round, single-peaked distributions which are free of protuberances.

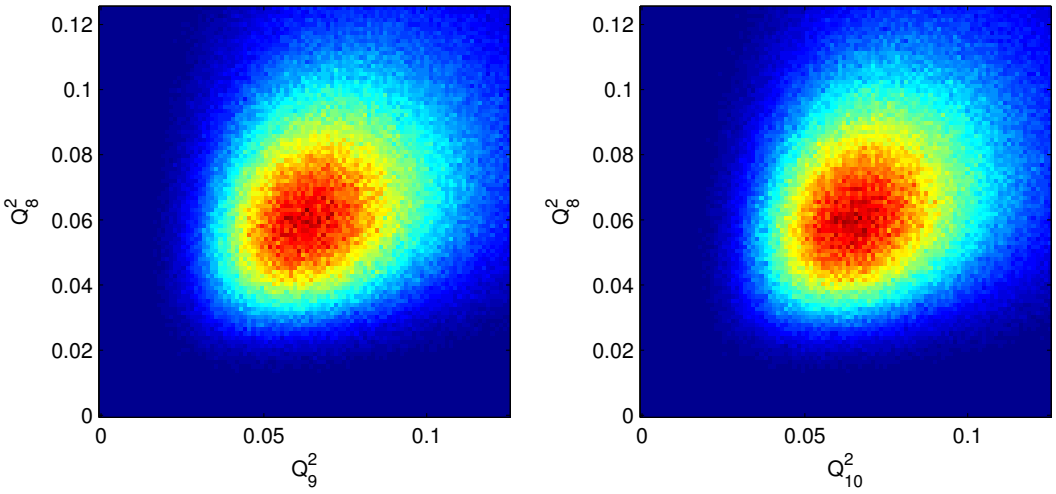

Figure 16: Two-harmonic pseudocolor plot for $(8, 9)$ and $(8, 10)$ for all configurations at $T \approx 50000$. See text for plotting information. These are typical examples of two-harmonic plots at high temperatures.

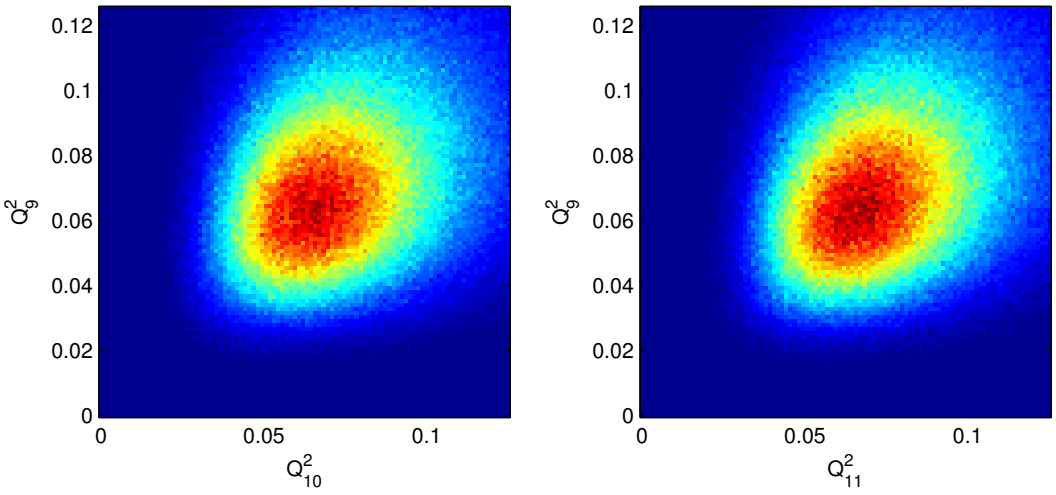

Figure 17: Two-harmonic pseudocolor plot for $(9, 10)$ and $(9, 11)$ for all configurations at $T \approx 50000$. See text for plotting information. These are typical examples of two-harmonic plots at high temperatures.

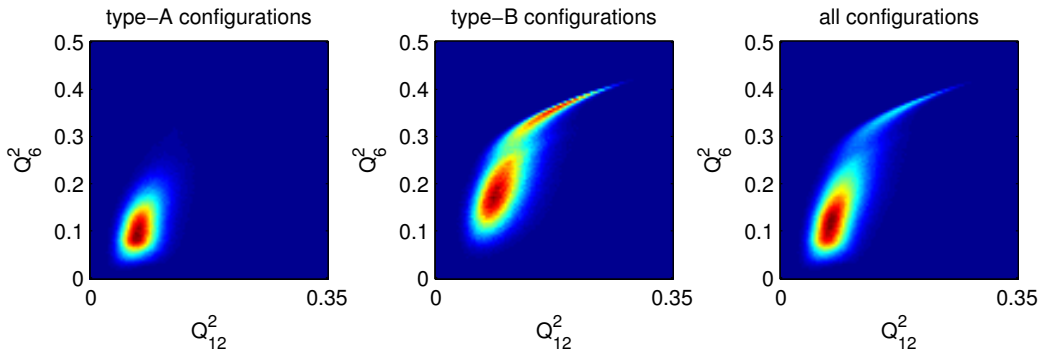

Figure 18: Two-harmonic pseudocolor plots for $(6, 12)$ at $T = .52$ for either just type-A configurations, just type-B configurations, or all configurations. See text for plotting information.

3.5 Two-harmonic distributions: Type-B configurations

The two-harmonic distributions at $T = .52$ are more complex than the $T = 50000$ distributions in figures 16 and 17. To better understand these distributions, we divide them into categories. The first categorization we will consider is by core atom species, so that some plots will represent just the configurations with type-A core atoms, and others just the configurations with type-B core atoms. We will refer to these configurations as "type-A configurations" and "type-B configurations". Next, we divide each core-species category into groups based on the coordination number, which is the number of atoms in the first full coordination shell. Finally, for a certain coordination number, we will vary the specific combination of type-A and type-B shell atoms.

The type-B and type-A configurations differ in that many of the two-harmonic plots for type-B configurations contain prominent "tails" which will prove to be indicative of formation of icosahedral structures. Because the presence of tails is important to this project, we will plot every two-harmonic plot for type-B configurations, but we will only plot a few notable plots for type-A configurations. To illustrate the difference between these distributions, we plot the two-harmonic distribution $(6, 12)$ at $T = .52$ in fig. 18 for just type-A configurations, just type-B configurations, and then all configurations.

The type-B two-harmonic distributions are plotted in figures 19 through 51. We note that many of these distributions have tails or protuberances where $Q_l^2 \to 0$ if $l \neq 6, 10$, or 12, and where Q_l^2 increases if $l = 6, 10$, or 12. The clearest example of a tail is probably the tail in the $(6, 12)$ distribution, where the tail configurations lie in the region $Q_6^2 > 0.3$ and $Q_{12}^2 > 0.1$. The length of this tail is greater than the major axis diameter of the nearly-elliptical lower portion of the distribution. The density of the tail is great enough for the distribution to be bimodal. There is no clean split between the tail and the "body" of the distribution, however, even when we categorize by coordination number or shell

species combination as we do later in this paper, but we can approximate the division between tail and body by defining the tail to be $Q_6^2 > 0.3$ and $Q_{12}^2 > 0.1$. In the remaining distributions, tails and protuberances come in various degrees of obviousness. The existence of a tail in $(6, 12)$ or $(5, 11)$ can be said to be very obvious because these tails extend out a distance that is a significant fraction of the size of the non-tail parts of the distributions, and because these tails are so thin compared to the distributions' bodies. Slightly less obvious are tails such as the extension in $(5, 10)$, which are not nearly as thin as the $(6, 12)$ and $(5, 11)$ tails. Even less obvious is the existence of a tail in $(5, 8)$. There is clearly an extension towards the origin in $(5, 8)$, but it is unclear where a tail begins and a body ends. $(4, 12)$ has a relatively small extension towards higher Q_{12}^2 for low Q_4^2, but in this case one would be more inclined to say this extension is simply just an extension, rather than a nearly-separate entity such as the tail in $(6, 12)$. Finally, we have distributions like $(4, 11)$, where the distribution seems to point in a certain direction (in this case toward the origin), but where an extension does not seem to exist. In the captions to the figures of these distributions (figures 19 through 51), we make note of any existences of "tails", "extensions", or even when the distributions as wholes point in a certain direction. This analysis may seem arbitrary, especially for cases such as $(4, 11)$, but it will be shown later that as Q_6^2 increases, the $l \neq 6$ harmonics decrease or increase according to tendencies we note in these distributions.

In addition to tails or extensions, the distributions plotted in fig. 19-51 differ from the simple distributions in figures 16 and 17 in other ways. Most notable is the distribution of $(5, 6)$, which seems to consist of parallel bands of a negative slope; we shall see that each band represents configurations of a different coordination number. The distribution of $(6, 11)$, in addition to having a prominent high-Q_6^2 tail, has a body that seems to point towards the origin.

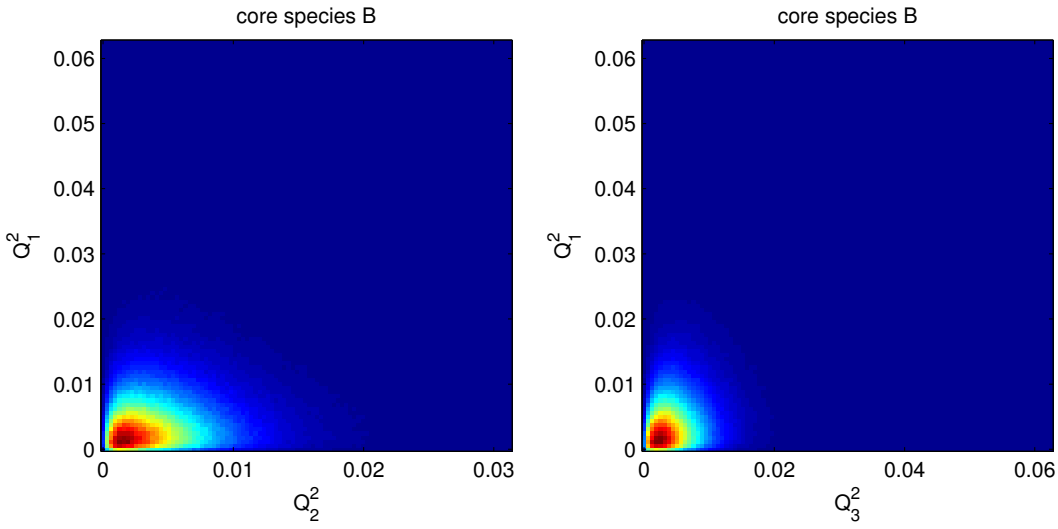

Figure 19: Two-harmonic pseudocolor plot for $(1, 2)$ and $(1, 3)$ for configurations with type-B core particles. See text for plotting information. Both distributions seem ordinary except that they are very close to the origin and that their outward fronts seem perpendicular to the origin.

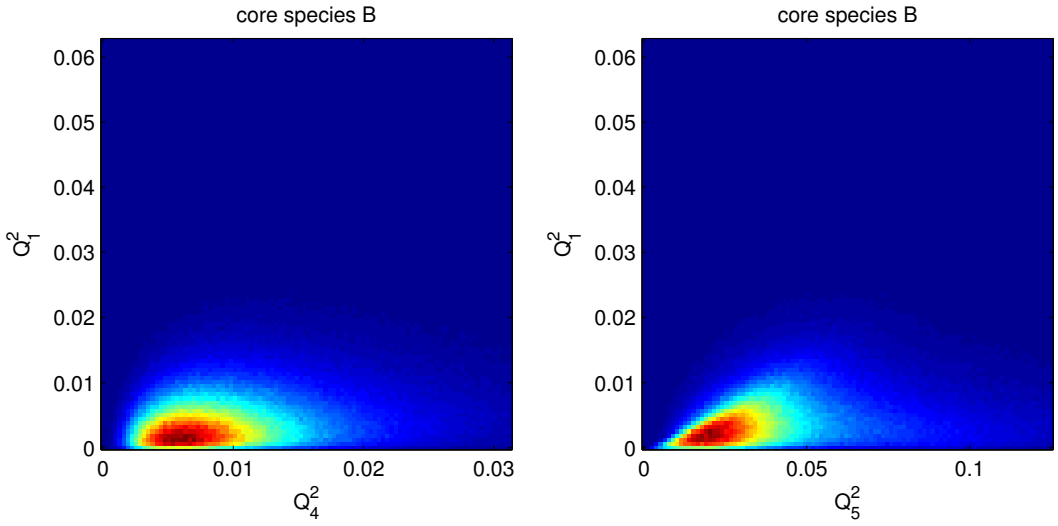

Figure 20: Two-harmonic pseudocolor plot for $(1, 4)$ and $(1, 5)$ for configurations with type-B core particles. See text for plotting information. The $(1, 4)$ plot seems ordinary but the $(1, 5)$ plot seems to have a linear side that points out from the origin, suggesting that as $Q_5^2 \to 0$, $Q_1^2 \to 0$.

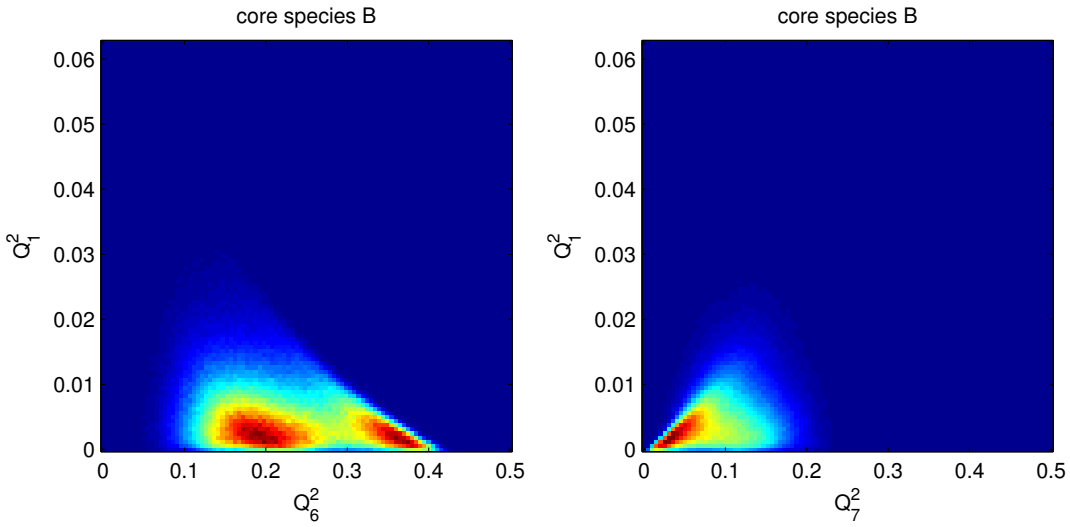

Figure 21: Two-harmonic pseudocolor plot for $(1,6)$ and $(1,7)$ for configurations with type-B core particles. See text for plotting information. The $(1,6)$ distribution has two peaks, with one peak tending towards $Q_1^2 = 0$ as Q_6^2 increases. The $(1,7)$ distribution has $Q_1^2 \to 0$ for $Q_7^2 \to 0$ and does not share the round shape of the $(1,2)$, $(1,3)$, or $(1,4)$ distributions. Specifically, $(1,7)$ extends out towards high Q_7^2 and low Q_1^2.

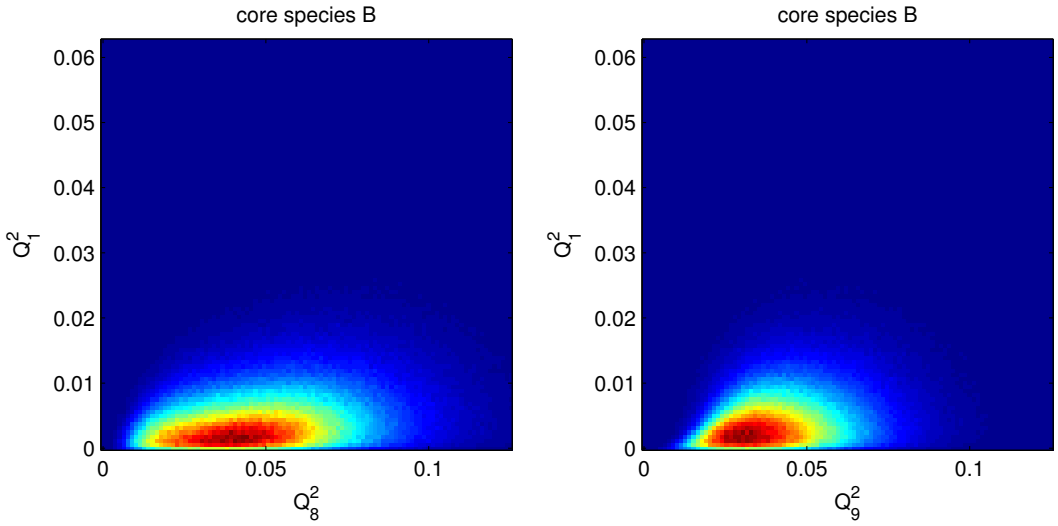

Figure 22: Two-harmonic pseudocolor plot for $(1, 8)$ and $(1, 9)$ for configurations with type-B core particles. See text for plotting information. Both distributions are ordinary except that $(1, 9)$ shows a slight tendency to point towards the origin.

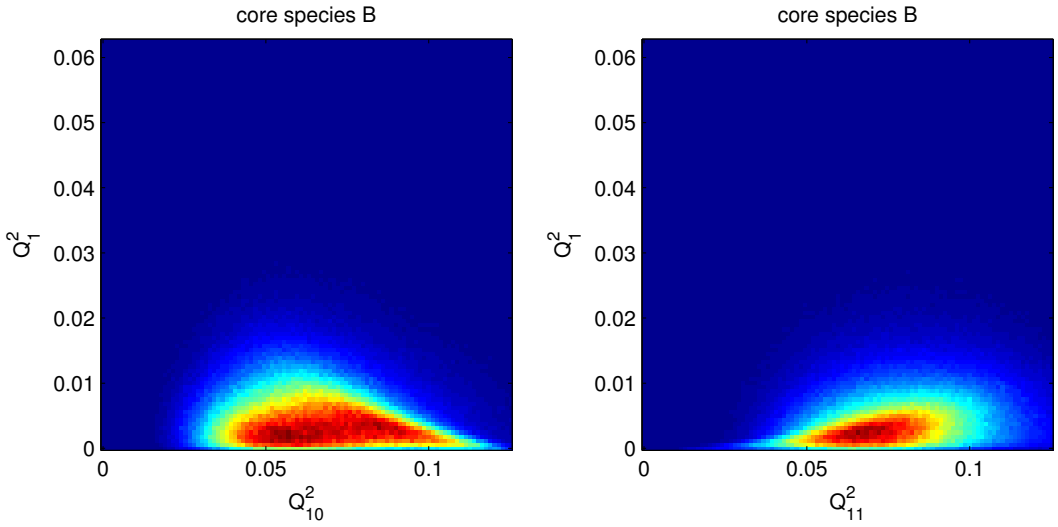

Figure 23: Two-harmonic pseudocolor plot for $(1, 10)$ and $(1, 11)$ for configurations with type-B core particles. See text for plotting information. We note that for $(1, 10)$, $Q_1^2 \to 0$ as Q_{10}^2 increases, and that $(1, 11)$ shows a slight tendency to point toward the origin.

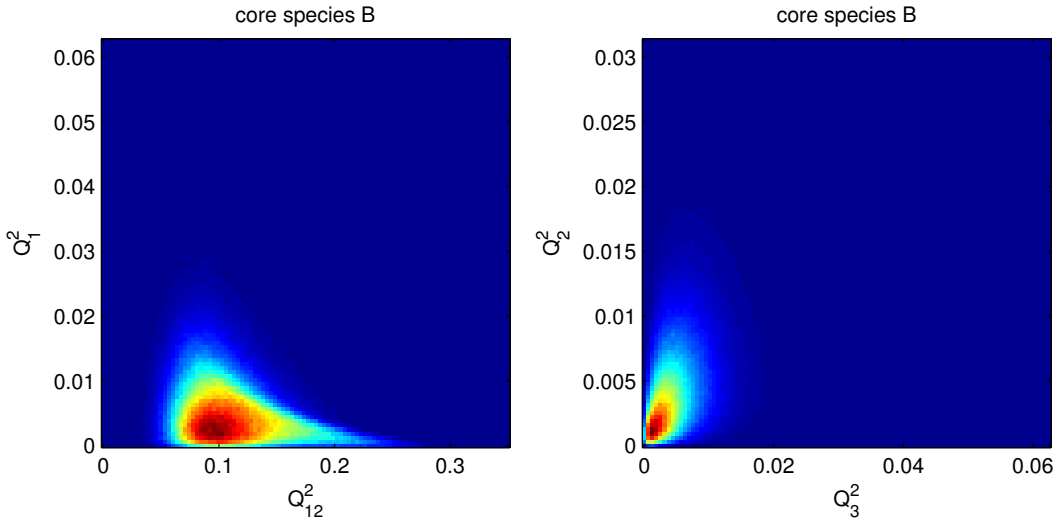

Figure 24: Two-harmonic pseudocolor plot for $(1, 12)$ and $(2, 3)$ for configurations with type-B core particles. See text for plotting information. $(1, 12)$ seems to extend to high Q_1^2 for small Q_{12}^2 more than expected, and as Q_{12}^2 increases, $Q_1^2 \to 0$. $(2, 3)$ seems unremarkable.

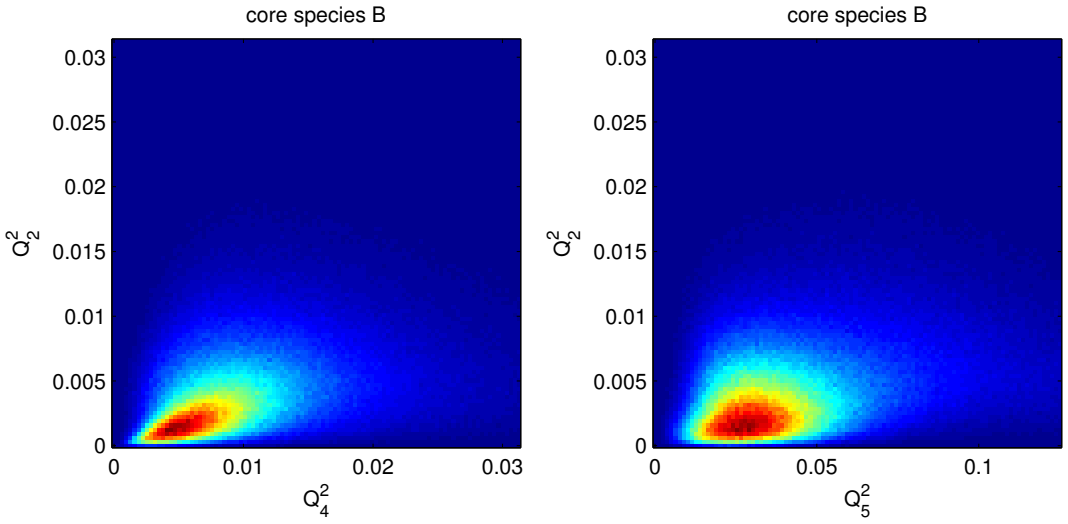

Figure 25: Two-harmonic pseudocolor plot for $(2, 4)$ and $(2, 5)$ for configurations with type-B core particles. See text for plotting information. $(2, 4)$ shows a slight tendency to point toward the origin, and the $(2, 5)$ distribution's lower-Q_5^2 side seems unusually linear.

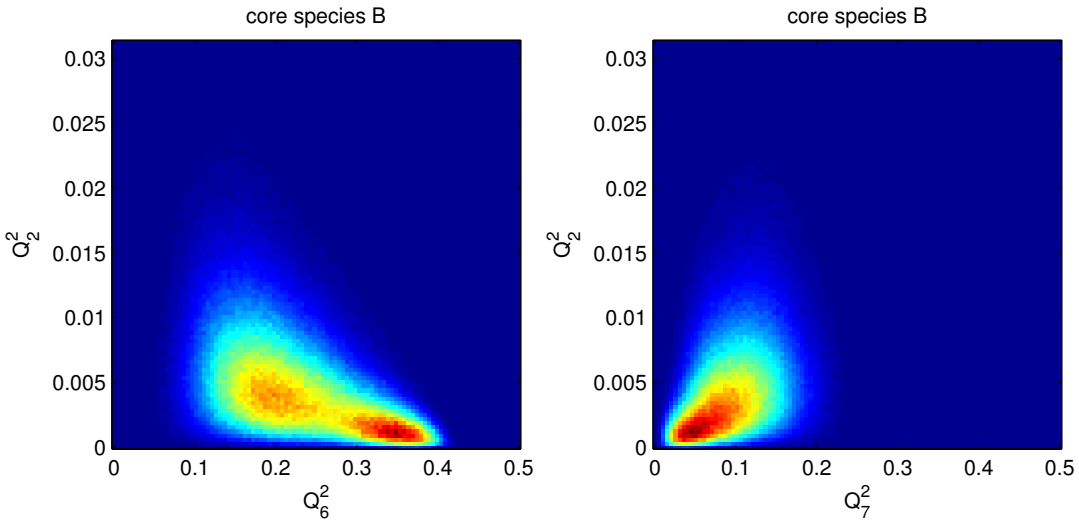

Figure 26: Two-harmonic pseudocolor plot for $(2, 6)$ and $(2, 7)$ for configurations with type-B core particles. See text for plotting information. $(2, 6)$ seems to have two peaks, one for which $Q_2^2 \to 0$ as Q_6^2 increases. $(2, 7)$ seems to point toward the origin, but it also seems to extend towards higher Q_2^2 while keeping the same Q_7^2 rather than extending outwards for both harmonics.

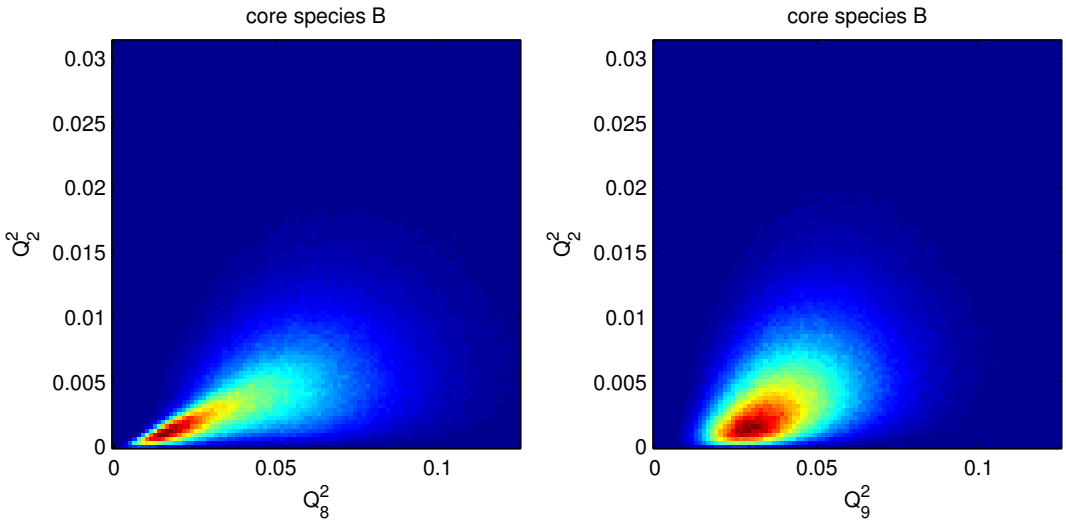

Figure 27: Two-harmonic pseudocolor plot for $(2, 8)$ and $(2, 9)$ for configurations with type-B core particles. See text for plotting information. $(2, 8)$ points sharply towards the origin, but spreads out significantly in the other direction. The lower-Q_9^2 side of the $(2, 9)$ distribution seems more linear than expected.

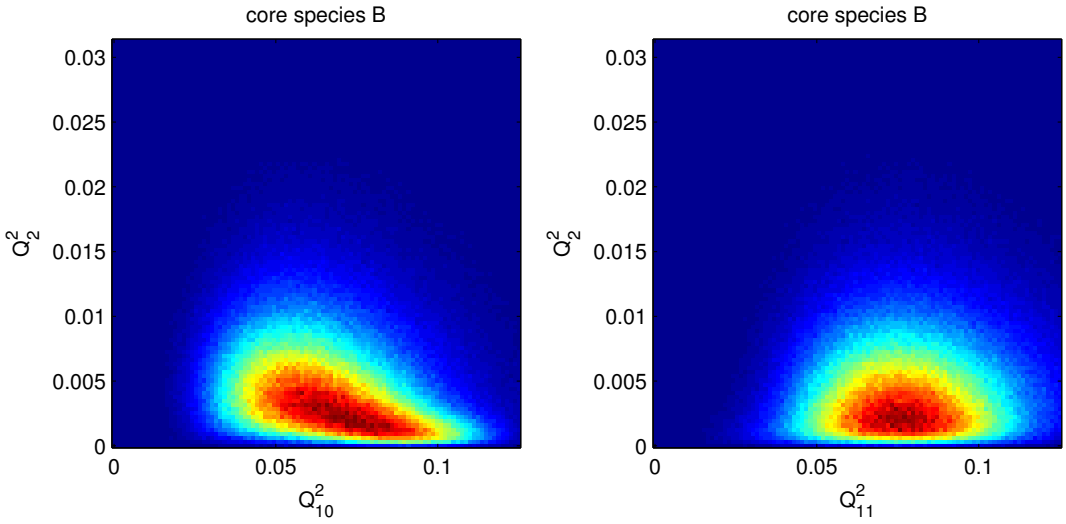

Figure 28: Two-harmonic pseudocolor plot for $(2, 10)$ and $(2, 11)$. The $(2, 10)$ distribution protrudes to greater Q_{10}^2, with a slight decrease in Q_2^2. The $(2, 11)$ seems almost symmetrical on the Q_{11}^2 axis about its mean.

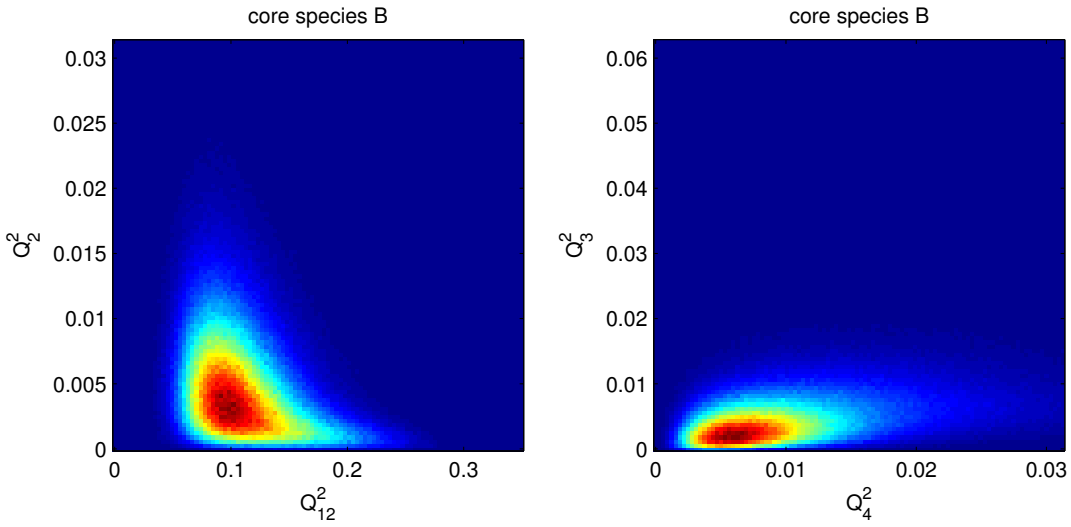

Figure 29: Two-harmonic pseudocolor plot for $(2, 12)$ and $(3, 4)$ for configurations with type-B core particles. See text for plotting information. $(2, 12)$ protrudes towards high Q_2^2 for low Q_{12}^2 and towards high Q_{12}^2 for low Q_2^2. The $(3, 4)$ distribution seems ordinary.

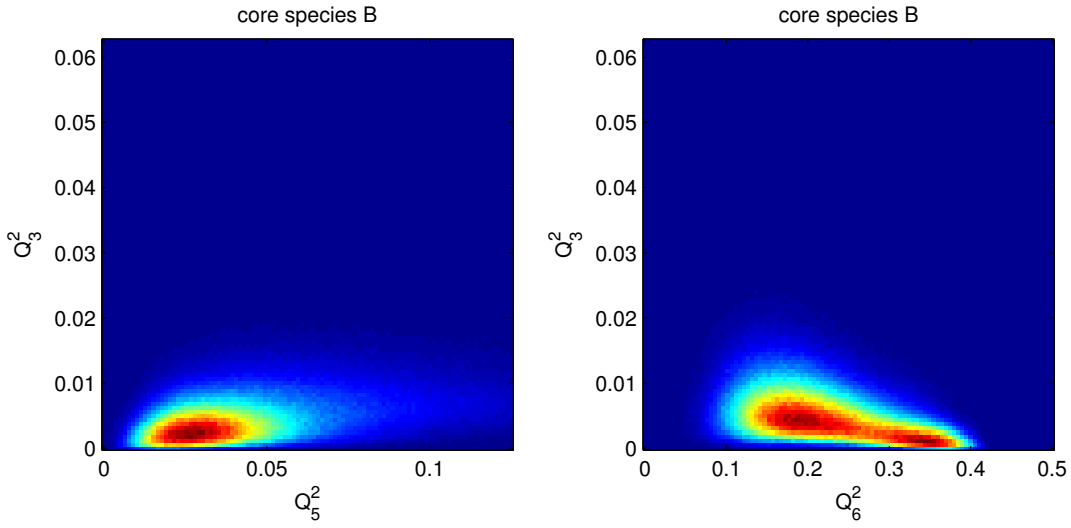

Figure 30: Two-harmonic pseudocolor plot for $(3, 5)$ and $(3, 6)$ for configurations with type-B core particles. See text for plotting information. The $(3, 5)$ plot seems ordinary, while the $(3, 6)$ plot seems to have two peaks in which one has Q_3^2 decrease while Q_6^2 increases.

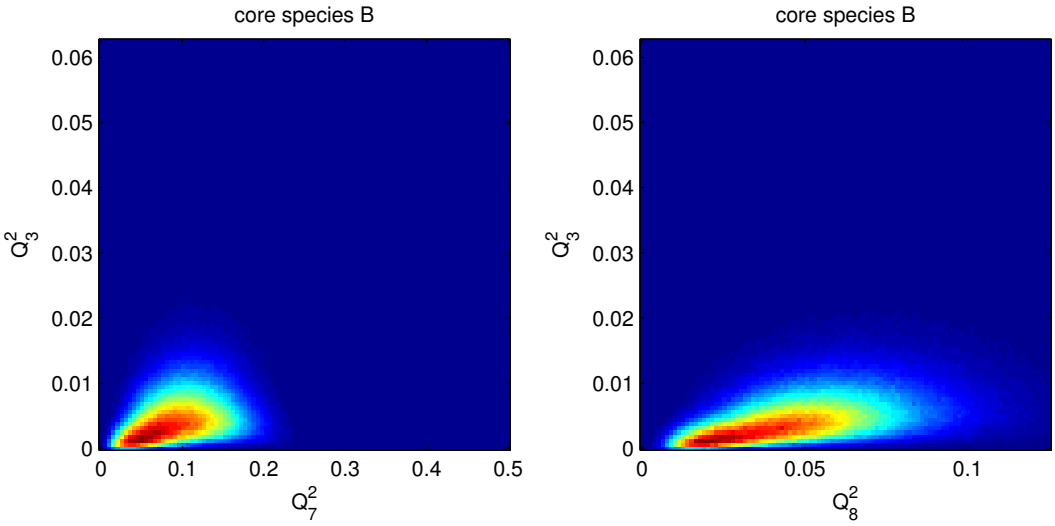

Figure 31: Two-harmonic pseudocolor plot for $(3, 7)$ and $(3, 8)$ for configurations with type-B core particles. See text for plotting information. These plots both seem to point toward the origin.

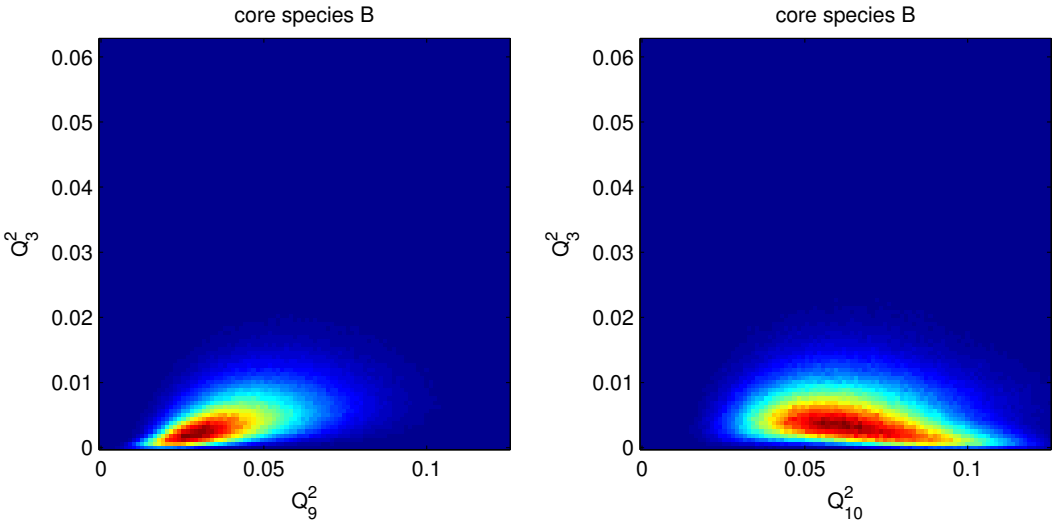

Figure 32: Two-harmonic pseudocolor plot for $(3, 9)$ and $(3, 10)$ for configurations with type-B core particles. See text for plotting information. $(3, 9)$ points toward the origin, and for $(3, 10)$, $Q_3^2 \to 0$ as Q_{10}^2 increases.

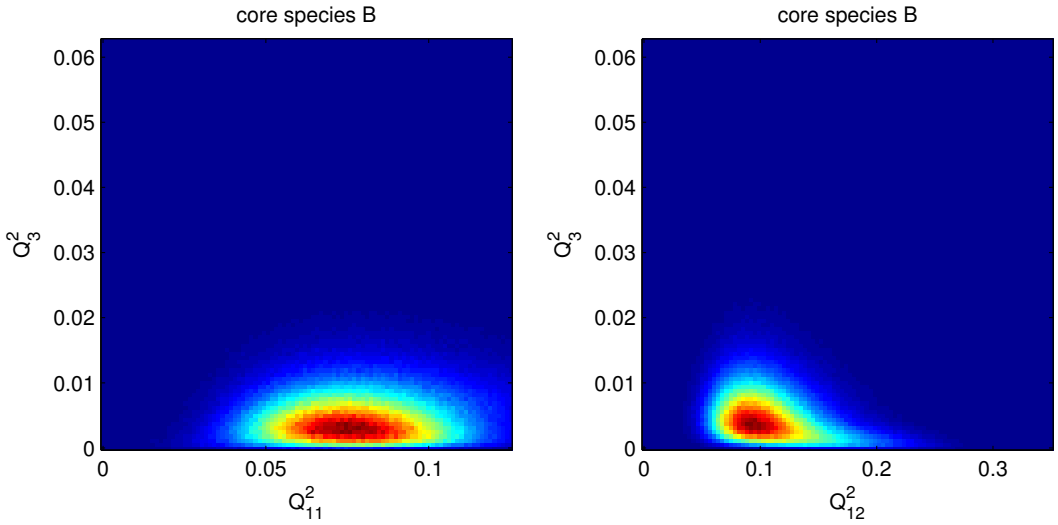

Figure 33: Two-harmonic pseudocolor plot for $(3, 11)$ and $(3, 12)$ for configurations with type-B core particles. See text for plotting information. The $(3, 11)$ distribution seems to be symmetric about a Q_{11}^2 value of about 0.075. $(3, 12)$ protrudes to higher Q_{12}^2 for low Q_3^2.

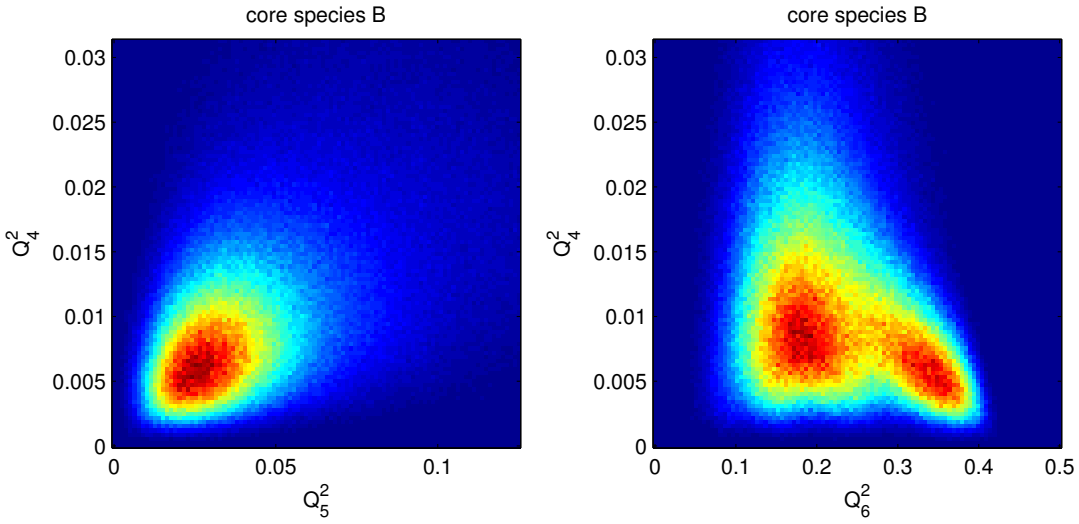

Figure 34: Two-harmonic pseudocolor plot for $(4, 5)$ and $(4, 6)$ for configurations with type-B core particles. See text for plotting information. $(4, 5)$ seems unremarkable, but $(4, 6)$ clearly shows two peaks, of which one has Q_4^2 decrease as Q_6^2 increases.

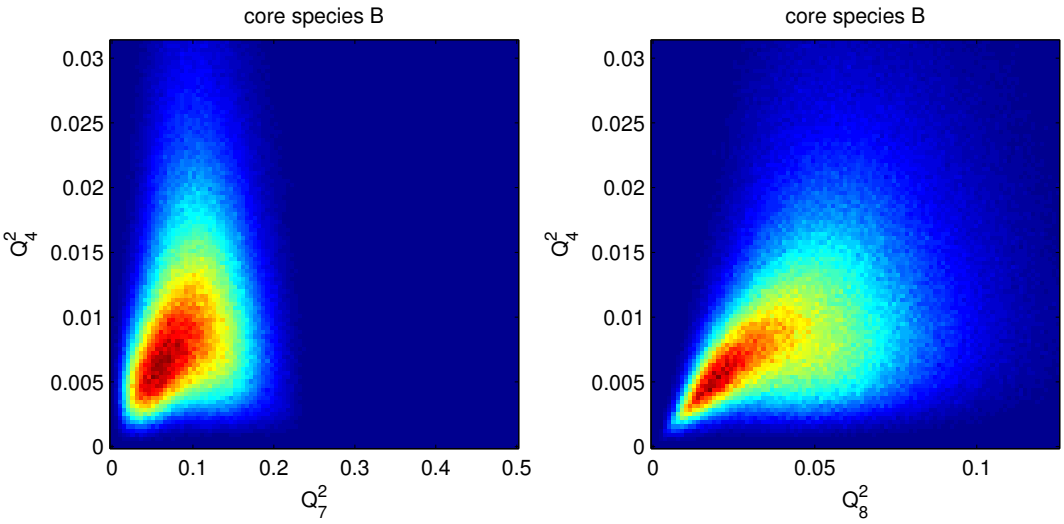

Figure 35: Two-harmonic pseudocolor plot for $(4, 7)$ and $(4, 8)$ for configurations with type-B core particles. See text for plotting information. $(4, 7)$ points toward the origin and extends to higher Q_4^2 without a shift in the average Q_7^2 values. $(4, 8)$ points sharply toward the origin.

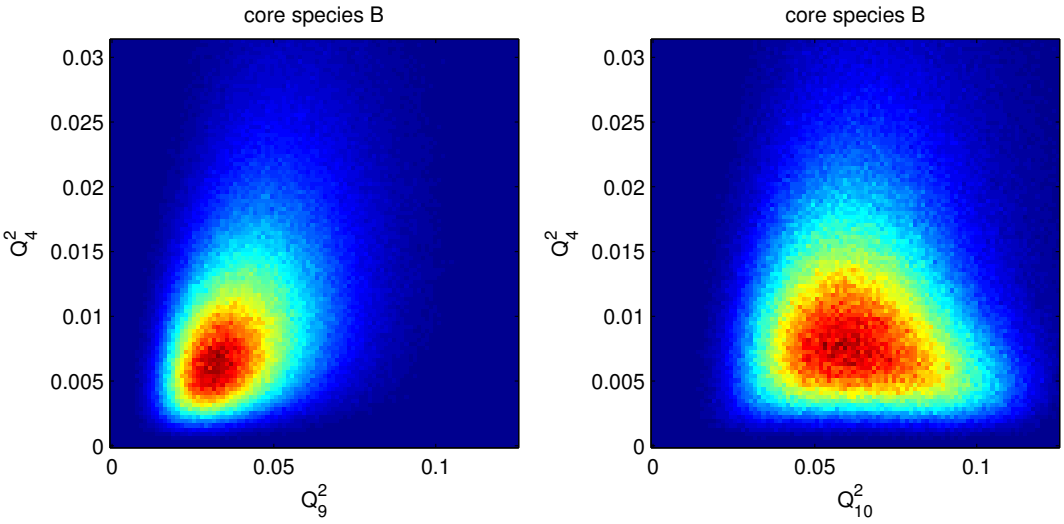

Figure 36: Two-harmonic pseudocolor plot for $(4, 9)$ and $(4, 10)$ for configurations with type-B core particles. See text for plotting information. $(4, 9)$ seems unremarkable. $(4, 10)$ protrudes slightly toward higher Q_{10}^2 for low Q_4^2.

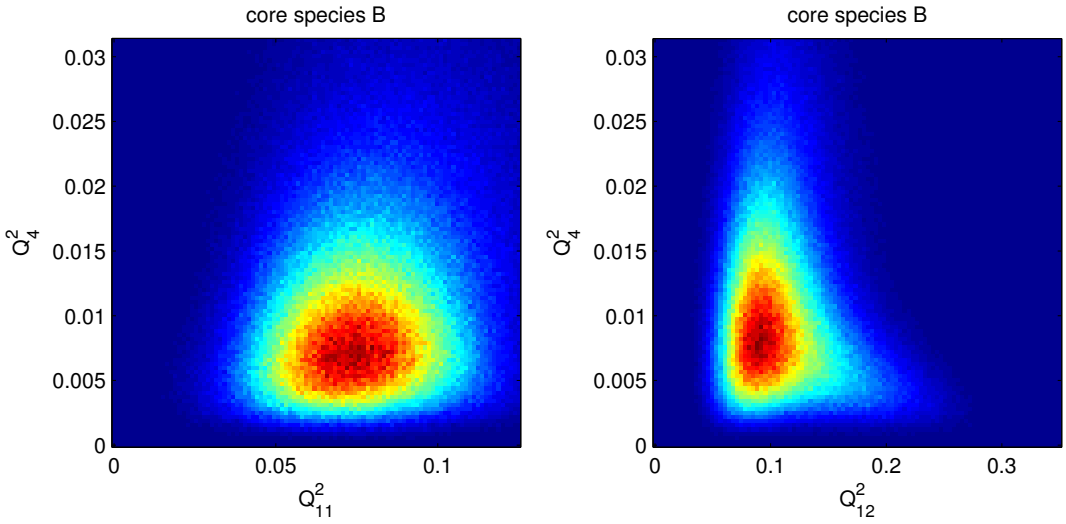

Figure 37: Two-harmonic pseudocolor plot for $(4, 11)$ and $(4, 12)$ for configurations with type-B core particles. See text for plotting information. $(4, 11)$ seems unremarkable. $(4, 12)$ protrudes toward higher Q_{12}^2 for low Q_4^2.

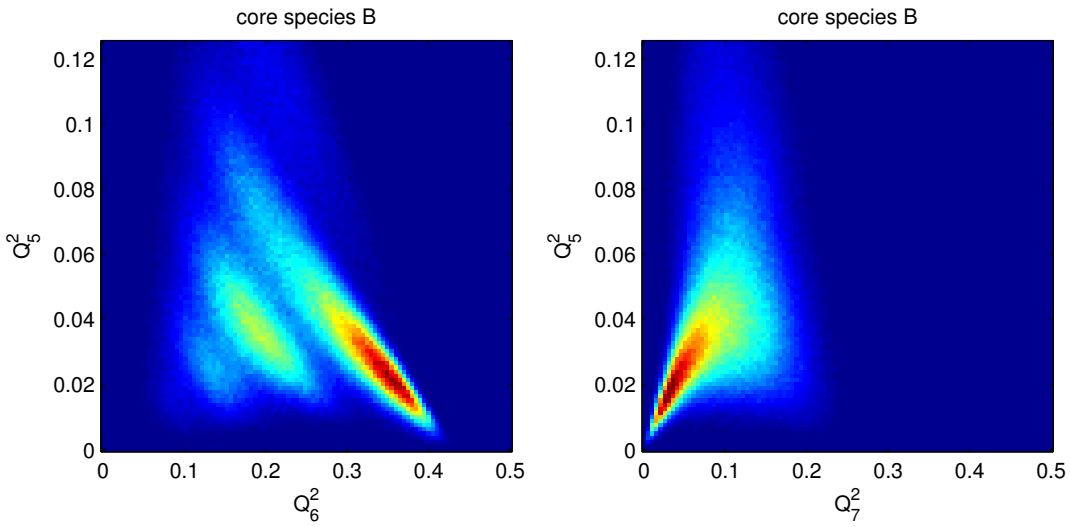

Figure 38: Two-harmonic pseudocolor plot for $(5, 6)$ and $(5, 7)$ for configurations with type-B core particles. See text for plotting information. $(5, 6)$ seems to consist of multiple bands which lie on lines of the same negative slope. The largest band has configurations congregating in the low-Q_5^2 area, in which $Q_5^2 \to 0$ as Q_6^2 increases. There appear to be four or five bands total, depending on whether the area around $Q_5^2 = 0.02$ and $Q_6^2 = 0.1$ counts as a separate band. The $(5, 7)$ distribution points sharply toward the origin and seems to extend to high Q_5^2 to a greater degree than normal.

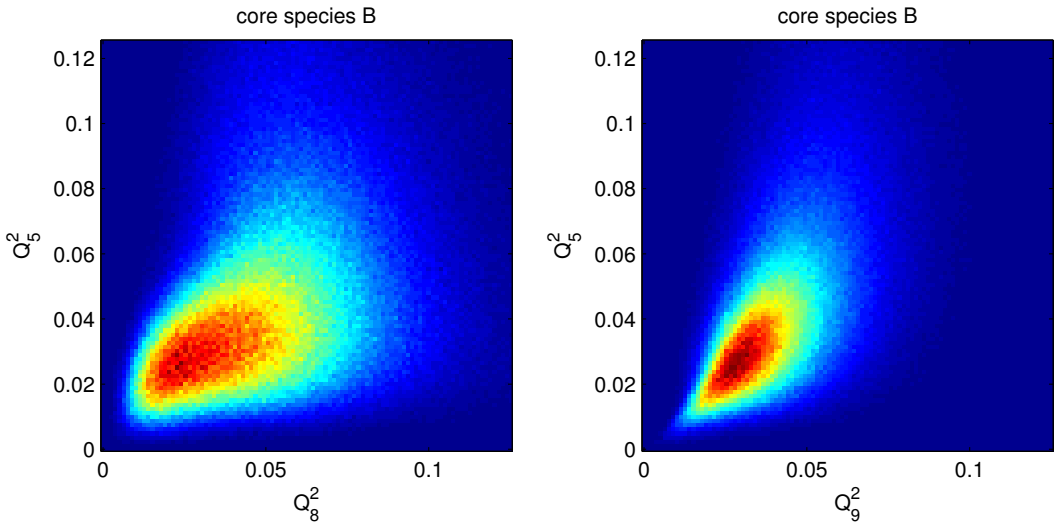

Figure 39: Two-harmonic pseudocolor plot for $(5, 8)$ and $(5, 9)$ for configurations with type-B core particles. See text for plotting information. The $(5, 8)$ distribution seems to significantly protrude toward the origin. The $(5, 9)$ distribution points toward the origin more sharply.

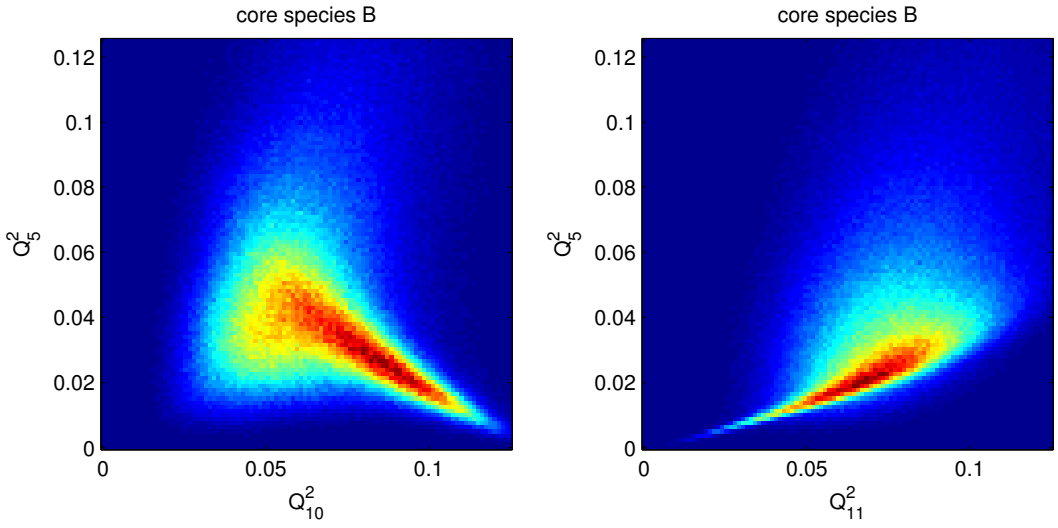

Figure 40: Two-harmonic pseudocolor plot for $(5, 10)$ and $(5, 11)$ for configurations with type-B core particles. See text for plotting information. Both plots have regions which grow sharper as $Q_5^2 \to 0$; for $(5, 10)$, Q_{10}^2 increases as Q_5^2 decreases, and for $(5, 11)$, as $Q_5^2 \to 0$, $Q_{11}^2 \to 0$.

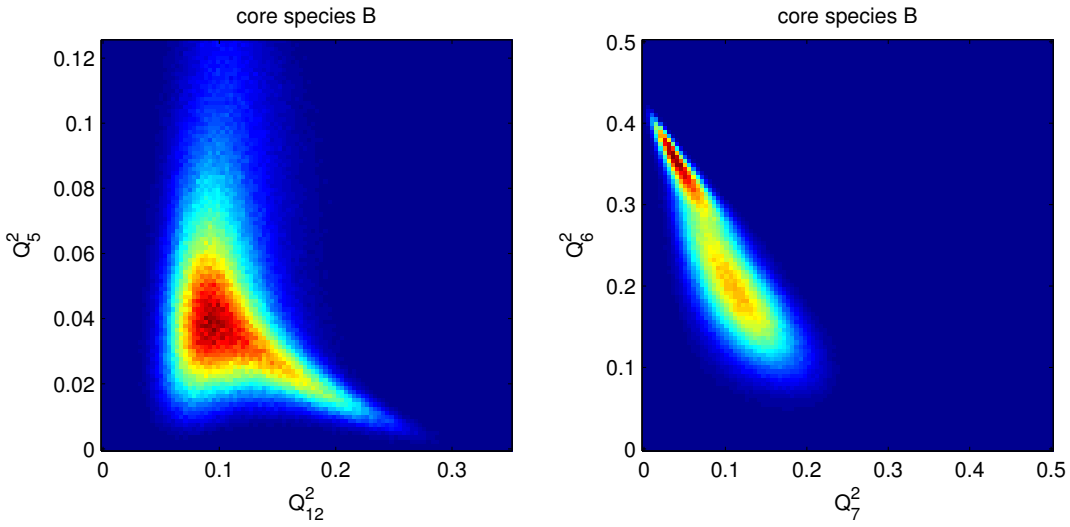

Figure 41: Two-harmonic pseudocolor plot for $(5, 12)$ and $(6, 7)$ for configurations with type-B core particles. See text for plotting information. $(5, 12)$ has a region where $Q_5^2 \to 0$ as Q_{12}^2 increases. $(6, 7)$ seems to have two peaks, with one having the property that $Q_7^2 \to 0$ as Q_6^2 increases.

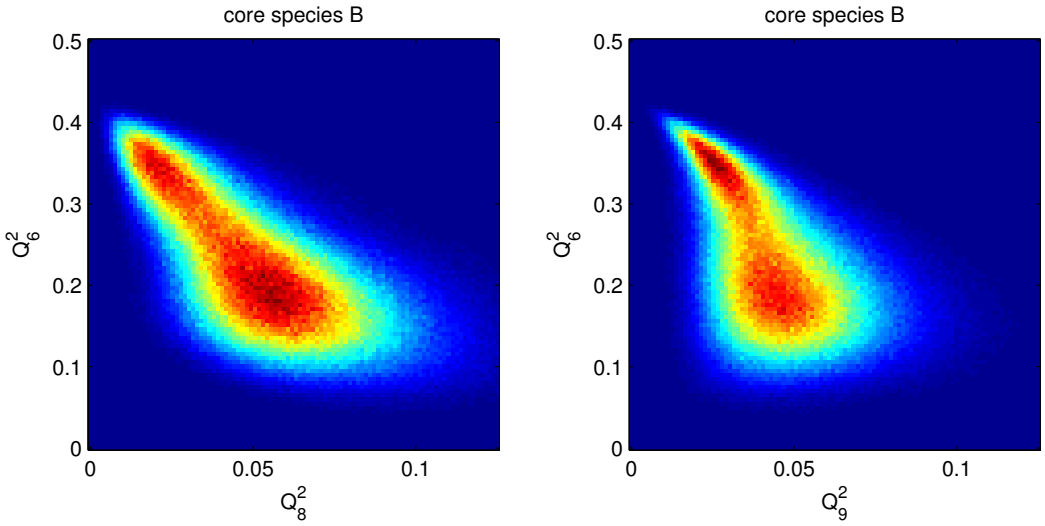

Figure 42: Two-harmonic pseudocolor plot for $(6, 8)$ and $(6, 9)$ for configurations with type-B core particles. See text for plotting information. These two distributions have timilar features, in that there appear to be two peaks, one of which has the property that Q_8^2 or $Q_9^2 \to 0$ as Q_6^2 increases.

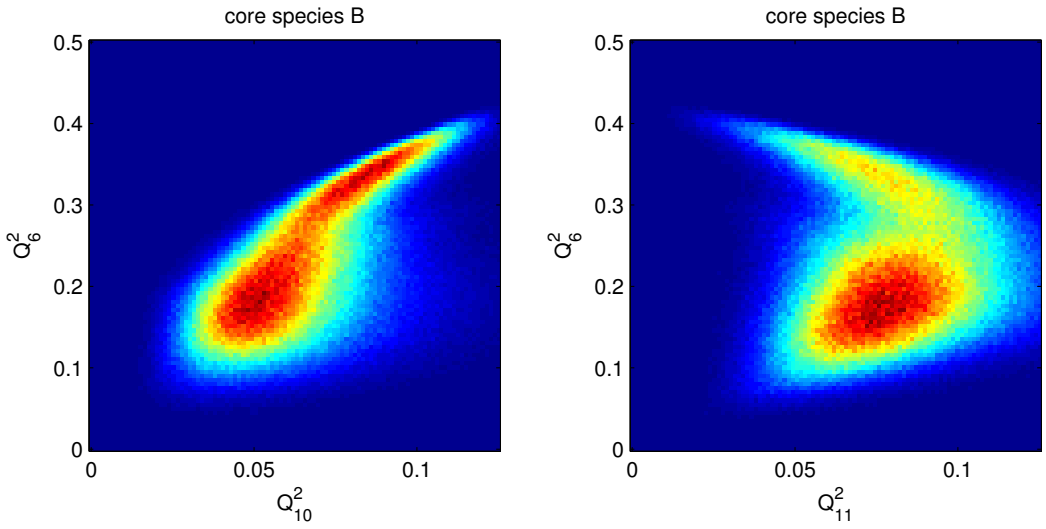

Figure 43: Two-harmonic pseudocolor plot for $(6, 10)$ and $(6, 11)$ for configurations with type-B core particles. See text for plotting information. For each of these graphs, as Q_6^2 increases, Q_{10}^2 increases and Q_{11}^2 decreases. The $(6, 11)$ distribution has a lower part that seems to point toward the origin.

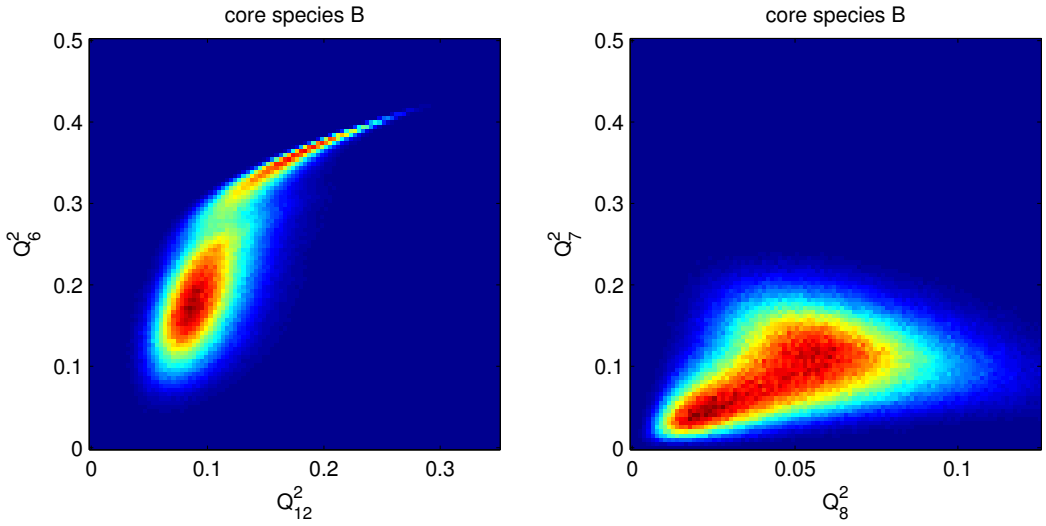

Figure 44: Two-harmonic pseudocolor plot for $(6, 12)$ and $(7, 8)$ for configurations with type-B core particles. See text for plotting information. The $(6, 12)$ distribution resembles an ellipse and a tail in a tadpole shape. As Q_6^2 increases, Q_{12}^2 increases. $(7, 8)$ seems to protrude toward the origin.

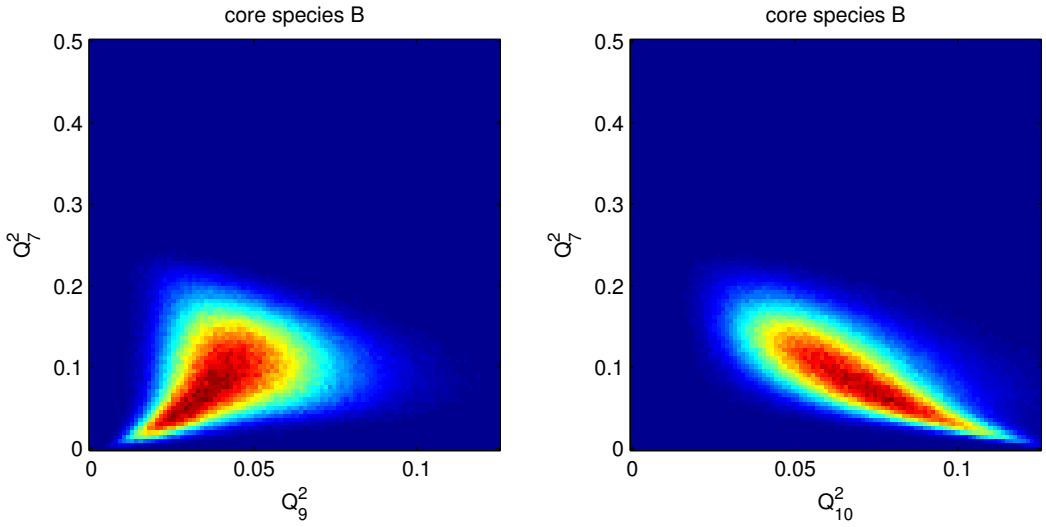

Figure 45: Two-harmonic pseudocolor plot for $(7, 9)$ and $(7, 10)$ for configurations with type-B core particles. See text for plotting information. $(7, 9)$ has a protrusion where Q_7^2 and Q_9^2 go to zero together. In $(7, 10)$, $Q_7^2 \to 0$ as Q_{10}^2 increases.

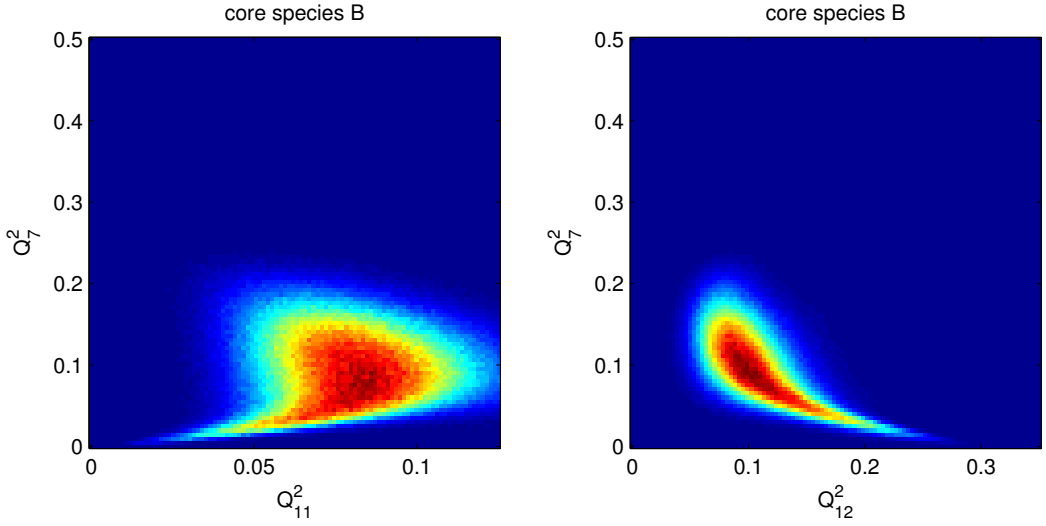

Figure 46: Two-harmonic pseudocolor plot for $(7, 11)$ and $(7, 12)$ for configurations with type-B core particles. See text for plotting information. Both distributions have a main body with a thin protrusion for $Q_7^2 \to 0$. For $(7, 11)$, both Q_7^2 and Q_{11}^2 go to zero together. For $(7, 12)$, $Q_7^2 \to 0$ as Q_{12}^2 increases.

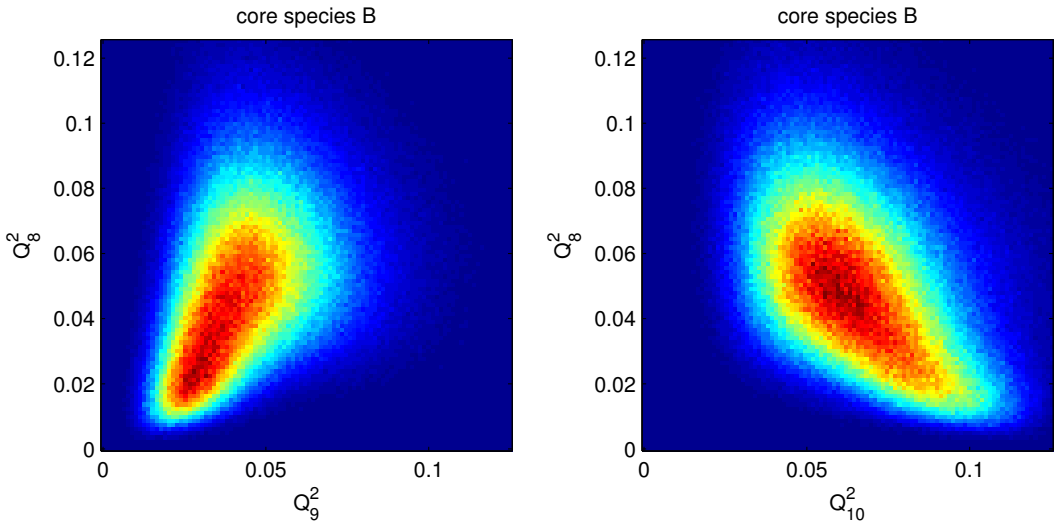

Figure 47: Two-harmonic pseudocolor plot for $(8, 9)$ and $(8, 10)$ for configurations with type-B core particles. See text for plotting information. These two distributions seem ordinary except for a protrusion toward the origin for $(8, 9)$ and a protrusion toward high Q_{10}^2 and low Q_8^2 for $(8, 10)$.

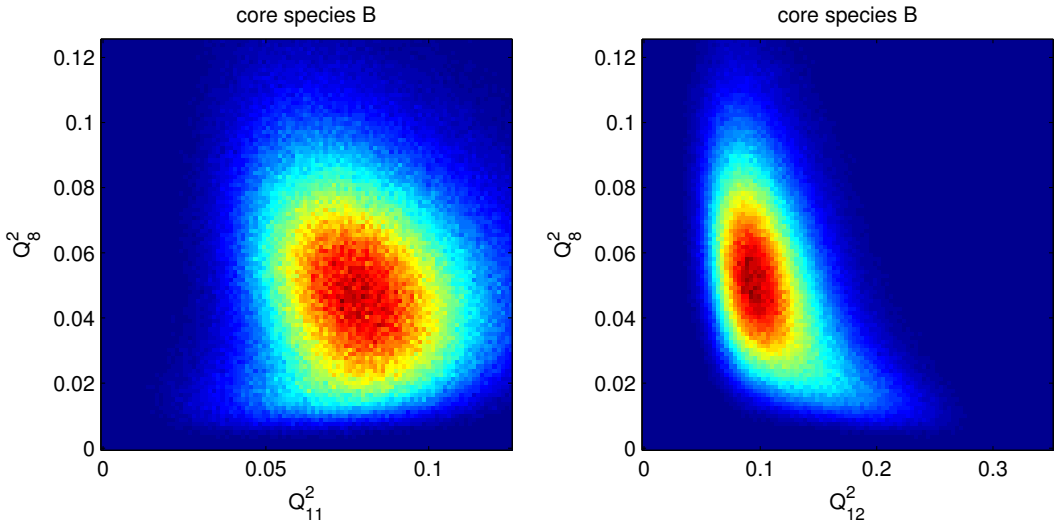

Figure 48: Two-harmonic pseudocolor plot for $(8, 11)$ and $(8, 12)$ for configurations with type-B core particles. See text for plotting information. $(8, 11)$ seems ordinary except for a very slight protrusion toward low Q_{11}^2 for low Q_8^2. $(8, 12)$ is also ordinary but it has a more significant protrusion toward low Q_8^2 and high Q_{12}^2.

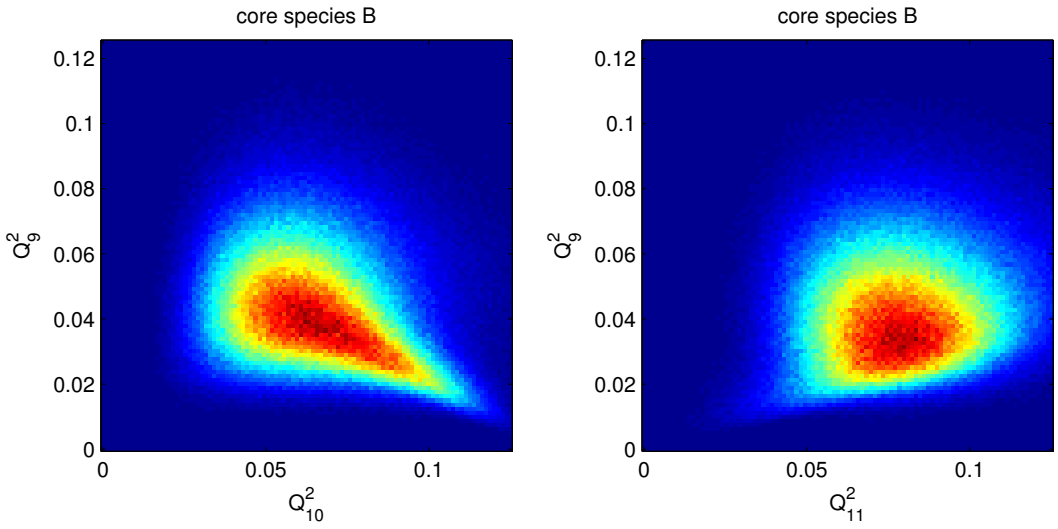

Figure 49: Two-harmonic pseudocolor plot for $(9, 10)$ and $(9, 11)$ for configurations with type-B core particles. See text for plotting information. $(9, 10)$ seems ordinary except for a sharp protrusion toward low Q_9^2 and high Q_{10}^2. $(9, 11)$ also seems ordinary, with a very slight protrusion toward the origin.

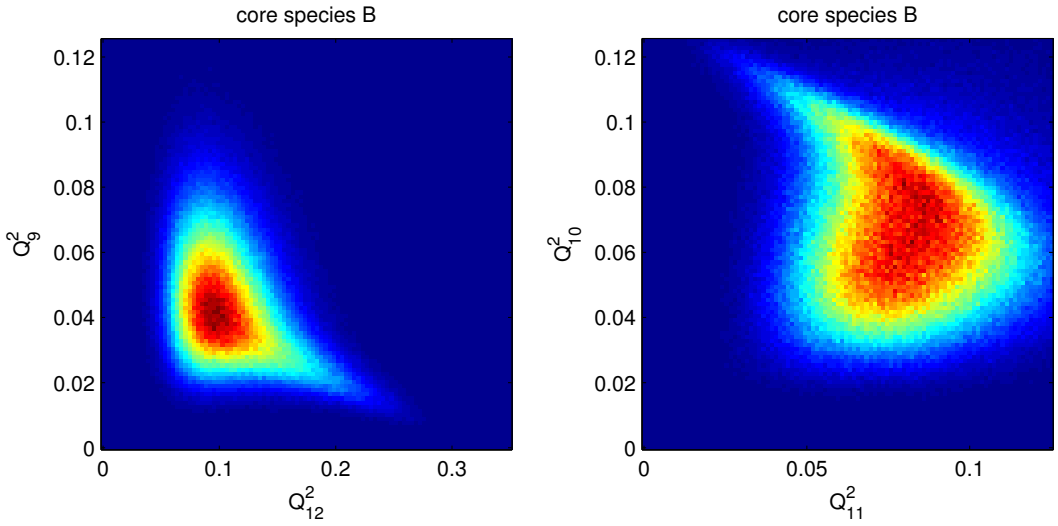

Figure 50: Two-harmonic pseudocolor plot for $(9, 12)$ and $(10, 11)$ for configurations with type-B core particles. See text for plotting information. $(9, 12)$ has a protrusion toward low Q_9^2 and high Q_{12}^2, and $(10, 11)$ protrudes toward low Q_{11}^2 for high Q_{10}^2.

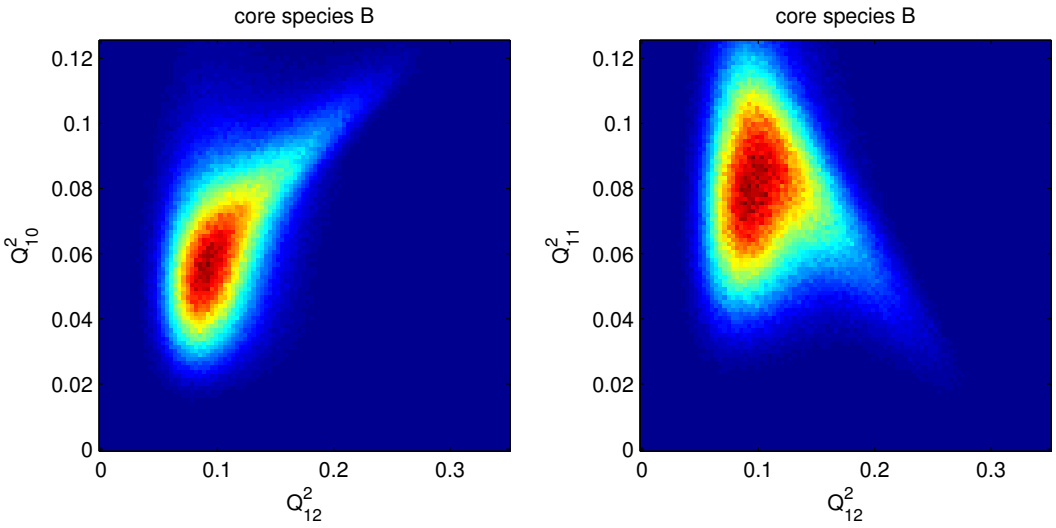

Figure 51: Two-harmonic pseudocolor plot for $(10, 12)$ and $(11, 12)$ for configurations with type-B core particles. See text for plotting information. $(10, 12)$ is ordinary except for a protrusion toward high Q^2_{10} and high Q^2_{12}. For $(11, 12)$, on the higher-Q^2_{12} side there is a protrusion which decreases in Q^2_{11} as Q^2_{12} increases.

3.6 Two-harmonic distributions: Type-A configurations

We plot a few of the more notable type-A two-harmonic distributions in figures 52, 53, 54, and 55. In fig. 52, we note that $(7, 10)$ and $(7, 11)$ both point toward higher Q^2_7 for lower Q^2_{10} or Q^2_{11}. This seems the extent to which any tail-like behavior appears for type-A distributions (with the exception of $(6, 7)$ below.) This is notable because here, with type-A configurations, the distribution thins toward greater Q^2_7, while the tails in the type-B configurations for figures 19-51 thin as $Q^2_7 \to 0$. In figures 53 and 54, we notice strong band structure characteristics in $(5, 6)$ and possible related characteristics in the bumpy lower-Q^2_4 side of $(4, 6)$ and a notch in the lower-Q^2_2 side of $(2, 6)$, though $(3, 6)$ does not appear to show such structure.

Most importantly, we note that $(6, 7)$ shows a tail that extends to higher Q^2_6 as $Q^2_7 \to 0$, which is notable considering that tails are present for type-B configurations but rarely for type-A configurations. We also note that the tail in $(6, 7)$ is much fainter in type-A distributions (fig. 55) than in type-B distributions (fig. 41).

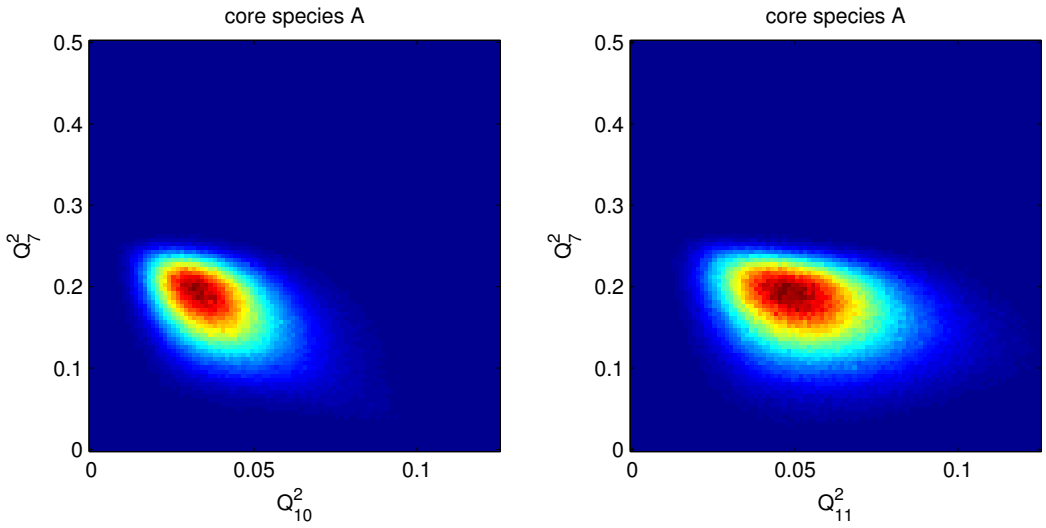

Figure 52: Two-harmonic pseudocolor plot for $(7, 10)$ and $(7, 11)$ for configurations with type-A core particles. See text for plotting information. We note that both distributions seem to point towards the area $0.2 < Q_7^2 < 0.3$ as Q_{10}^2 or Q_{11}^2 decreases.

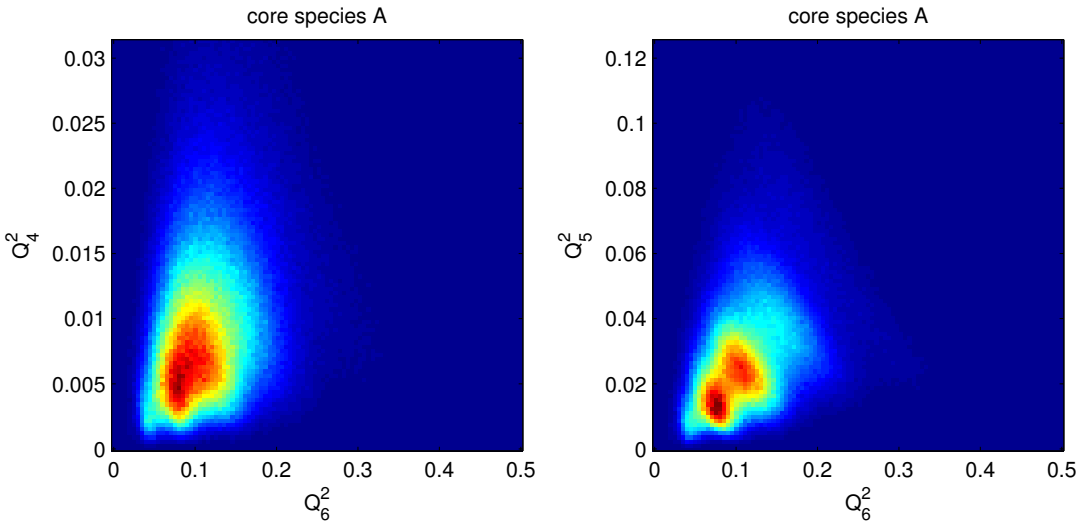

Figure 53: Two-harmonic pseudocolor plot for $(4,6)$ and $(5,6)$ for configurations with type-A core particles. See text for plotting information. We note that $(5,6)$ seems to consist of parallel bands of negative slope, as did the type-B $(5,6)$ in figure 38. The lower-Q_4^2 side of $(4,6)$ is bumpy in a way that resembles the lower-Q_4^2 side of $(5,6)$, possibly indicating a subtle band structure in $(4,6)$ as well.

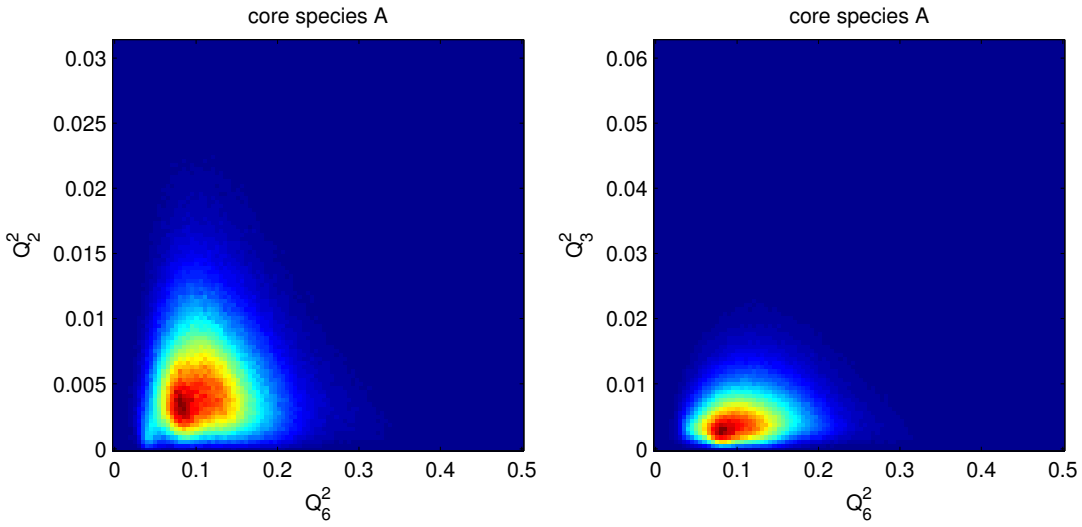

Figure 54: Two-harmonic pseudocolor plot for $(2, 6)$ and $(3, 6)$ for configurations with type-A core particles. See text for plotting information. In fig. 53 we saw a band structure in $(5, 6)$ and possibly in $(4, 6)$, so it seemed reasonable to check $(3, 6)$ and $(2, 6)$ as well. $(3, 6)$ shows no definite signs of band structure, but $(2, 6)$ has a notch on the low-Q_2^2 side.

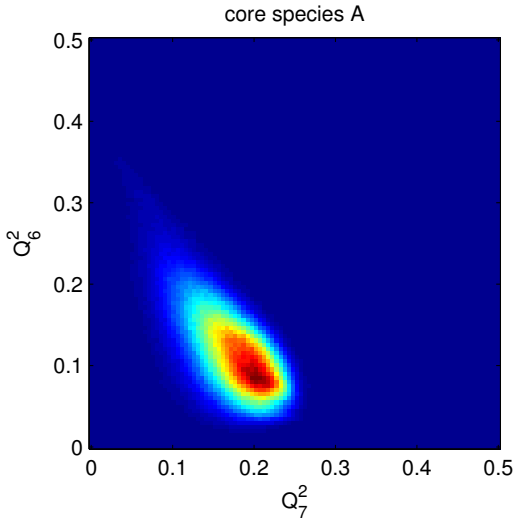

Figure 55: Two-harmonic pseudocolor plot for $(6, 7)$ for configurations with type-A core particles. See text for plotting information. This plot has a faint but clear tail that extends toward higher Q_6^2 as $Q_7^2 \to 0$.

3.7 Two-harmonic distributions: Coordination number

To consider the effect of coordination number on the two-harmonic distributions, we first present the distribution of coordination numbers in fig. 56. To consider the distributions of the various combinations of type-A and type-B atoms in the first shell, we show the distributions of the number of type-A shell atoms when the coordination number is 12; these distributions are also plotted in fig. 56. We see that type-A configurations most frequently have a coordination number of 13 or 14. Type-B configurations most frequently have 12 as their coordination number. It is likely type-A particles have larger coordination numbers because they are the larger atoms in the system and thus have more surface area than the average atom. One would expect the coordination number of type-B configurations would be less than 12 on average because optimal packing of a center sphere and a number of equally-sized "shell" spheres would require 12 shell spheres for optimal packing [2], and increasing the size of the shell spheres would only decrease the coordination number. However, these distributions were measured for the first full shell, which may be large enough to occasionally allow more than 12 atoms within the shell radius.

The distributions of type-A shell atoms are centered about values 7 and 8 for the type-A configurations, and about values 6 and 7 for the type-B configurations. Since the type-A and type-B particles are scattered evenly throughout the system, the chance of having any one particle be type-A would be about half, and the expected distribution would be a binomial distribution centered on 6. However, the different sizes of the type-A and type-B particles alters the distribution slightly, shifting it to greater type-A shell atoms in both cases. For type-A configurations, a coordination number of 12 would be less than average, so we would need more big particles surrounding it to make up for the difference. This is true for type-B configurations too, though to a lesser extent.

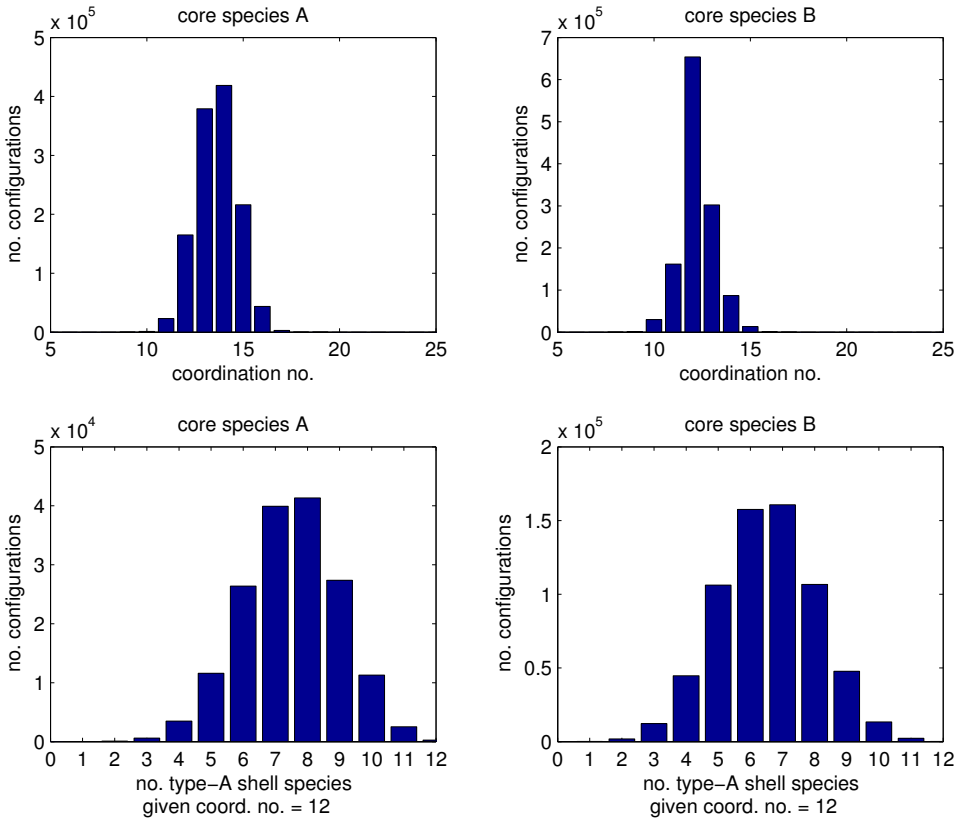

Figure 56: The top two graphs plot the distributions of the coordination numbers for each core atom species at $T = .52$. The bottom two graphs plot the number of type-A atoms in the first shell given a coordination number of 12. These graphs use the first full shell as a definition of a coordination shell.

Our first example of the effect of coordination number on the harmonics is the two-harmonic distribution $(6, 11)$ for core species B, plotted in figures 57 and 58. We plot for coordination numbers 8 through 15. Two main characteristics should be observed. First, the locations of the distributions vary quite a bit when different coordination numbers are selected. In fig. 43, we mentioned that $(6, 11)$ had a lower-Q_6^2 portion that seemed to point toward the origin. It is possible that features that seem to point in a certain direction are instead the result of the superposition of distributions of differing coordination numbers. The center of the non-tail portion of the coord. no. 12 distribution and the centers of the distributions for coord. nos. 13 through 15 together have a tendency to move toward the origin as we increase coordination number. Summing up distributions whose centers shift toward the origin as coord. no. increases may explain the origin-pointing behavior of the $(6, 11)$ distribution. The second notable characteristic is that these distributions, especially for coord. no. 12, are not as simple as the $T = 50000$ distributions in figures 16 and 17, suggesting that one cannot always break up a complex distribution into simple ones through coordination number.

Our next example of coordination number dependence is demonstrated in figures 59 and 60, in which we plot $(6, 12)$. We note that the tail in the coord. no. 12 plot is also present to a lesser degree for coord. nos. 11 and 13. In addition, categorizing by coordination number has shown that the tail is present almost entirely for coord. no. 12, but that not all coord. no. 12 configurations are part of the tail.

Finally, we examine the B-core-species plots for various coordination numbers, plotted in figures 61 and 62. For the most part, each distribution in these plots forms a separate band in the $(5, 6)$ plot in figure 38, though there seems to be direct overlap between the coord. no. 10 and coord. no. 11 distributions.

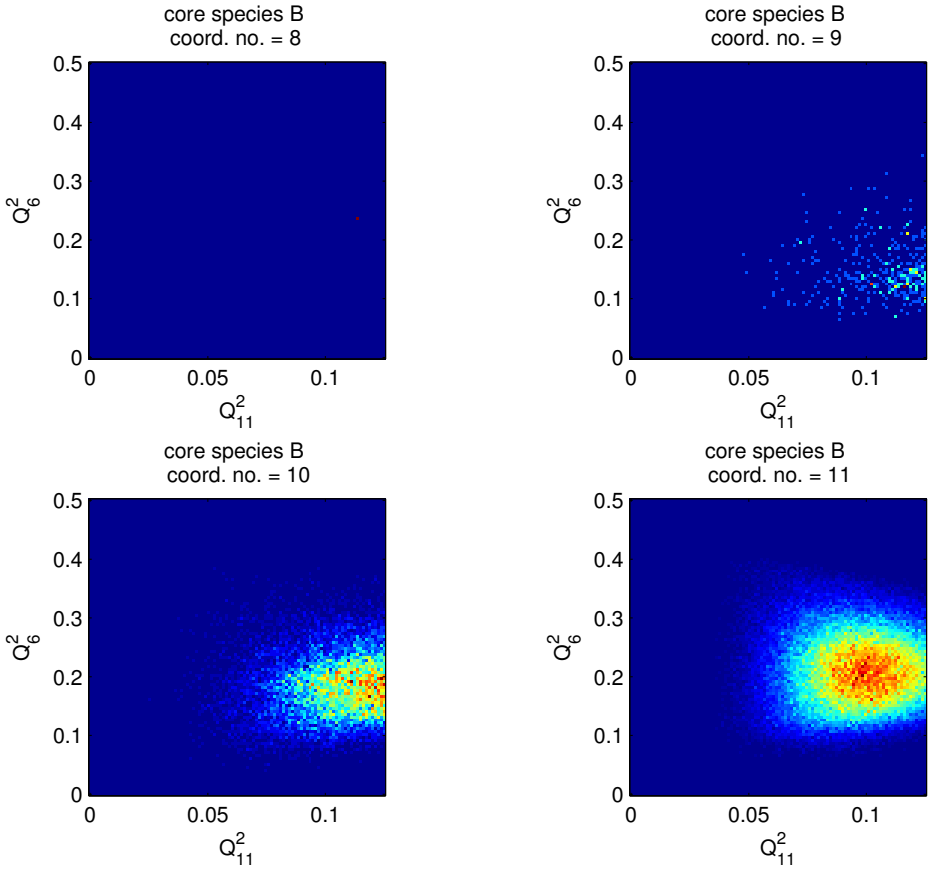

Figure 57: Here are the $(6, 11)$ two-harmonic distributions at $T = .52$ for core species B for coordination numbers 8-11. For a coordination number of 8, only eight configurations exist, only one of which is within the bounds of this plot (and this point may not be visible if the resolution is too low.) For coord. nos. 9 and 10, the distribution lies in a region partly beyond the upper Q_{11}^2 bound, which was chosen to accomodate the higher-coordination number distributions. From coord. no. 9 to coord. no. 11 we see the distributions becoming clearer, and that from what we can see these distributions are simple, i.e. they are relatively round, unimodal, and have no protuberances.

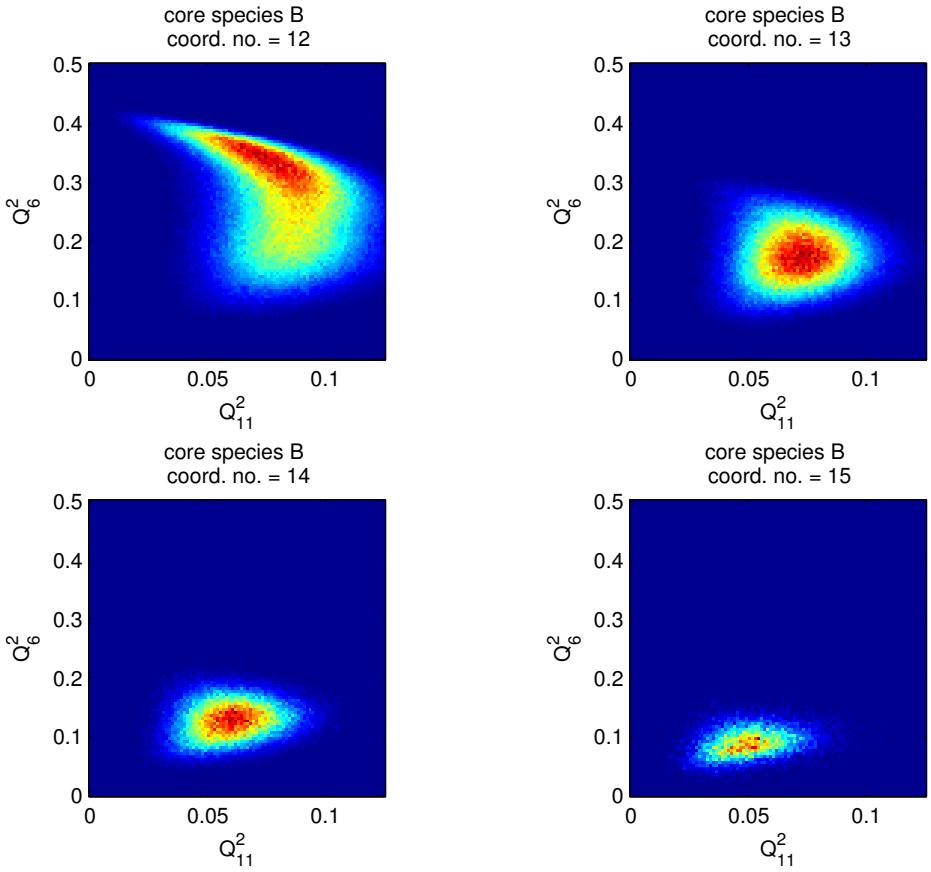

Figure 58: Here are the $(6, 11)$ two-harmonic distributions at $T = .52$ for core species B for coordination numbers 12-15. At coord. no. 12, we see a tail for large Q_6^2 which does not appear for coord. nos. 11 or 13. From coord. no. 12 to 15, we see a drop in Q_6^2 for each successive distribution.

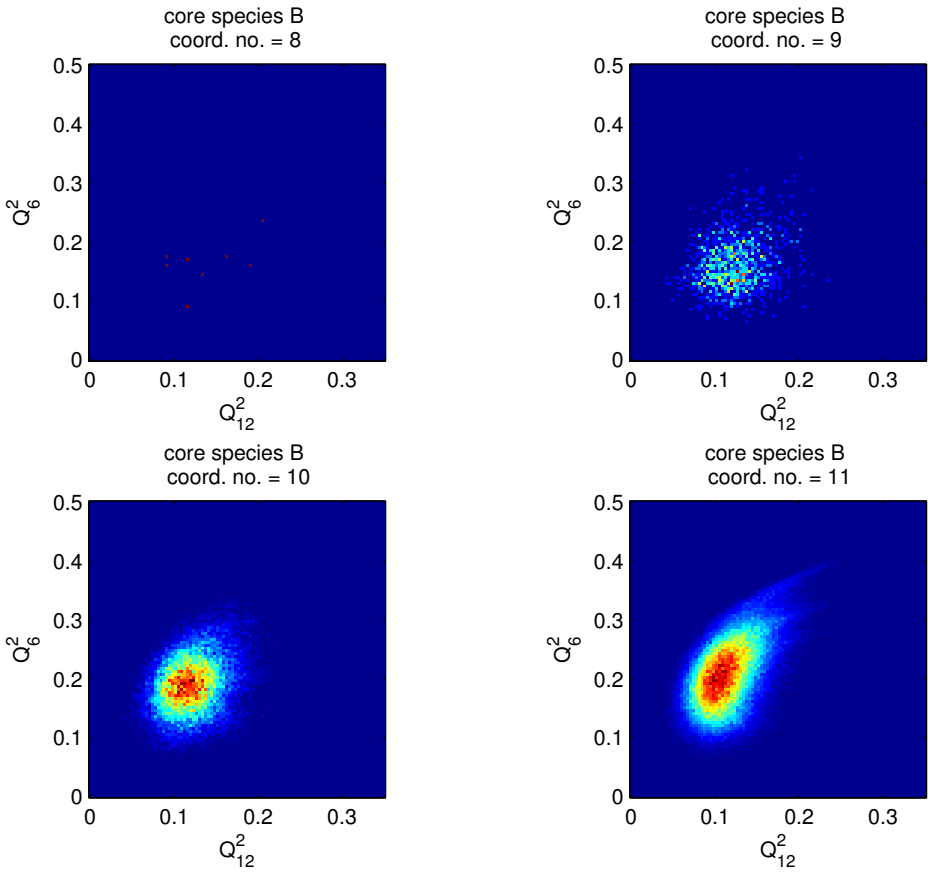

Figure 59: Here are the $(6, 12)$ two-harmonic distributions at $T = .52$ for core species B for coordination numbers 8-11. Due to sparsity, the distribution for coord. no. 8 does not show us much. Distributions for coord. nos. 9 and 10 appear to be round and featureless. For coord. no. 11 we have a more elongated distribution and a faint tail for $Q_6^2 > 0.3$.

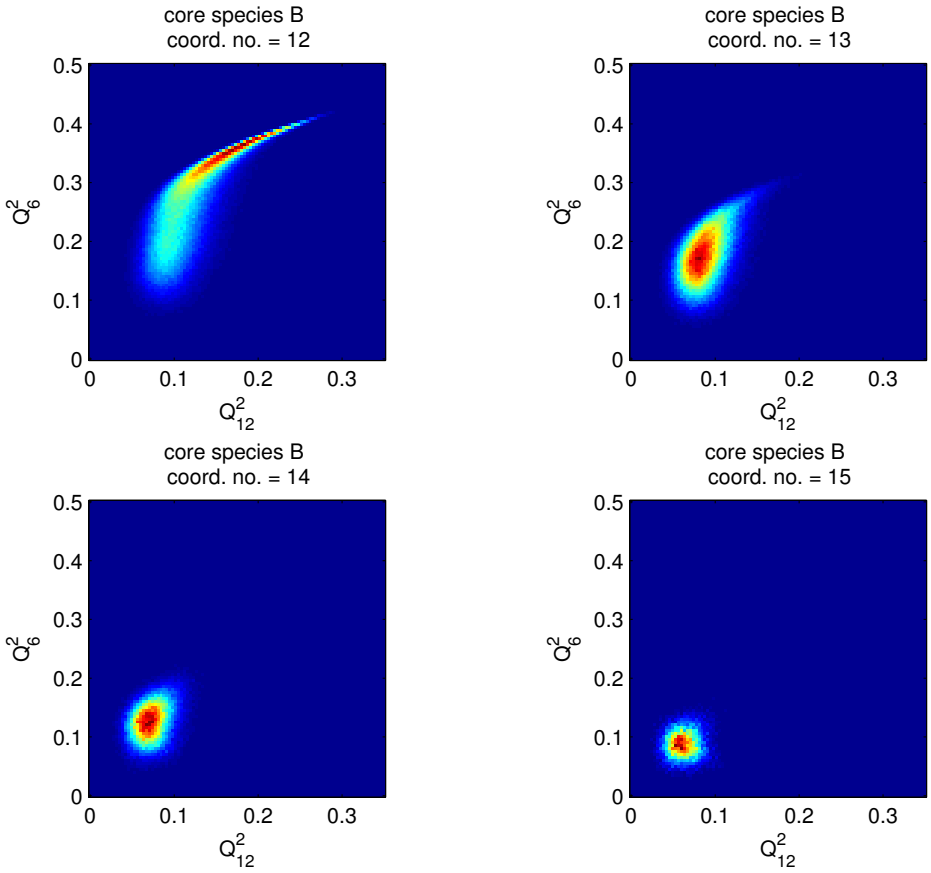

Figure 60: Here are the $(6, 12)$ two-harmonic distributions at $T = .52$ for core species B for coordination numbers 12-15. For coord. no. 12 the tail is the most prominent feature, but there is a significant region of configurations which are not part of the tail. The boundary between tail and body is not well defined. The distribution for coord. no. 13 has a small, faint tail for high Q_6^2 and Q_{12}^2 and a featureless body. For coord. nos. 14 and 15, the distributions are small and featureless.

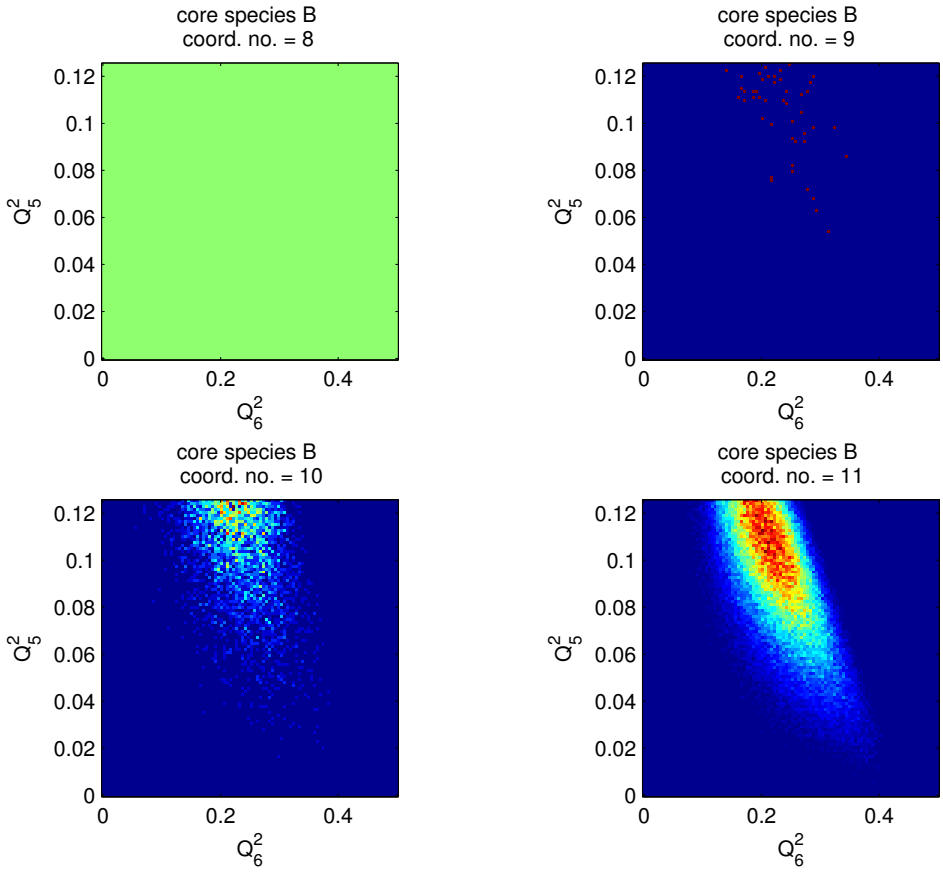

Figure 61: Here are the $(5,6)$ two-harmonic distributions at $T = .52$ for core species B for coordination numbers 8-11. For coord. no. 8, no configurations are shown, explaining why the entire pseudocolor plot appears green. From coord. nos. 9 to 11 the distribution descends toward lower Q_5^2.

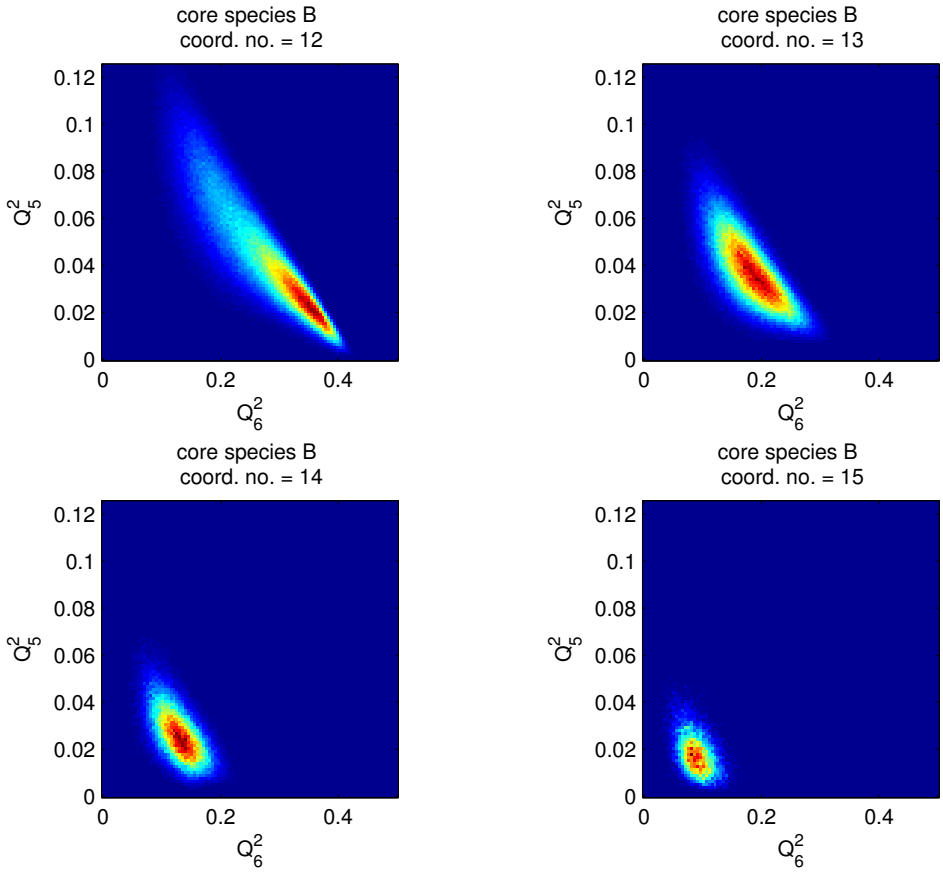

Figure 62: Here are the $(5,6)$ two-harmonic distributions at $T = .52$ for core species B for coordination numbers 12-15. Each of these distributions form a band in the complete $(5,6)$ plot for core species B shown in figure 38.

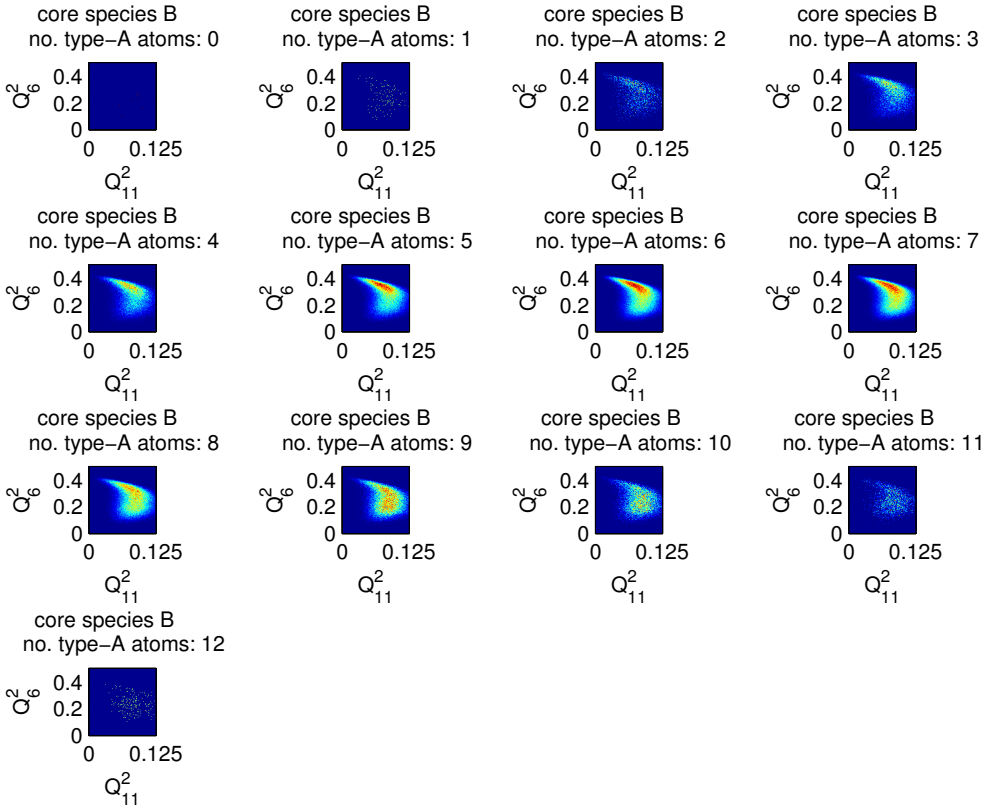

Figure 63: Here are the $(6, 11)$ two-harmonic distributions at $T = .52$ for core species B for coordination number 12 for various numbers of type-A shell atoms.

3.8 Two-harmonic distributions: Shell species combinations

In figure 63 we see the two-harmonic distribution plotted for all particles that have cores atom of type B, 12 shell atoms in the first shell, and various numbers of type-A atoms in those 12-atom shells. The temperature is $T = .52$. The graphs are clearest for shell combinations with 6, 7, or 8 type-A atoms, which makes sense considering most 12-atom shells have these numbers of type-A atoms as seen in fig. 56. Every distribution whose shape is somewhat clear has the same shape consisting of a tail extending towards low Q_{11}^2 for high Q_6^2 and a rounder low-Q_6^2 body. The relative densities of the tails and the bodies seem to shift slightly as we alter no. type-A atoms. For no. type-A atoms 3 and 4 we see more of an emphasis on the tail, but for no. type-A atoms 9 and 10 we see more emphasis on the body.

3.9 Two-harmonic distributions: Temperature dependence

In fig. 64, we plot $(6, 12)$ for type-B configurations for various temperatures. As temperature drops from $T = 50000$ to $T = .52$, many of the more interesting characteristics appear in two-harmonic distributions, the most notable being the tails such as the one plotted in the $(6, 12)$ distributions. We see that the first hint of a tail appears at $T = 1.0$. (If $T = 1.2$ were plotted, we would see a slight extension that would be too ambiguous to call a tail.) As temperature decreases below $T = 1.0$, the tails extend out to higher Q_{12}^2 and have their density of configurations increase. Since the shape of the tails from place to place does not change much when temperature decreases, this increase in density represents an increase in the number of configurations within these tails.

To better understand the growth of these tails, we define tail configurations as those with $Q_6^2 > 0.3$ and $Q_{12}^2 > 0.1$ and plot their temperature dependence. The number of tail configurations for each temperature were counted over 20 different moments in time and averaged. Fig. 65 shows the number of tail configurations for $T \leq 1.4$ on a linear-linear plot, and fig. 66 shows the number of tail configurations over all temperatures on a log-log plot.

In fig. 67, we plot the $(5, 6)$ distribution for type-B configurations for various temperatures. At $T = 50000$ and $T = 200$, we see distributions which would probably resemble figures 16, 17, or the high-temperature plots in fig. 64 if the axes were scaled in the same way. At $T = 2.25$ the distribution extends more in the higher-Q_6^2 direction, and at $T = 1.4$ we see a slight protuberance in that direction. The parallel bands of negative slope that we see in the $T = 0.53$ plot first appear at $T = 1.0$ as a bumpy low-Q_5^2, high-Q_6^2 side to the distribution. These bands become more clear as temperature decreases. That each band represents a different coordination number shows us that the importance of coordination number is greater for low temperatures, when clear bands can be seen for each number, than for high temperatures.

In figure 68, we plot the harmonic average for all type-B configurations in the $(6, 12)$ tail and the harmonics for an icosahedron. The latter are all zero except for $l = 6, 10$, or 12. At these three harmonic indices, the harmonic averages for the tail configurations are highest, so there seems to be a connection between icosahedral structure and the tail configurations. In addition, from fig. 69 we see that Q_{10}^2 and Q_{12}^2 increase as Q_6^2 increases, and that all other harmonics decrease, suggesting that, on the $(6, 12)$ tail, structures become more icosahedral the closer toward the $Q_6^2 = 0.44$ limit we get.

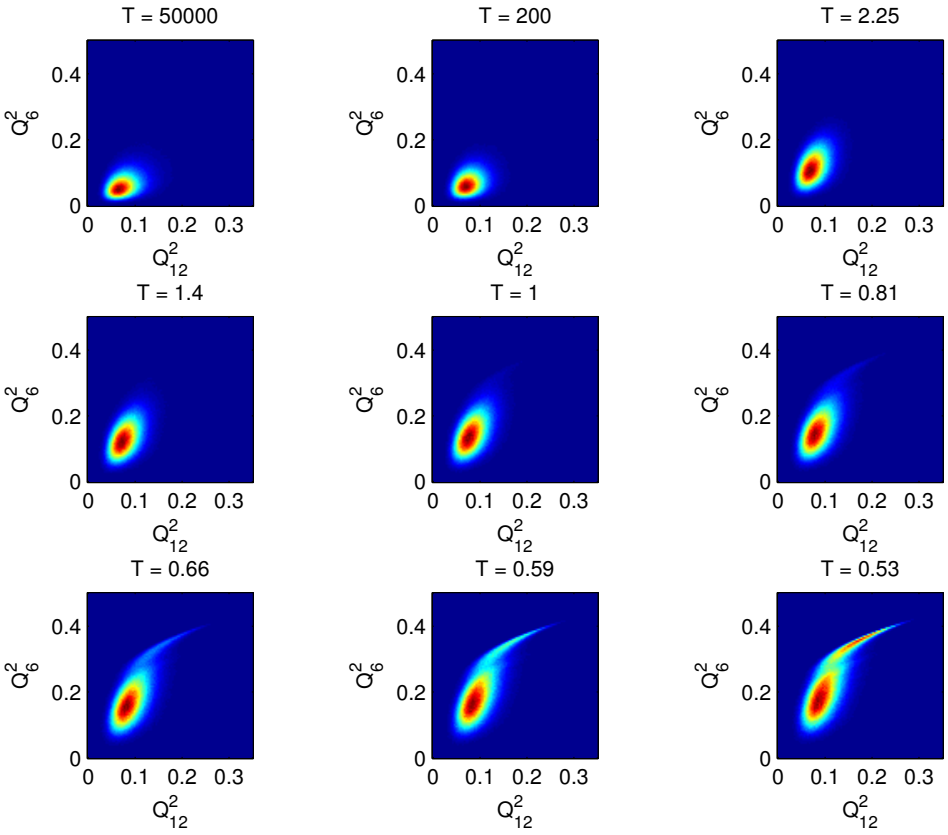

Figure 64: Here we plot $(6, 12)$ for configurations of a type-B core atom for temperatures $T = 50000, 200, 2.25, 1.4, 1, 0.81, 0.66, 0.59$, and 0.53. At $T = 50000$ and $T = 200$, we see featureless distributions such as those plotted in figures 16 or 17. At $T = 2.25$ we see that the distribution stretches to higher Q_6^2. At $T = 1.0$, the first hint of a tail appears, which grows in prominence as temperature continues to decrease.

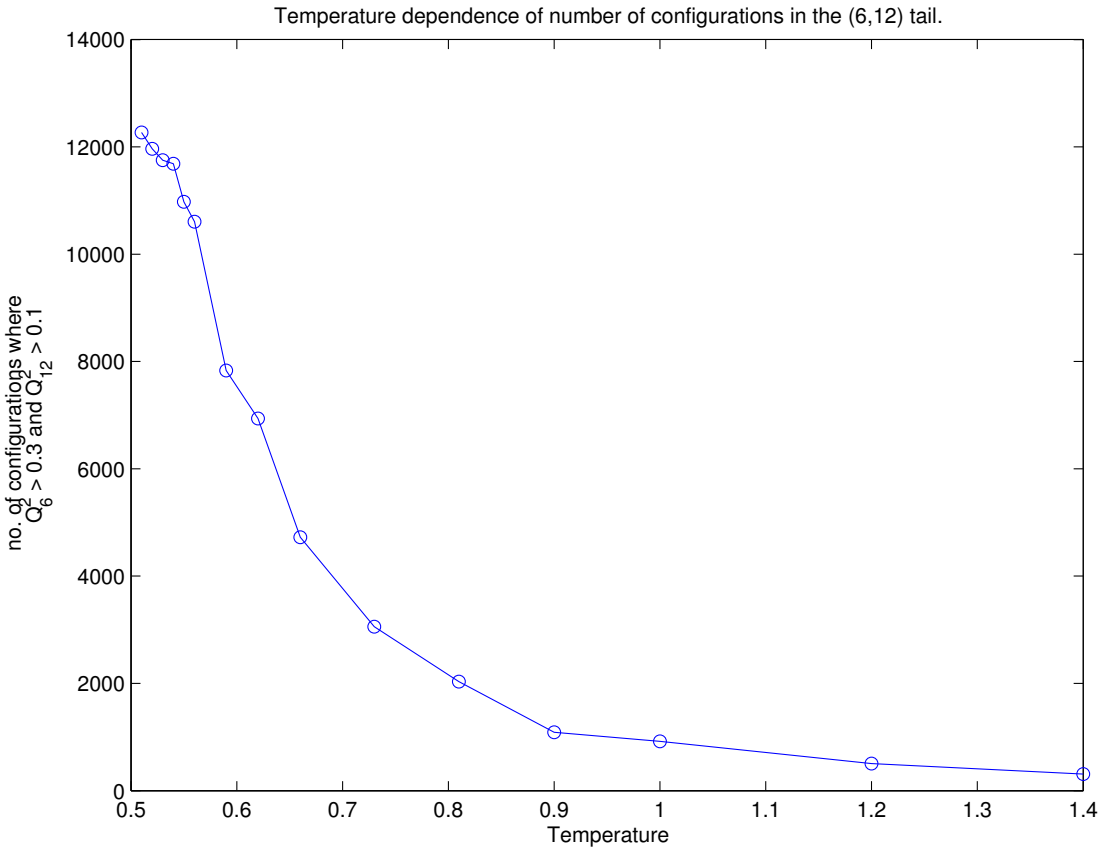

Figure 65: We plot the number of configurations such that $Q_6^2 > 0.3$ and $Q_{12}^2 > 0.1$ as a function of temperature for low temperatures. We note a steep increase as temperature decreases.

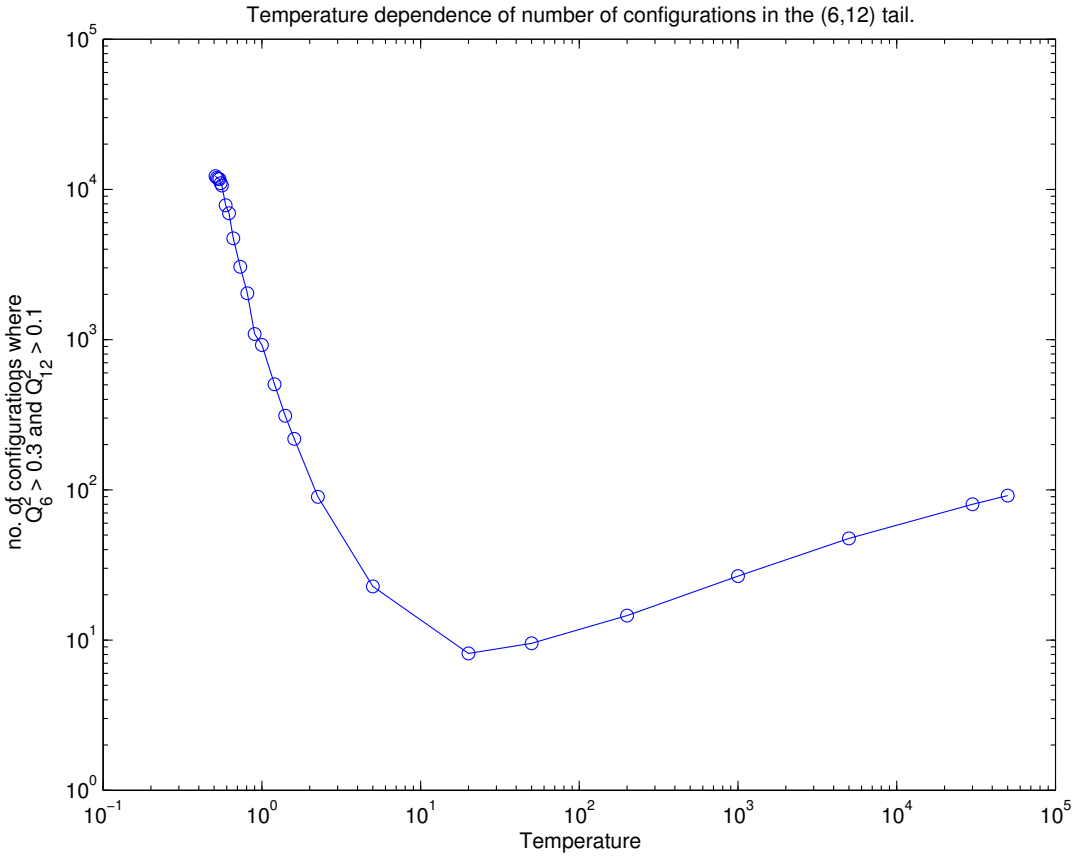

Figure 66: We plot the number of configurations such that $Q_6^2 > 0.3$ and $Q_{12}^2 > 0.1$ as a function of temperature for all temperatures. We note that this curve when plotted on a log-log plot appears to be linear for $T > 50$ and for $T < 2.25$, though the slopes differ in both sign and magnitude. The region $2.25 < T < 50$ does not appear to represent an abrupt transition from one type of behavior to the other.

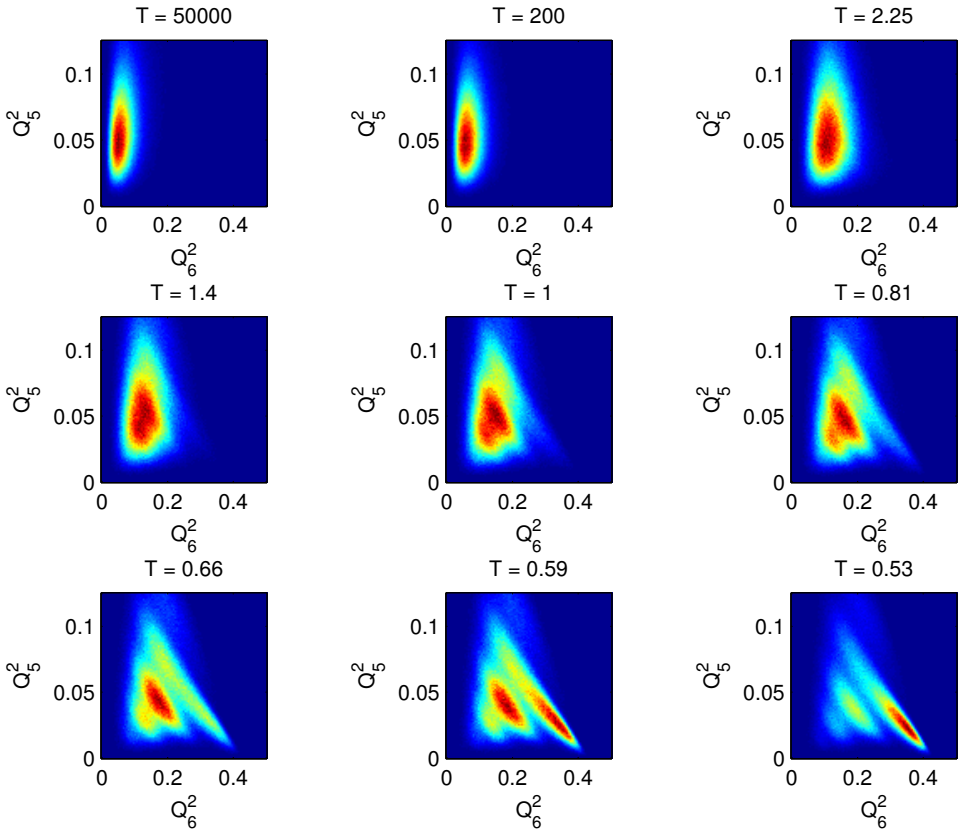

Figure 67: Here we plot $(5, 6)$ for configurations of a type-B core atom for temperatures $T = 50000, 200, 2.25, 1.4, 1.0, 0.81, 0.66, 0.59$, and 0.53.

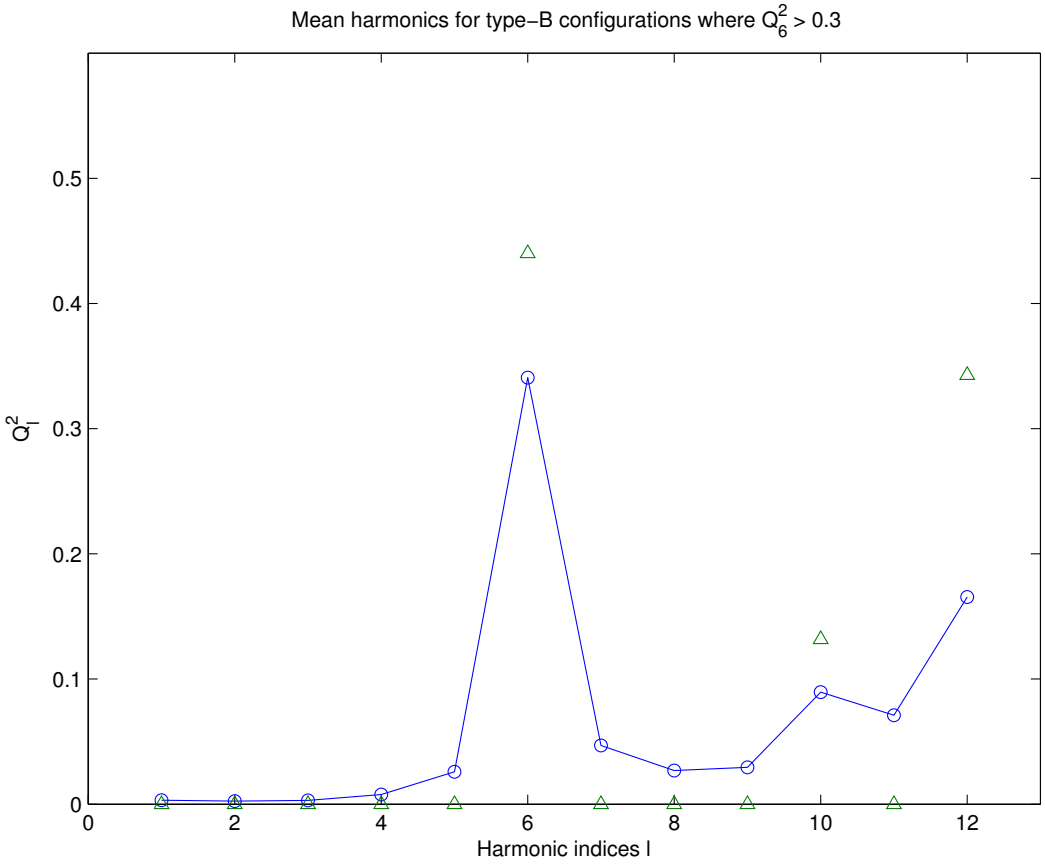

Figure 68: The harmonic averages for all type-B configurations in the $(6, 12)$ tail are plotted as "o" and connected by lines. The harmonics for an icosahedron are plotted as triangles.

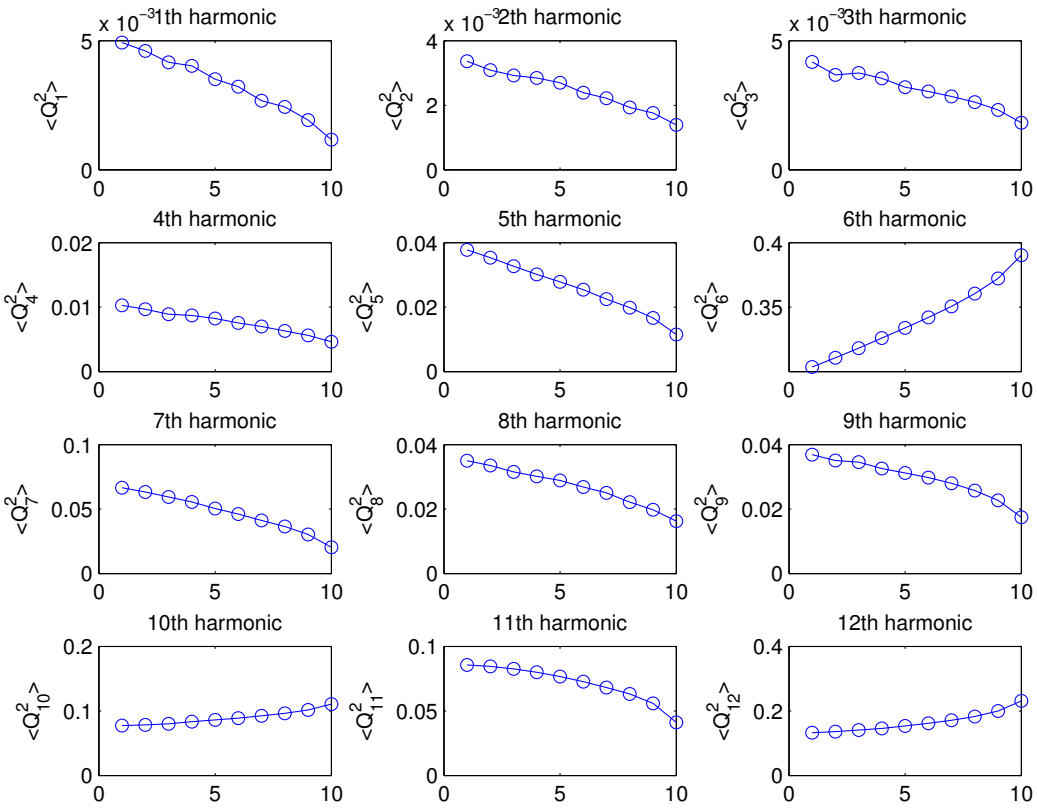

Figure 69: We sort all type-B configurations with $Q_6^2 > 0.3$ by Q_6^2 and group them into ten groups with equal numbers of configurations. Specifically, letting x be the value on the horizontal axis, the Q_6^2 bounds for each set of configurations are (0.3000, 0.3070) for $x = 1$; (0.3070, 0.3143) for $x = 2$; (0.3143, 0.3220) for $x = 3$; (0.3220, 0.3299) for $x = 4$; (0.3299, 0.3379) for $x = 5$; (0.3379, 0.3462) for $x = 6$; (0.3462, 0.3553) for $x = 7$;(0.3553, 0.3660) for $x = 8$; (0.3660, 0.3788) for $x = 9$; and (0.3788, 0.4239) for $x = 10$. We see that with a few negligible exceptions, as Q_6^2 increases, Q_l^2 decreases toward 0 for $l = 1, 2, 3, 4, 5, 7, 8, 9$, and 11, and Q_l^2 increases for $l = 10$ and $l = 12$.

3.10 Cross-harmonic correlations

The cross-harmonic correlation function $c(l, j)$ described in equation (13) can be used to characterize the two-harmonic distributions. In figures 70 and 71, we have plots that represent whether $c(l, j)$ is positive and relatively large (red), positive and small (yellow), negative and small (cyan), or negative and relatively large (blue). We say $c(l, j)$ is "small" if $|c(l, j)| < 0.005$, 0.005 being a somewhat arbitrary value meant to separate out the closer-to-zero values. We categorize the correlations in this manner because we are more interested in whether correlations are positive or negative than in their specific values. We make note of close-to-zero values because the difference between a positive and a negative $c(l, j)$ should be significantly large, so we should be skeptical of a reversal of the sign of $c(l, j)$ if $c(l, j)$ remains small. Fig. 70 deals with type-A configurations, and fig. 71 deals with type-B configurations, and both figures vary the coordination number and include one all-coordination-numbers plot. For all plots of $c(l, j)$, we note that for all l and j: $c(l, j) = c(j, l)$, which is true because the definition of $c(l, j)$ is invariant when we switch l and j; and $c(j, j) > 0$, which is true because $c(l, j)$ represent correlations of fluctuations of the lth harmonic about its mean with fluctuations of the jth harmonic about its mean, and it is impossible for a single variable to fluctuate above its mean and below its mean at the same time.

We include plots of different coordination numbers so that we can see whether features on an all-coordination-numbers distribution, such as a distribution seeming to point in a certain direction, are consistent across coordination numbers or an artifact of summing up these separate distributions that are centered in separate locations. In other words, we are most interested in the differences for these plots between coordination numbers.

For the type-A distributions, there are many observations we could make. As coordination number increases, the group of positive $c(l, j)$ for low l and j seems to grow larger, toward greater l and j. Also notable is that $c(10, 12)$ is only positive when the coordination number is 12. For coord. no. 9 we have a checkered pattern in the region $l = 6, 7$ with $j = 1, 2, 3, 4$. This signifies that, for configurations of coord. no. 9, there is some dependence on whether or not l or j are even or odd. We note that $c(5, 6)$ is always negative, which agrees with our finding of bands of negative slope in the $(5, 6)$ plot in 53.

For the type-B distributions, we first note the regularity of the coord. no. 12 plot in fig. 71. This pattern seems to distinguish the effects of the 6th, 10th, and 12th harmonics from the remaining harmonics. With the exception of $c(4, 11)$, which seems to be "small" and possibly negligible, the 6th, 10th, and 12th harmonics are negatively correlated with the other harmonics and positively correlated with themselves, and the other harmonics are positively correlated with themselves and negatively correlated with the 6th, 10th, and 12th harmonics. This agrees with the tendencies of the harmonics in the type-B distribution tails as Q_6^2 increases, as noted in fig. 69.

Overall, we note that $c(11, 12)$ is always negative if we consider only distributions for individual coordination numbers, but when we combine them into

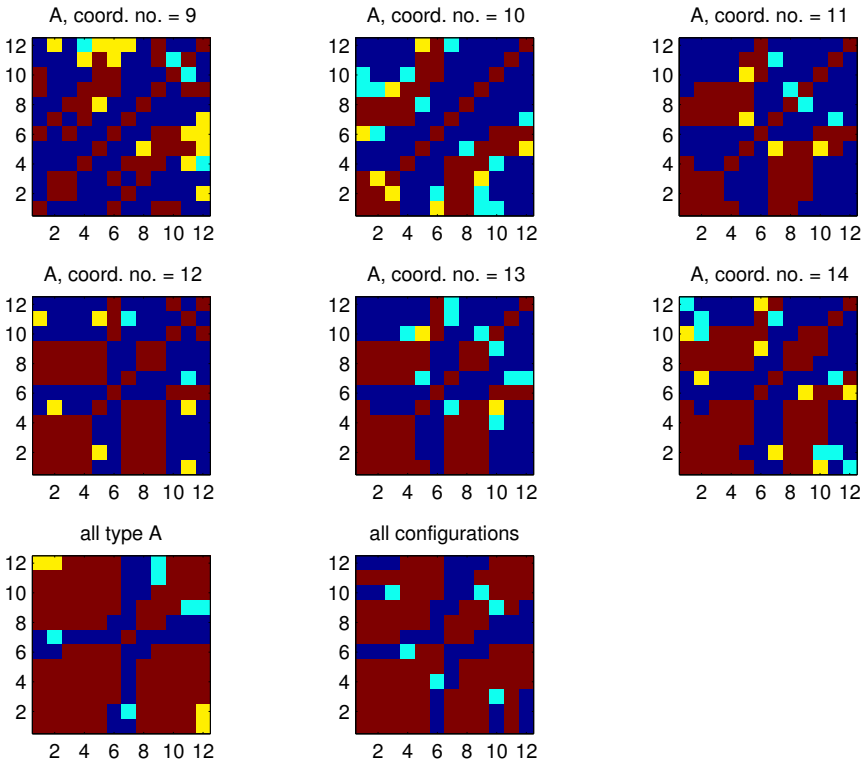

Figure 70: These plots are representations of $c(l, j)$ as described in the text. Only type-A configurations are considered here. The full-shell radius definition of a configuration was used.

an all type-A or an all configurations distribution, this correlation becomes positive. In all cases, $c(6, 10)$ and $c(6, 12)$ are positive, but $c(10, 12)$ varies from case to case.

Most of the work in this project uses a full-shell radius to define configurations, but we are interested in using $c(10, 11)$ to see whether or not the behavior of the 11th harmonic is similar to that of the 10th and 12th harmonics as suggested by Phillies and Whitford [26]. Phillies and Whitford used a half-shell radius to define their configurations, so for a direct comparison we represent the half-shell $c(l, j)$ in fig. 72 for type-A configurations and in fig. 73 for type-B configurations. We note that $c(10, 11)$ is negative for every case except when we average over all configurations. We also note that the half-shell $c(l, j)$ representation for coord. no. 12 and type-B core atoms is identical to the full-shell representation except for $c(4, 11)$, which is positive for half shells and slightly negative for full shells, and for $c(3, 11)$, which is only slightly positive for full shells.

In figures 74 and 75 we plot the cross-harmonic correlation functions $c(6, 12)$

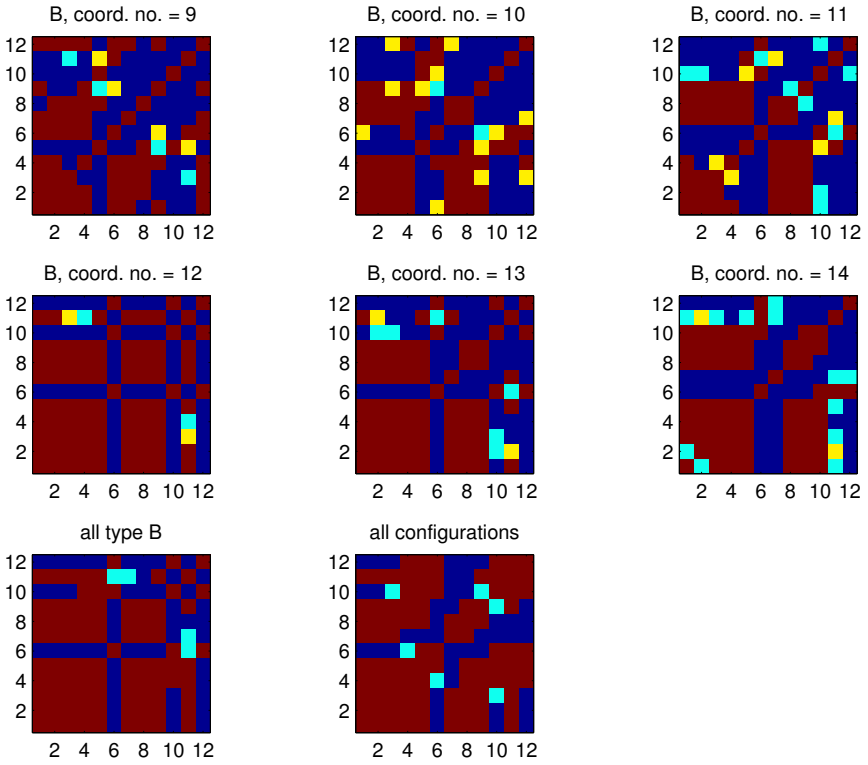

Figure 71: These plots are representations of $c(l, j)$ as described in the text. Only type-B configurations are considered here. The full-shell radius definition of a configuration was used.

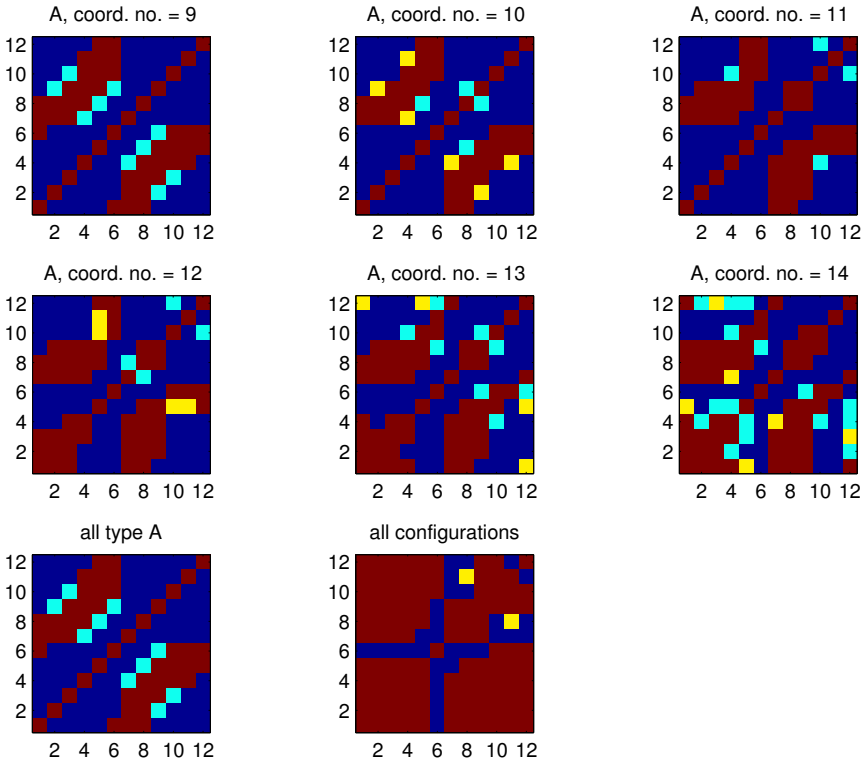

Figure 72: These plots are representations of $c(l, j)$ as described in the text. Only type-A configurations are considered here. The half-shell radius definition of a configuration was used.

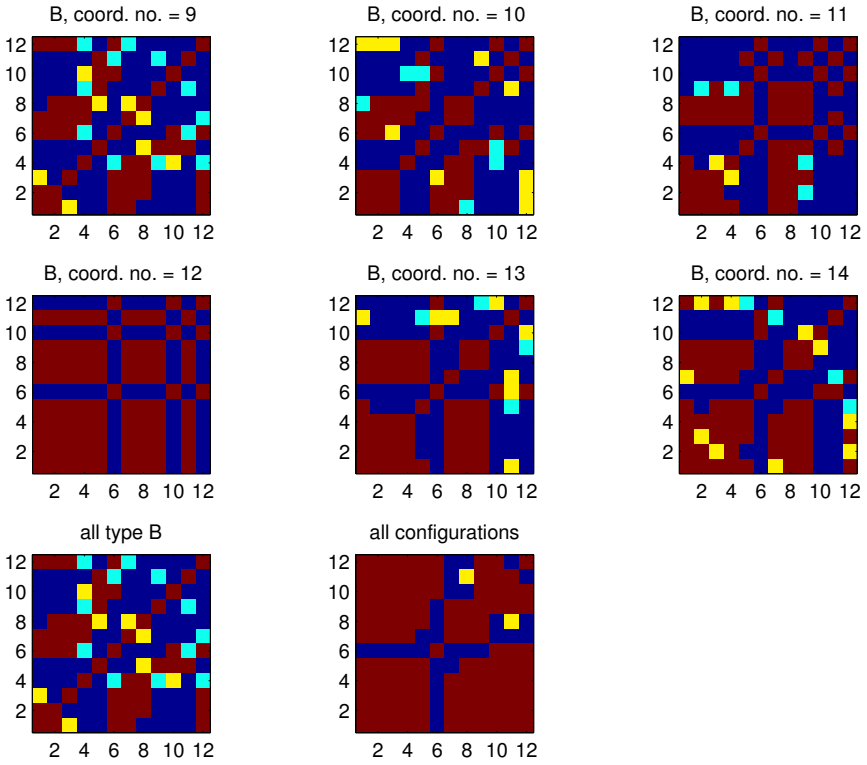

Figure 73: These plots are representations of $c(l, j)$ as described in the text. Only type-B configurations are considered here. The half-shell radius definition of a configuration was used.

and $c(5,6)$ as functions of temperature. Temperature is plotted logarithmically but $c(l,j)$ is plotted linearly. We avoid plotting $c(l,j)$ on a log-log plot because in general $c(l,j)$ may become negative as temperature drops, although this does not occur for $c(5,6)$ or $c(6,12)$. These correlations were averaged over all configurations, rather than only over type-B configurations, so a comparison of these functions to the two-harmonic distributions' time dependencies in figures 64 and 67 would be problematic. We can note, however, that the all-configuration two-harmonic distribution plot of $(6,12)$ at $T = 50000$ resembles the plots in figures 16 and 17, and that this plot transforms to the all-configurations $T = .52$ plot in fig. 18. The growth of a tail, especially, seems that it would increase $c(6,12)$ since the tail extends out far from the means $\langle Q_6^2 \rangle$ and $\langle Q_{12}^2 \rangle$, and has a positive slope. Thus the growth of the $(6,12)$ tail and the steep increase in $c(6,12)$ as temperatures decrease may be related. A less tenuous observation is that as temperature increases above about $T = 200$, these correlations, and indeed all correlations $c(j,l)$, rise in a way that appears linear when plotted on a lin-log or a log-log plot.

4 Discussion

To reiterate our most important result, as temperature decreases the two-harmonic distributions exhibit behavior which is indicative of near-icosahedral structure. Many of the two-harmonic distributions have tails to some degree, the clearest case being the $(6,12)$ type-B distribution's tail. These tails exist almost exclusively for type-B configurations, with the type-A $(6,7)$ distribution plotted in figure 55 being an exception; even so, this type-A tail is relatively unpopulated compared to most type-B distributions' tails. In addition, in figures 59 and 60 we see that almost all configurations in the $(6,12)$ tail have a coordination number of 12, although the distributions for coordination numbers 11 and 13 seem to have tails to a very small degree. These tails become thinner in shape as Q_l^2 increases for $l = 6, 10$, and 12 or decreases for the remaining harmonics, as detailed in the captions of figures 19 to 51. The configurations in the $(6,12)$ tail seem to lie in the area $Q_6^2 > 0.3$ and $Q_{12}^2 > 0.1$, so we use these inequalities as a definition for "tail configurations".

From fig. 68 we see that the harmonic averages for the tail configurations resemble the icosahedral harmonics, and in figures 76 and 77 we see somewhat of a resemblance between an icosahedron and a randomly-chosen configuration with $Q_6^2 > 0.35$. From fig. 69 we see that increasing Q_6^2 for configurations where Q_6^2 is already greater than 0.3 leads to Q_l^2 increasing for $l = 10$ or 12 and decreasing for all other l. This pattern of harmonic increase/decrease means that as Q_6^2 increases in the direction of the icosahedral limit $Q_6^2 = 0.44$, *the other harmonics also become more icosahedral*. The increase/decrease pattern is supported by the coord. no. 12 plot in fig. 71.

(As an aside, we note that in fig. 68, the $\langle Q_l^2 \rangle$ for $l \neq 6, 10$, or 12 seem to get larger for larger l, and that $\langle Q_{11}^2 \rangle$ is nearly the size of $\langle Q_{10}^2 \rangle$. This is to be expected. Spherical harmonics divide the sphere into a number of regions

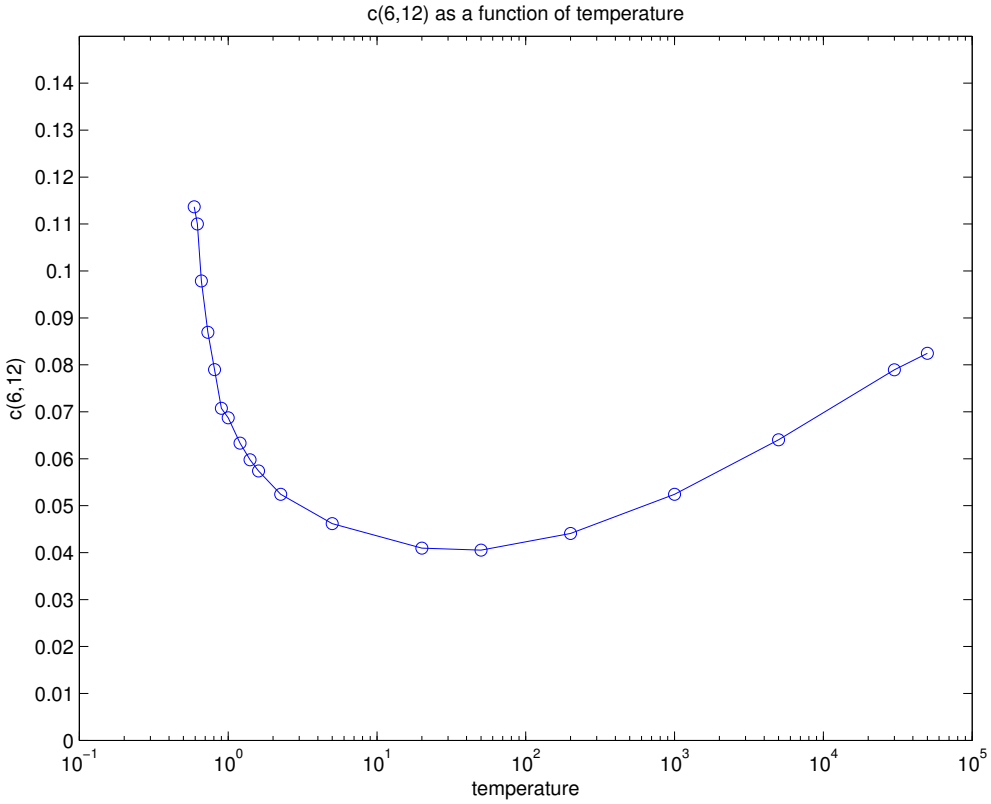

Figure 74: Here we have the cross-harmonic correlation $c(6, 12)$ plotted as a function of temperature on a linear-log plot. It appears that this increases linearly on a lin-log plot as temperatures increase for high temperature. Also, there is a steep increase in the correlation function as temperature decreases for low temperatures, and a smooth transition from one type of behavior to the other.

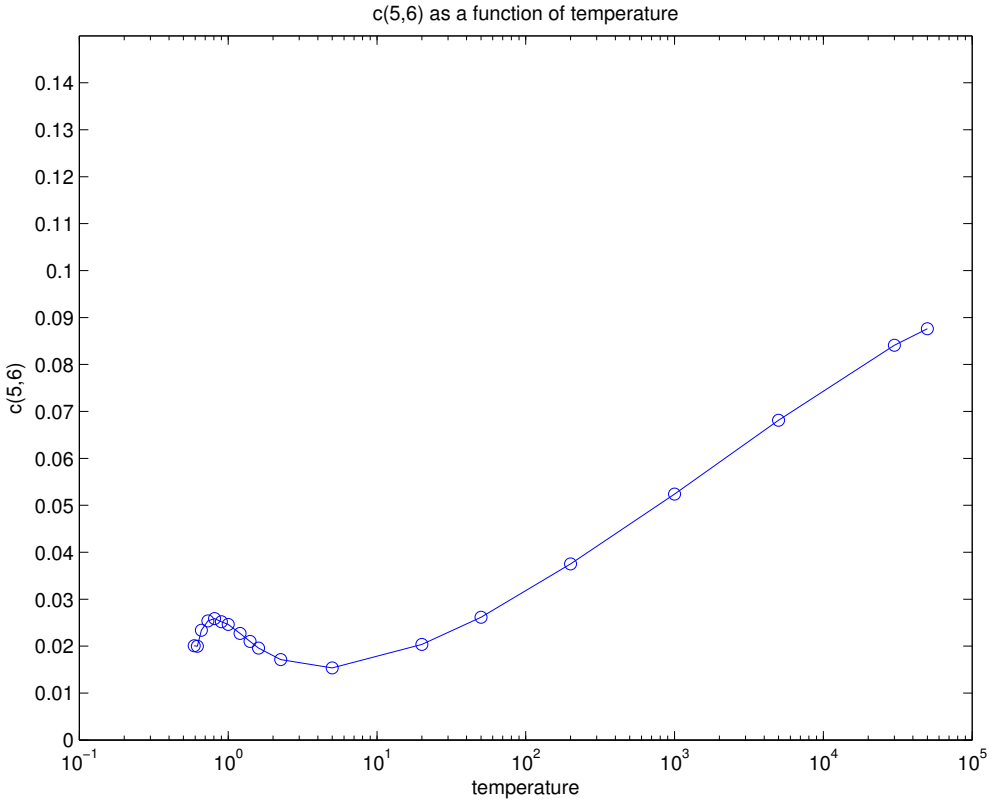

Figure 75: Here we have the cross-harmonic correlation $c(5,6)$ plotted as a function of temperature on a linear-log plot. It appears that this increases linearly on a lin-log plot as temperatures increase for high temperature. For low temperatures we see a strange behavior where, as temperature decreases, $c(5,6)$ decreases, then increases, then decreases again.

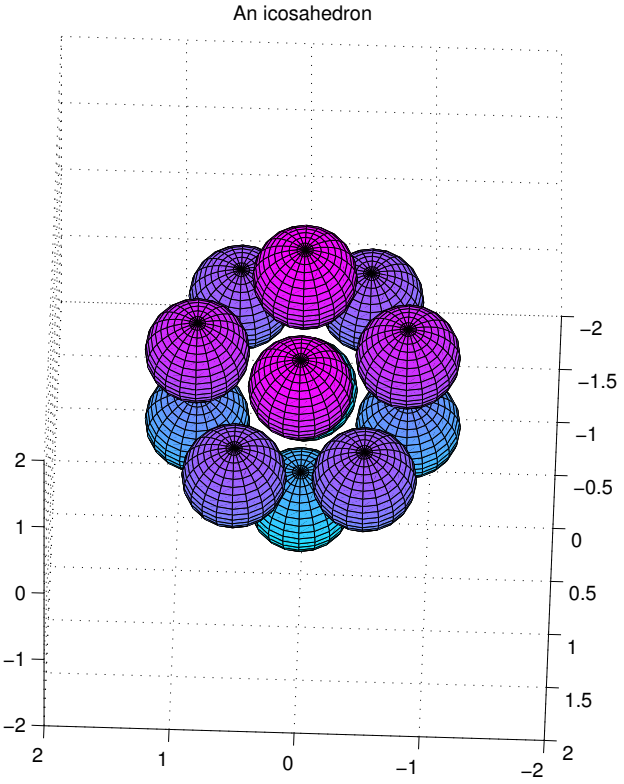

Figure 76: An icosahedron oriented so two opposite points line up in our view.

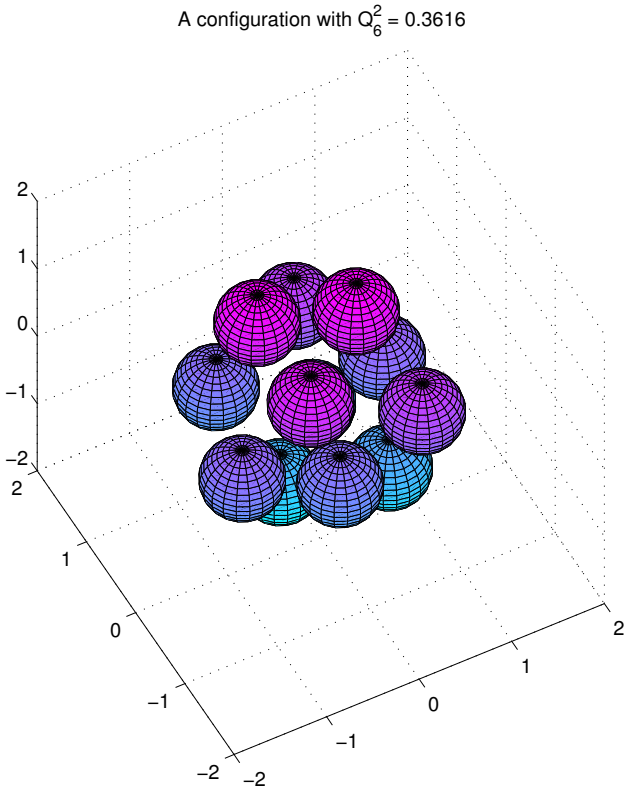

Figure 77: This configuration was a randomly chosen configuration with $Q_6^2 > 0.35$; it is oriented so two opposite points line up in our view.

which increases with l, so random deviations would be more likely to alter Q_l^2 for large l, when the regions are smaller, than for small l. In fig. 76 we see that there is perfect 10th-order symmetry in a perfect icosahedron, but it seems reasonable that deviations such as those of the near-icosahedron in fig. 77 would significantly increase the 11th-order harmonic.)

Furthermore, figures 65 and 66 show that the number of tail configurations increases exponentially as temperature decreases for $T < 1.0$. This is also shown in the graphs in fig. 64 which show that the tail emerges for $T \leq 1.0$. Thus icosahedral structure increases in our system as temperature decreases, a behavior originally predicted by Frank [2] in 1952 as a reason for glass-formation.

We should emphasize, however, that we have not defined what structures can be considered "icosahedral", but rather we have shown that tails exist, and that within these tails are configurations which become *more icosahedral* as one moves down these tails. We can, however, make estimates on the number of configurations in the type-B $(6, 12)$ tail in fig. 44. First, from fig. 65 we know that, out of 125000 configurations in our system, there are on average just over 12000 of those configurations in the $(6, 12)$ tail, about 10%. If we want to count configurations that are more strictly icosahedral, we can choose the region $0.3788 < Q_6^2 < 0.4239$, which is the Q_6^2 region closest to the icosahedral value of $Q_6^2 = 0.44$ that contains one tenth of the particles in the tail, numbering about 1200 configurations or about 1% of the total.

It is difficult to compare our estimates of the prevalence of icosahedral order with previous studies' estimates because there are many ways researchers define icosahedral order. As noted in the Introduction, Stillinger and LaViolette [17] [18] have voiced skepticism about the role of icosahedra in glass-forming based on arguments involving "distance violations" in configurations. They found only one configuration in 1465 configurations with coord. no. 12 in their system that had as few as one distance violation. We cannot compare Stillinger and LaViolette's results with our results, but we can note a few differences between our work and theirs: 1. They used a steepest-descent method to quench the system to local energy minima, which differs from our method of cooling the system gradually and letting the system equilibrate. 2. They used a potential slightly different from the LJ potential, one where a large system would settle into an FCC crystal structure rather than the HCP structure resulting from an LJ potential. This was done to more closely mimic the noble gases, which crystallize into an FCC structure. These two differences, in addition to the different definitions of what constitutes an icosahedron, may be responsible for the finding of icosahedral order in our system but not in the simulations of Stillinger and LaViolette.

As mentioned in the Introduction, Di Cicco and Trapananti [14] [20] have obtained a figure of 10% nearly icosahedral configurations in a supercooled liquid copper sample. Their definition of nearly icosahedral configurations are configurations with $\hat{W}_6 < -0.09$, which is a range corresponding to bond-angle distributions which have peaks for angles indicative of icosahedra. It is not clear how arbitrary the change in the bond-angle distribution is at $\hat{W}_6 = -0.09$, though from fig. 60 we see that our definition of tail configurations as being

those with $Q_6^2 > 0.3$ and $Q_{12}^2 > 0.1$ is also somewhat arbitrary. It is strange that Di Cicco and Trapananti's 10% figure coincides with the number of tail configurations in the $(6, 12)$ tail at $T = .52$ in our system, which is also about 10%, but unless Di Cicco and Trapananti's nearly icosahedral configurations can be shown to match our tail configurations, the sharing of a 10% figure seems to be a coincidence.

Using common-neighbor analysis to define icosahedral structure, Celino, et al. [22] provided some estimates for the prevalence of icosahedra. Specifically, 0.26% of their undercooled liquid system consists of "perfect icosahedra", 0.11% for warmer liquids, and 9.15% of the system consists of "defective" icosahedra. Once again, it is difficult to compare results from a method like common-neighbor analysis with a method like counting the configurations in the tails of our two-harmonic distributions, though we can agree that somewhat icosahedral configurations are prevalent.

We now turn to the more general question of the relationship between the two-harmonic distributions and the arrangement of atoms. We are fortunate that the presence of icosahedral ordering manifested itself in such observable tails, and that we had the aid of Frank's prediction of icosahedral ordering in glasses [2], but unfortunately we do not have a theory regarding the non-icosahedral structures in our system. Instead, we have used the simple-looking $T = 50000$ distributions plotted in figures 16 and 17 as a standard for comparison. These high-temperature distributions seem not to depend much on harmonic indices l, and we do not expect local structure to play a significant role at high temperatures, so the shape of these distributions would seem to be due to randomness. Since we do not have a theory determining what distributions to expect for a certain noncrystalline system, the $T = 50000$ distributions give us valuable insight by showing how the harmonics exhibit themselves in very simple circumstances.

We can, however, make some educated guesses on how to interpret different distribution shapes. If we have a perfect crystal at absolute zero, then we have a small number of possible configurations, meaning that only a few very-populated dots on the two-harmonic plots would be occupied, likely with $Q_l^2 = 0$ for odd l. Thus, the presence of dots on two-harmonic plots would suggest crystal structures.

A more complicated distribution to analyze would be the $(6, 12)$ tail in fig. 44. All perfect icosahedra would be located at $Q_6^2 = 0.44$ and $Q_{12}^2 = 0.3427$. All configurations in our simulations have $Q_6^2 < 0.44$, so formation of icosahedral ordering would require that Q_6^2 increase. The high value of $Q_6^2 = 0.44$ is due to the icosahedron's high degree of symmetry, and one would imagine that the higher the degree of symmetry, the fewer possible structures would exist. Assuming that these structures would not all share the same Q_{12}^2 value, then a narrower range of structures would suggest a narrower range of Q_{12}^2. This may explain why the $(6, 12)$ tail becomes thinner as Q_6^2 increases. Similar arguments can be made for this "thinning" shape of tails in other two-harmonic distributions.

One interesting distribution shape is the banded structure of $(5, 6)$ for type-A distributions in figure 38. In figures 61 and 62 we show that the different

bands correspond to different coordination numbers. However, we are still left with the question, "what is the significance of these bands being parallel?" (We should keep in mind, however, that the type-B $(5, 6)$ distributions for coord. nos. 10 and 11 seem to significantly overlap, so not all of the bands are parallel and separate.) This behavior seems to suggest that adding or subtracting a particle from a type-B configuration would not disturb whatever it is that makes the $(5, 6)$ distributions lie on a negatively-sloped line, though for some reason it shifts the location and length of the bands.

Another interesting behavior we note is that the correlations $c(l, j)$ (see fig. 74 and fig. 75) and the number of tail configurations (see fig. 66) seem to rise at high temperatures in a way that appears linear on a log-log plot. This seems strange. We would assume that as temperature increases, the system would become more and more like an ideal gas and would have less structure, so each harmonic would have no reason to depend on another harmonic in a non-random way. In addition, from fig. 64 we see that from $T = 2.25$ to $T = 50000$ the distribution seems to be retreating to the direction of the origin and that there are no tails in either of these distributions. A related observation we noted earlier is that the peak of $\langle Q_l^2 \rangle$ in fig. 12 seems to shift toward higher l as temperature increases. At $T = 50000$, $c(j, l)$ is always positive, so if we selected configurations with $Q_l^2 > \langle Q_l^2 \rangle$ for a certain l, then we would expect the neighboring harmonics to, on average, move above their means as well. Perhaps there is a connection between the $\langle Q_l^2 \rangle$ curve seeming to expand out to larger l and the $c(l, j)$ becoming all positive as temperature increases. To explain these behaviors, one would need a deeper analysis of how the harmonics relate to each other at high temperatures, possibly using Landau theory. Steinhardt, et al. used Landau theory to derive equations constraining possible configurations to answer questions such as, "what configurations exist such that $Q_4^2 = 0$ when $Q_6^2 \neq 0$?" [15].

Phillies and Whitford [26] noted that the behavior of the 10th, 11th, and 12th harmonics seemed to be similar, specifically, that their $\langle Q_l^2 \rangle$ were similar, that they all decreased by almost 10% as T drops from 1.2 to 0.56, and that the function $C_l^{(2)}(t)$ introduced in equation (10) has similar behavior for $l = 10$, $l = 11$, and $l = 12$. We have not calculated the $C_l^{(2)}(t)$, but we can say that the existence of similar behavior for $\langle Q_{10}^2 \rangle$, $\langle Q_{11}^2 \rangle$, and $\langle Q_{12}^2 \rangle$ appears to be true only when we average over all particles. If we stick to the tail configurations as we have done for the data in figures 68 and 69, we find that Q_{11}^2 decreases as Q_{10}^2 and Q_{12}^2 increase. Furthermore, from figures 72 and 73 which represent the $c(l, j)$ for half-shell configurations, we see that the 11th and 12th harmonics are always correlated for the various coordination numbers *except when we combine these distributions into an all-configurations distributions.* This suggests that the similar behavior between the 11th harmonic and the 10th and 12th harmonics may be an artifact of the two atom species having different distributions, rather than representing the relationship between Q_{10}^2, Q_{11}^2, and Q_{12}^2 within each configuration.

The two-harmonic distribution method has a few advantages over methods

used in previous studies. As mentioned before, there are three common ways of quantifying the structure of a configuration: Steinhardt's invariants (i.e., the harmonics), common-neighbor analysis, and Voronoi analysis. The latter two methods assign integer indices to a structure to classify it, while the harmonics assign a real number to the structure. This means that the harmonics, but not the common-neighbor analysis or the Voronoi analysis, lend themselves to an analysis of the continuous range of structure. In addition, the use of the two-harmonic distributions, together with analysis of the harmonic composition and growth of the $(6, 12)$ tails, seems to be a more direct way of testing for the presence of icosahedra than many of the methods used in past molecular dynamics study. This directness of structural characteristics display may be the two-harmonic distribution's greatest advantage.

There are disadvantages to this method as well. One needs 1,500,000 configurations to generate two-harmonic plots at the same level of detail as in our project; this would be a heavy computational demand. In addition, storage of this data can be difficult. If we wanted maximum flexibility, then we would store our raw data in a file containing 1,500,000 configuration's harmonics with core and shell species information; this would take hundreds of megabytes. If we allow the program to generate our distributions for us, defining which core and shell species we want to see ahead of time but keeping flexibility in which harmonic indices we choose, then we would have a file of several megabytes. Finally, although the presence of tails seems clear, from the coord. no. 12 plot in fig. 60 we see that there is no clear boundary between the tail and the body of the distribution, so while a two-harmonic $(6, 12)$ distribution is more clear in showing special behavior than a single-harmonic Q_6^2 distribution, this method does not entirely lift the ambiguity in determining what qualifies as "icosahedral order".

4.1 Suggestions for future research

There are many questions left unanswered. We have not investigated the relationship between the harmonics and relative position of configurations. For example, one could see if tail configurations are, on average, closer or farther from each other than non-tail configurations. Also, one imagines the more perfect icosahedra in our simulation might act as seeds to nuclei which expand as temperature decreases, possibly into Mackay icosahedra. We have looked at the two-harmonic distributions for the second full coordination shell, but we have not noticed anything unusual like tails. It might be worth analyzing the dependence of shell radii on the two-harmonic distributions, possibly finding tails and seeing that the number of tail icosahedra climbs exponentially as temperature drops, but whose number drops as one expands the shell radius.

We have not investigated how dynamical properties are related to different harmonics. Donati, et al. [32] have found that "mobile" and "non-mobile" particles tend to group in clusters, with mobile particles in string-like clusters and non-mobile particles in more compact clusters. Perhaps there is a connection between being non-mobile and having icosahedral order.

This project could be repeated for a single-species system with a crystal-inhibiting potential such as the Dzugutov potential [5]. It seems that a single-species system would avoid some species-related complexities such as having most icosahedral structures being type-B configurations. It would also be interesting to use two-harmonic distribution analysis on a glass-forming system which is not expected to form icosahedral structures. Iwamatsu and Lai [7] have noted that, in binary clusters when the size ratio is too large, icosahedra are no longer the lowest-energy structures. One might use a binary system with a size ratio having lowest energy states of neither icosahedra nor crystal structures.

Finally, the biggest uncertainty in our results seems to be the dependence of icosahedral ordering on our definition of coordination number. One theory is that some icosahedral configurations are being masked by the intrusion of another particle within the first full shell radius. However, preliminary attempts to remove the outermost atom from a few 13-atom shells to obtain icosahedra have not yielded icosahedra. In addition, Stillinger and LaViolette [17] have calculated the radial distribution function for different coordination numbers and found significant differences. If the difference between 12-atom and 13-atom configurations was simply an extra atom that had wandered within the coordination shell radius, then we would not expect the radial distribution function to differ much between coordination numbers.

5 Conclusions

We have introduced a method using two-harmonic distributions to represent local structure of systems. We have demonstrated that icosahedral order increases in a simulated glass-forming supercooled liquid as one decreases the temperature, and we have the following evidence to support this conclusion: 1. tail-like shapes in the two-harmonic plots appear as temperature decreases. Most tail configurations have a core atom of type-B and a shell of coordination number 12. 2. These tails appear to become thinner as the 6th, 10th, and 12th harmonics increase and the other harmonics decrease. 3. We have shown quantitatively that, by dividing the $(6, 12)$ tail according to Q_6^2 into ten sections and calculating the harmonic averages over each section, as Q_6^2 increases toward its icosahedral value of 0.44, $\langle Q_{10}^2 \rangle$ and $\langle Q_{12}^2 \rangle$ increase while the other harmonic averages decrease. 4. We have investigated cross-harmonic correlations $c(l, j)$ for harmonic indices l and j. The $c(l, j)$ for both full and half shells for coordination no. 12 have a pattern that is consisted with the aforementioned pattern of increase and decrease for each harmonic. This is sensible considering that many type-B, coord. no. 12 configurations are part of the $(6, 12)$ tail.

In addition, we have investigated the relationship between the 10th, 11th, and 12th harmonics using the half-shell $c(l, j)$. We have found that $c(10, 11)$ is negative when the correlation is averaged over configurations of each core atom type or over configurations categorized by coordination number within each type, but only when we average over both particle species does $c(10, 11)$ become positive, suggesting that the similarity between the 11th harmonic and the 10th

and 12th harmonics noted by Phillies and Whitford [26] is due to averaging over both species rather than to structural properties.

We have seen that the two-harmonic distributions and the cross-harmonic correlations are useful ways of representing relationships between different harmonics. These relationships can be a key to determining how local structure changes as a system changes. It would be worth exploring the two-harmonic distribution method further by using it to analyze other systems.

Acknowledgments

I would like to thank Josh Brandt and Mark Taylor for their assistance in using VEX.WPI.EDU, BIG16.WPI.EDU, and RAVE.WPI.EDU; Professors G. D. J. Phillies and Paul Whitford for their research, which is the foundation of this project, and for providing me with their programs and their data; Prof. Phillies for being my MQP advisor through most of the project, for having patience throughout my MQP work, and for his corrections, suggestions, and insights; Prof. Iannachione for advising me after Prof. Phillies was no longer able to; and my family, for their patience, for putting me through college, and for their unending support.

References

[1] W. Kauzmann, Chem. Rev. **43**, 219 (1948).

[2] F. C. Frank, Proc. Roy. Soc. London Ser. A **215**, 43 (1952).

[3] J. D. Honeycutt and H. C. Andersen, J. Phys. Chem. **91**, 4950-4963 (1987).

[4] W. Kob and H. C. Andersen, Phys. Rev. E **51**, 5 (1995).

[5] M. Dzugutov, Phys. Rev. A **46**, 6 (1992).

[6] M. Iwamatsu, Mat. Sci. and Eng. A **449-451**, 975-978 (2007).

[7] M. Iwamatsu and S. K. Lai, J. Non-Crys. Solids **353**, 3698-3703 (2007).

[8] S. Cozzini and M. Ronchetti, Phys. Rev. B **53**, 18 (1996).

[9] M. Kleman and J. F. Sadoc, J. Phys. (Paris), Lett. **40**, L569 (1979).

[10] D. R. Nelson, The Structure and Statistical Mechanics of Glass, 13-30, *Applications of Field Theory to Statistical Mechanics*, Springer Berlin / Heidelberg (1985).

[11] T. Tomida, T. Egami, Phys. Rev. B **52**, 5 (1995).

[12] E. W. Fischer, G. Meier, T. Rabenau, A. Patkowski, W. Steffen, and W. Meier, J. Non-Cryst. Solids **131-133**, 134 (1991).

[13] S. A. Kivelson, et al. J. Chem. Phys **101**, 3 (1994).

[14] A. Di Cicco, A. Trapananti, S. Faggioni, and A. Filipponi, Phys. Rev. Let. **91**, 13 (2003).

[15] P. J. Steinhardt, D. R. Nelson, and M. Ronchetti, Phys. Rev. B **28**, 2 (1983).

[16] H. Terrones and A. L. Mackay, J. Math. Chem. **15**, 157 (1994).

[17] F. H. Stillinger and R. A. LaViolette, Phys. Rev. B **34**, 8 (1986).

[18] R. A. LaViolette, Phys. Rev. B **41**, 12 (1990).

[19] S. Mossa and G. Tarjus, J. Chem. Phys. **119**, 15 (2003).

[20] A. Di Cicco and A. Trapananti, J. Non-Cryst. Solids **353**, 3671-3678 (2007).

[21] P. Ganesh and M. Widom, Phys. Rev. B **74**, 134205 (2006).

[22] M. Celino, V. Rosato, A. Di Cicco, A. Trapananti and C. Massobrio, Phys. Rev. B **75**, 174210 (2007).

[23] S. Sastry, P. G. Debenedetti, F. H. Stillinger, T. B. Schröder, J. C. Dyre, and S. C. Glotzer, Physica A **270**, 301-308 (1999).

[24] M. Jansen, J. C. Schön, and L. van Wüllen, Angew. Chem. Int. Ed. **45**, 4244-4263 (2006).

[25] D. R. Reichman and P. Charbonneau, J. Stat. Mech. P05013 (2005).

[26] G. D. J. Phillies and P. C. Whitford, Phys. Rev. E **52**, 021203 (2005).

[27] G. D. J. Phillies and P. C. Whitford, J. Chem. Phys. **122**, 044508 (2005).

[28] G. D. J. Phillies and P. C. Whitford, private communications.

[29] D. C. Rapaport, *The Art of Molecular Dynamics Simulation*, Cambridge University Press, (2004).

[30] S. Glotzer, J. Chem. Phys. **112**, 509 (2000).

[31] M. P. Calvo and J. M. Sanz-Cerna, SIAM J. Comput. Math. **14**, 936 (1993).

[32] C. Donati, S. C. Glotzer, P. H. Poole, W. Kob, and S. J. Plimpton, Phys. Rev. E **60**, 5 (1999).

[33] A. C. Mitus, F. Smolej, H. Hahn, and A. Z. Patashinski, Physica A **232**, 662-685 (1996).